Theories and Applications of Multiple Scattering of S-wave Scatterers

A thesis presented

by

Yick Stella Chan

to

The Department of Physics

in partial fulfillment of the requirements

for the degree of

Doctor of Philosophy

in the subject of

Physics

Harvard University

Cambridge, Massachusetts

September 1997

Abstract

Models and Applications of Multiple Scattering Theories in 2D have been studied. In particular, models have been built for STM and Coherent Backscattering experiments. The STM experiments have opened up a new class of scattering inversion problems, where the scatterers are fixed and the boundary condition corresponds to a movable point source. Using a least square method, we can obtain the scattering T-matrix for an assembly of atoms (s-wave point scatterers) on a surface; and thus the off-diagonal elements of the Green's function just from the knowledge of the one-tip data. Therefore, transport property measurements such as that suggested by Niu et al. can be predicted solely from the one-tip data. Moreover, simple formulae relating Green's functions for similar configurations of scatterers are found. Quantum billiards on GaAs/AlGaAs heterostructures provide a great physical system simulating mathematical hard walls. In a perfect situation, the conductance of a coherent backscattering experiment should show an Aharonov-Bohm like oscillation as the magnetic field is varied. However, the observations shows otherwise. A model with impurities has been built to match the observations. Further, theories of proximity resonance in 2D and the scattering off atom wall have been investigated. The former proves the existence of 2D proximity resonance. The latter yields the transmittivity and reflectivity of infinite and finite walls as well as the first band structure study of a finite object embedded in a higher dimension.

Contents

1 **Introduction** **1**

2 **Formalism** **3**

2.1 Introduction 3

2.2 Scattering Theory in 2D 3

2.2.1 Partial Wave Expansion and Results for Elastic Scattering . . 4

2.2.2 Inelastic Scattering 6

2.2.3 Relation between the Phase Shift and the Scattering Length in 2D at low energy 8

2.3 Multiple Scattering Theory 18

2.4 Boundary Wall Method 22

3 **Theories of STM experiment** **25**

3.1 Theory of STM with One and Many Tips 25

3.1.1 N Coherent Tips 26

3.1.2 Niu's Two Tip Experiment 30

4 Models and Results for the One-Tip STM Experiment 34

4.1 Introduction 34

4.2 Review of Quantum Corral Experiment 35

4.3 Multiple Scattering Formalism 35

4.4 Modified Dispersion Relation 37

4.5 Acoustics of the Corrals 37

4.6 Conclusion 40

5 Theory of STM Surface State Electron Scattering off a Step Edge 43

5.1 Introduction 44

5.2 Multiple Scattering Formalism 45

5.3 Scattering off a Step Edge 46

5.4 Scattering off A Step Edge and An Array of Fe Adatoms on Cu(111) 47

5.5 Discussion of Numerical Results 48

5.6 Conclusion 49

6 Two-Tip Results From One-Tip Data and its Variations 54

6.1 Introduction 54

6.2 STM Surface State Electron Scattering:Two-Tip Results from One-Tip Data . . . 55
    6.2.1 Introduction . . . 56
    6.2.2 Review of the Multiple Scattering Theory . . . 57
    6.2.3 Two tip results from one tip data . . . 58
    6.2.4 Two Tip Experiment . . . 61
    6.2.5 Conclusion of Section . . . 62
6.3 Relating Green's functions of similar configurations of scatterers . . . 64
    6.3.1 Missing Scatterer . . . 64
    6.3.2 Added scatterer . . . 66
    6.3.3 Generalization of the Missing Scatterer Formula . . . 67
6.4 Conclusion . . . 70

7 Proximity Scattering, Wall Scattering, and more 71

7.1 Introduction . . . 71
7.2 Picking the Right Atom . . . 72
7.3 Proximity Resonance in 2D . . . 77
    7.3.1 Asymmetric scatterers . . . 81
7.4 Scattering by Small Structures . . . 81

7.5 Scattering by Wall of Scatterers 92
  7.5.1 Infinite Wall of Atoms 92
  7.5.2 Scattering off Finite Walls 96
  7.5.3 8 Atoms Wall 96
  7.5.4 Band Structure of the 8 Atom Wall 98
7.6 Conclusion 98

8 Theories of Coherent Backscattering 108

8.1 Introduction 108
8.2 Review of the Westervelt Experiment 109
8.3 Modeling 110
  8.3.1 Green's Function in the Presence of a B-field 110
  8.3.2 Resistance 111
  8.3.3 Application of the Boundary wall method 112
  8.3.4 Impurities 114
8.4 Conclusion 114

9 Conclusion 118

A Coherent Backscattering Experiment 120

A.1 Determination of the shape of the reflectors 120

List of Figures

3.1 (a) The two-tip experiment suggested by Niu et. al. is schematically shown. The two tips are biased at V_1 and V_2 respectively while the surface is grounded. I_1 and I_2 are the current from the tip to the sample respectively. (b) The cotunneling process from tip one to sample and then to tip two is shown, which contributes to the transconductance component in I_2. 33

4.1 The results by Heller et al of dI/dV vs V for the 60 atoms on a circle with radius of $88.67\mathring{A}$ is shown, compared with the experimental value. 40

4.2 Shown is the dispersion relation with a quartic anharmonicity built in. The effective mass at the bottom of the band is $m_b = 0.352m_e$. The quadratic dispersion relation is plotted as a comparison. 41

4.3 The dI/dV vs V is plotted with the modified dispersion relation with a $m_b = 0.352m_e$. The location of the peaks agree with the experimental curve. 42

5.1 Shown are the components of the total amplitude. (a) This component goes from the tip and reflects normally off the edge back to the tip. (b) This amplitude goes from the tip to the ith scatterer and bounces off all possible paths and finally to the jth scatterer and then back to the tip. (c) Same as (b), except that the wave bounces off the edge before hitting the ith scatterer for the first time. This is equivalent to hitting the image scatterer, $i'th$. (d) Same as (b), except that the wave bounces off the edge before finally getting back to the tip from the jth scatterer. This is equivalent to the amplitude coming from the image scatterer, $j'th$. (e) The amplitude bounces off the edge before hitting the ith scatterer for the first time, and after coming off the jth scatterer for the final time. Again, this is equivalent to scattering from the image scatterers i' and j'. 50

5.2 The scattering off N adatoms with T-matrix of $\beta e^{i\gamma}$ near a step edge can be reduced to the scattering problem with N adatoms and N image adatoms with a T-matrix of $\beta\beta_s e^{i(\gamma+\gamma_s)}$. 51

5.3 Contour plot of LDOS for 2 Fe adatoms, at (2,2) and (2,-2), near the step edge (at $x = 0$) is shown. The edge has a phase shift of $\delta_s = 0$ and an attenuation of $\alpha_s = .4$. This pattern is insensitive to the variation of real part of the phase shift. (The scale is measured in terms of the wavelength.) 52

5.4 Contour plot of LDOS for 24 Fe adatoms, located uniformly on a semicircle of radius 4 wavelengths and centered at (2,0) near the step edge (at $x = 0$), is shown. (The scale is measured in terms of the wavelength.) The plots corresponds to the following attenuation and phase shift for the edge: (a) $\alpha_s = .4$, $\delta_s = \pi$, (b)$\alpha_s = .4$, $\delta_s = .95\pi$, (c) $\alpha_s = .4$, $\delta_s = 0$, $\alpha_s = .4$, $\delta_s = \pi/4$. By inspection, there are distinctive features for each of the plot. 53

6.1 $\text{Im}[i\mathcal{G}(\vec{r}_1, \vec{r}_2, \epsilon)]$ is plotted against x, where $\vec{r}_1 = (x, 0)$ and $\vec{r}_2 = (165, 165)$ (in Å). The energy is at $\epsilon = .45eV$. 60 Fe adatoms are located in a circle of radius $292.84\mathring{A}$ centered at $(0., 0.)$. The exact data is compared to the inversion results with noisy data with a Gaussian error of 10%. In fact, the inversion data without noise agrees with the exact one within line width. 63

7.1 This is the single atom scattering cross section with a resonance at $k = .05$, a width of .000625, and no background ($R_0 = 0$). 75

7.2 This is the single atom scattering cross section with a resonance at $k = .05$, a width of .000625, and $R_0 = 1$. 76

7.3 This is the cross section for quantum proximity resonance with no background. The single atom scattering cross section has a resonance at $k = .05$, a width of .000625, and $R_0 = 0$. 82

7.4 This is the cross section for quantum proximity resonance with background. The single atom scattering cross section has a resonance at $k = .05$, a width of .000625, and $R_0 = 1$. 83

7.5 This is the cross section for quantum proximity resonance with background. The single atom scattering cross section has a resonance at $k = .05$, a width of .000625, and $R_0 = 10$. 84

7.6 The resonance energy for the S-wave and P-wave cross section is plotted against the separation $k_0 d$. 85

7.7 The resonance width for the S-wave and P-wave cross section is plotted against the separation $k_0 d$. 86

7.8 This is the S-wave cross section for quantum proximity resonance with no background for 2 asymmetric scatterers. The single atom scattering cross section has a resonance at $k = .05$, a width of .000625 and 0.000484, and $R_0 = 0$. 87

7.9 This is the P-wave cross section for quantum proximity resonance with no background for 2 asymmetric scatterers. The single atom scattering cross section has a resonance at $k = .05$, a width of .000625 and 0.000484, and $R_0 = 0$. 88

7.10 This is the S-wave cross section for 2-8 atoms on a circle with radius 1, with no background scattering. The single atom scattering cross section has a resonance at $k = .05$, a width of .000625, and $R_0 = 0$. . 90

7.11 This is the P-wave cross section for 3-8 atoms on a circle with radius 1, with no background scattering. The single atom scattering cross section has a resonance at $k = .05$, a width of .000625, and $R_0 = 0$. . 91

7.12 The transmittivity and reflectivity of an infinite wall of scatterers are plotted against k. The scatterers are spaced at d away from one another. The single scatterer cross section has a peak at $k_0 = 0.05$ and a width of 0.000625. Again, the incident plane wave is 1 radian to the normal of the wall. 95

7.13 Shown is the transmittivity through a wall of 8 atoms. 99

7.14 Shown is the reflectivity through a wall of 8 atoms. 100

7.15 The s-wave and d-wave cross sections for a wall of 8 atoms is shown. . 101

7.16 The p-wave cross section for a wall of 8 atoms is shown. 102

7.17 The total cross section for a wall of 8 atoms is shown. 103

7.18 The wavefunction at p-wave resonance, $k = 0.0514135$, for a wall of 8 atoms is shown. This shows p-wave characteristics. 104

7.19 The wavefunction at s-wave and d-wave resonance, $k = 0.051175$, for a wall of 8 atoms is shown. This shows s-d mixed characteristics. . . . 105

7.20 The wavefunction at a non-resonance energy for a wall of 8 atoms is shown. The amplitude along the wall is not as big as the ones on resonance. 106

7.21 The energy vs wavevector of the S-wave resonance states are plotted. 107

7.22 The energy vs wavevector of the P-wave resonance states are plotted. 107

8.1 The resistance vs magnetic field for the given experimental set up is shown. 115

8.2 Shown is the results of the theory with no impurities. 116

8.3 Shown is the comparison of theory with the impurities and the experimental results. 117

A.1 The schematic of the reflector is shown. The gate is along the y axis. 122

Chapter 1

Introduction

Quantum Chaos has been the Holy Grail for experimentalists and theorists alike. While striving to find systems that exhibits such phenomona, recently, people have built "Quantum Corral"[cro93Na, hel94] on Cu(111) as well as ballistic billiards on GaAs/AlGaAs heterostructures.

The "Quantum Corral" utilizes the STM and has probed the surface struture atom by atom. However, instead of the chaotic wavefunction that one might expect for a stadium shape corral, only standing wave patterns are observed. The setback is due to the choice of the material for the corral "wall". The experimentalists picked Fe adatoms. Unfortunately, the Fe adatoms act more like pillows than bricks. Therefore, the Q of the cavity is very low and is inadequate to observe quantum chao as chaos needs to look at long term behaviors of trajectories. This could be explained by a parametrized multiple scattering theory[hel94]. Despite the temporary setback, the "Quantum Corral" experiment has inspired many interesting projects to study. First, the one tip STM can provide information about the local density of states of electrons all over the surface. And one might want to extract more than local properties from such numbers. Therefore, we find a method of getting the results of a two-tip STM experiment from just the one-tip results. Further, one might want to play with the

Green's function a little more. We have discovered simple formulae relating Green's functions for similar configurations of scatterers.

While investigating multiple scattering theory, we have discovered an interesting proximity resonance when we put two S-wave scatterers are put very close together. Moreover, the STM also guided us towards the study of scattering off real atomic walls. Although mathematical walls have been studied by many, the atomic walls are generally unexplored. The atomic walls are important in the sense that the world is actually molecular.

Lastly, we will move on to a system with mathematical walls. The experiments performed on GaAs/AlGaAs provide a great physical system simulating the hard walls. In particular, we are interested in a coherent backscattering experiment performed in the Westervelt group[kat96]. We try to model for the observed dependence of the resistance on the perpendicular magnetic field.

Chapter 2

Formalism

2.1 Introduction

In this chapter, I am going to review some background material. My research consists of building models for the STM Quantum Corral Experiments[cro93Na, has93, cro93Sc, avo90], its variations[chan97, niu95], and the Conductance Fluctuation Experiments[kat96]. All these requires multiple scattering theory. As a result, there are three main topics that need to be studied. First, scattering formalism in 2D has to be reviewed because the physical systems considered are all 2D systems. The second topic is the bread and butter of my research: multiple scattering theory. Lastly, the boundary wall method[luz97] has to be mentioned because it provides a very convenient way to simulate a mathematical hard wall.

2.2 Scattering Theory in 2D

The study of multiple scattering theory should begin with the study of scattering theory per se. In particular, since all of the systems that I consider are two dimensional systems, it would help to re-derive the formalism for the 2D scattering theory. In the presence of a potential, the wavefunction can be written as:

$$\psi(\vec{r}) = e^{i\vec{k}\cdot\vec{r}} + \sum_{l=-\infty}^{l=\infty} \frac{e^{2i\delta_l}-1}{2} H_l^{(1)}(kr) e^{il\phi} e^{il\pi/2} \tag{2.1}$$

$$= \sum_{l=-\infty}^{l=\infty} (\frac{e^{2i\delta_l}}{2} H_l^{(1)}(kr) + \frac{1}{2} H_l^{(2)}(kr)) e^{il\phi} e^{il\pi/2} \tag{2.2}$$

,where $S_l \equiv e^{2i\delta_l}$. $S_l = 1$ and $\delta_l = 0$ corresponds to the trivial case of $V(\vec{r}) = 0$.

To study the optical theorem and the like, we have to go to the limit where the distance is much larger than the wavelength. In the limit of large kr,

$$H_l^{(1)}(kr) \rightarrow \sqrt{\frac{2}{\pi kr}} e^{i(kr-\pi/4-l\pi/2)} \tag{2.3}$$

$$H_l^{(2)}(kr) \rightarrow \sqrt{\frac{2}{\pi kr}} e^{-i(kr-\pi/4-l\pi/2)} \tag{2.4}$$

Therefore, the wavefunction can be rewritten as:

$$\psi(\vec{r}) \rightarrow \sqrt{\frac{1}{2\pi kr}} \sum_{l=-\infty}^{l=\infty} (e^{2i\delta_l} e^{i(kr-\pi/4)} + e^{-i(kr-\pi/4-l\pi)}) \tag{2.5}$$

The wavefunction at large distance in terms of the scattering amplitude is:

$$\psi(\vec{r}) \rightarrow e^{i\vec{k}\cdot\vec{r}} + f(\phi) \frac{e^{ikr}}{\sqrt{r}} \tag{2.6}$$

2.2.1 Partial Wave Expansion and Results for Elastic Scattering

Likewise, we can expand the scattering amplitude into partial waves:

$$f(\phi) = \sum_{l=-\infty}^{l=\infty} f_l e^{il\phi} \tag{2.7}$$

Then the asymtoptic form of the wavefunction becomes:

$$\psi(\vec{r}) \to \sqrt{\frac{1}{2\pi kr}} \sum_{l=-\infty}^{l=\infty} ((1+\sqrt{2\pi k}e^{i\pi/4} f_l)e^{i(kr-\pi/4)} + e^{-i(kr-\pi/4-l\pi)}) \tag{2.8}$$

In other words,

$$S_l = 1 + \sqrt{2\pi k}e^{i\pi/4} f_l = e^{2i\delta_l} \tag{2.9}$$

The scattering amplitude in terms of the phase shift is therefore given by:

$$\begin{aligned} f_l &= \frac{e^{2i\delta_l}-1}{\sqrt{2\pi k}} e^{-i\pi/4} && (2.10) \\ &= \sqrt{\frac{2}{\pi k}} e^{i\pi/4} e^{i\delta_l} \sin\delta_l && (2.11) \end{aligned}$$

The total elastic scattering cross section is:

$$\begin{aligned} \sigma_{total} &= \int_{-\pi}^{\pi} |f(\phi)|^2 d\phi && (2.12) \\ &= \frac{2}{\pi k} \int_{-\pi}^{\pi} \sum_{ll'} e^{i(\delta_l - \delta_{l'})} \sin\delta_l \sin\delta_{l'} e^{i(l-l')\phi} d\phi && (2.13) \\ &= \frac{2}{\pi k} 2\pi \sum_l \sin^2\delta_l && (2.14) \\ &= \frac{4}{k} \sum_l \sin^2\delta_l && (2.15) \end{aligned}$$

because of the orthogonality of $e^{il\phi}$.

Note that the scattering amplitude for forward scattering gives:

$$\mathrm{Im}(f(\phi = 0)e^{-i\pi/4}) = \sqrt{\frac{2}{\pi k}} \sum_l \sin^2 \delta_l \tag{2.16}$$

Consequently,

$$\sigma_{total} = \sqrt{\frac{8\pi}{k}} \mathrm{Im}(f(\phi = 0)e^{-i\pi/4}) \tag{2.17}$$

2.2.2 Inelastic Scattering

So far, only the case of elastic scattering is considered. What if the phase shift is complex? In that case, the scattering S-matrix is of a more general form:

$$S_l = \alpha_l e^{2i\delta_l} \tag{2.18}$$

where both δ_l and α_l are real. α_l is the attenuation due to the potential. In the presence of inelasticity, equation (2.9) becomes:

$$S_l = 1 + \sqrt{2\pi k} e^{i\pi/4} f_l = \alpha_l e^{2i\delta_l} \tag{2.19}$$

The inelasticity is due to other degrees of freedom in the physical scatterer. And by tracing over those channels, one can obtain an effective phase shift, gernerally complex, for the scatterer. Likewise,

$$f_l = \frac{e^{-\pi/4}}{\sqrt{2\pi k}} (\alpha_l e^{2i\delta_l} - 1) \tag{2.20}$$

Again, the elastic cross section is:

$$
\begin{aligned}
\sigma_e &= \int_{-\pi}^{\pi} d\phi |f(\phi)|^2 && (2.21)\\
&= \frac{1}{k}\sum_l |S_l - 1|^2 = \frac{1}{k}\sum_l |\alpha_l e^{2i\delta_l} - 1|^2 && (2.22)
\end{aligned}
$$

As mentioned before, α_l caused an attenuation in the amplitude. For each channel, the ratio of the outgoing wave to the incoming is $\alpha_l^2 = |S_l|^2$. Therefore, the probability of being inelastically scattered in channel l is $1 - \alpha_l^2 = 1 - |S_l|^2$. The cross section due to such processes is:

$$
\sigma_r = \frac{1}{k}\sum_l (1 - |S_l|^2) \qquad (2.23)
$$

Summing up the elastic and the inelastic cross section, the total cross section is:

$$
\begin{aligned}
\sigma_{total} &= \sigma_e + \sigma_r && (2.24)\\
&= \frac{1}{k}\sum_l (|S_l - 1|^2 + 1 - |S_l|^2) && (2.25)\\
&= \frac{2}{k}\sum_l (1 - \mathrm{Re} S_l) && (2.26)
\end{aligned}
$$

Again, $S_l = 1$ is the case with $V(\vec{r}) = 0$, and S_l corresponds to total absorption. Now that we have the total cross section, it would be nice to search for a generalized optical theorem in the presence of inelasticity. The forward scattering amplitude is:

$$
f(\phi = 0) = \sum_l \frac{e^{-i\pi/4}}{\sqrt{2\pi k}}(S_l - 1) \qquad (2.27)
$$

The imaginary part of the product this quantity and the phase in equation (2.16) is:

$$\begin{aligned}\mathrm{Im}(f(\phi=0)e^{-i\pi/4}) &= \frac{1}{\sqrt{2\pi k}}\mathrm{Im}(i-iS_l) && (2.28)\\ &= \frac{1}{\sqrt{2\pi k}}(1-\mathrm{Re}S_l) && (2.29)\\ &= \sqrt{\frac{k}{8\pi}}\sigma_{total} && (2.30)\end{aligned}$$

This yields the generalized form of the optical theorem in 2D.

2.2.3 Relation between the Phase Shift and the Scattering Length in 2D at low energy

In 3D, at low energy, the phase shift goes like ka, where a is the scattering length [sak]. I will try to emulate the same derivation for the 2D case.

Hard Disk Potential

First, consider the scattering off a hard disc in 2D. In other words, we have a potential:

$$V(r) = \{ \begin{array}{cc} 0 & r > R \\ \infty & r < R \end{array} \tag{2.31}$$

With an incident plane wave, the wavefunction should be like:

$$\psi(\vec{r}) = e^{i\vec{k}\cdot\vec{r}} + \sum_{l=-\infty}^{l=\infty} \frac{e^{2i\delta_l}-1}{2} H_l^{(1)}(kr)e^{il\phi}e^{il\pi/2} \tag{2.32}$$

Expanding the plane wave in terms of Bessel functions, we have:

$$e^{i\vec{k}\cdot\vec{r}} = \sum_{l=-\infty}^{\infty} \frac{1}{2}(H_l^{(1)}(kr) + H_l^{(2)}(kr))e^{il\phi}e^{il\pi/2} \tag{2.33}$$

Then, equation (2.32) becomes:

$$\psi(\vec{r}) = \sum_{l=-\infty}^{\infty} (\frac{e^{2i\delta_l}}{2} H_l^{(1)}(kr) + \frac{1}{2} H_l^{(2)}(kr)) e^{il\phi} e^{il\pi/2} \equiv \sum_{l=-\infty}^{\infty} A_l(r) e^{il\phi} e^{il\pi/2} \tag{2.34}$$

For a hard disc, the wavefunction has to vanish at $r = R$. In other words,

$$A_l(R) = e^{i\delta_l}[\cos\delta_l J_l(kR) - \sin\delta_l Y_l(kR)] = 0 \tag{2.35}$$

Therefore,

$$\tan\delta_l = \frac{J_l(kR)}{Y_l(kR)} \tag{2.36}$$

The scattering t-matrix is thus given by:

$$\begin{aligned} -\frac{i}{4}t &= \frac{e^{2i\delta_l} - 1}{2} && (2.37) \\ &= i\frac{\tan\delta_l(1 + i\tan\delta_l)}{1 + \tan^2\delta_l} && (2.38) \\ &= -\frac{H_l^{(2)}(kR) J_l(kR)}{J_l^2(kR) + Y_l^2(kR)} && (2.39) \\ &= -\frac{J_l(kR)}{H_l^{(1)}(kR)} && (2.40) \end{aligned}$$

Moreover, the partial wave scattering cross section is:

$$\begin{aligned} \sigma_l &= \frac{4}{k}\frac{\tan\delta_l^2}{1 + \tan\delta_l^2} && (2.41) \\ &= \frac{4}{k}\frac{J_l(kR)^2}{J_l(kR)^2 + Y_l(kR)^2} && (2.42) \end{aligned}$$

Cylindrically Symmetric Well/Barrier Potential

For a more general case than the infinite hard disk, we consider the following potential:

$$V(r) = \{ \begin{array}{ll} 0 & r > R \\ V_0 & r < R \end{array} \tag{2.43}$$

$V_0 > 0$ corresponds to a barrier whereas $V_0 < 0$ means a well. The wavefunction outside the range of the potential is again given by equation (2.34). However, as we go inside the range, the wavefunction can only have the regular Bessel's function term. It is due to the singularity of the Neumann's function at the origin. Thus, for $r < R$,

$$\psi(\vec{r}) \propto J_0(k_{in} r), \tag{2.44}$$

where $k_{in} = \frac{\sqrt{2m(E-V_0)}}{\hbar}$ for $E > V_0$ and $k_{in} = i\frac{\sqrt{2m(V_0-E)}}{\hbar}$ for $E < V_0$.

The wavefunction as well as its derivative are continuous across the boundary at $r = R$. Due to the continuity, the logarithmic derivative is therefore continuous. And it has to be true for all of the partial waves.

The logarithmic derivative is:

$$\beta_l = \frac{r}{A_l}\frac{dA_l}{dr}|_{R_0} \tag{2.45}$$

The derivative outside the potential is:

$$\beta_l|_{\text{outside}} = kR\frac{J_l'(kR)\cos\delta_l - Y_l'(kR)\sin\delta_l}{J_l(kR)\cos\delta_l - Y_l(kR)\sin\delta_l} \tag{2.46}$$

The derivative inside the potential is:

$$\beta_l|_{\text{inside}} = k_{in}R\frac{J_l'(k_{in}R)}{J_l(k_{in}R)} \tag{2.47}$$

Consequently,

$$\tan\delta_l = \frac{J_l'(kR) - cJ_l(kR)}{Y_l'(kR) - cY_l(kR)} \tag{2.48}$$

where $c = k_{in}/kJ'(k_{in}R)/J(k_{in}R)$.

For the limit $V_0 \to \infty$, this yields equation (2.36).

Scattering Length or Not?

So far, we have no difficulty emulating the 3D results. However, if we scrutinize the equations a bit more, the logarithmic singularity in the Neumann function can cause trouble when establishing the "idea" of the scattering length. As an analogy to the Sakurai problem for 3D, we define a radial function:

$$u(r) = \sum_l \sqrt{r}A_l(r) \tag{2.49}$$

At the scattering length a, the radial function vanishes, $u(a) = 0$. But the existence of a scattering length at low k is not guaranteed unless we can find an $a(k, V_0, R)$ which varies very slowly with k at low energy. Rewriting the Schrödinger Equation in terms of the $u(r)$, we obtain:

$$\frac{d^2u}{dr^2} + \frac{1}{r^2}(\frac{1}{4} - l^2)u - Vu + k^2u = 0 \tag{2.50}$$

At very low energy, $k \approx 0$, the $l = 0$ term will be the most dominant. Outside the potential, $V = 0$, the equation can be rewritten as:

$$\frac{d^2u}{dr^2} = -\frac{1}{4}\frac{u}{r^2} \tag{2.51}$$

And the solution to such equation has to be of the form:

$$u(r) = c_1\sqrt{r} + c_2\sqrt{r}ln(r) \tag{2.52}$$

,where c_1,c_2 are constants.

At the scattering length a, $u(a) = 0$. Thus,

$$ln(a) = -\frac{c_1}{c_2} \tag{2.53}$$

Therefore,

$$\begin{aligned} u(r) &= c_1\sqrt{r}(1 - \frac{lnr}{lna}) && (2.54) \\ &= c_3\sqrt{r}ln(a/r) && (2.55) \end{aligned}$$

,where $c_3 = c_1/ln(a)$ is a constant.

Rephrasing this in terms of A_0,

$$A_0(r) = c_3 ln(a/r) \tag{2.56}$$

The logarithmic derivative defined in equation (2.45) yields:

$$\beta_l|_{\text{outside}} = \frac{1}{ln(a/R)} \tag{2.57}$$

Again, this has to be continuous over the boundary at $r = R$. If the potential is attractive, $V_0 < 0$, then the inside solution of the form:

$$A_0(r) \propto J_0(k_{in}r) \tag{2.58}$$

,where $k_{in} = \sqrt{2m|V_0|}/\hbar$. As mentioned before, the Neumann's function has a singularity at the origin and is invalid for this region. Likewise, the solution inside for repulsive potential, $V_0 > 0$, the inside solution should look like:

$$A_0(r) \propto I_0(k_{in}r) \tag{2.59}$$

The K_0 solution is rejected because of its logarithmic singularity at the origin as well.

The logarithmic derivative from the inside is:

$$\beta_l|_{\text{inside}} = \{ \begin{array}{ll} -k_{in}RJ_1(k_{in}R)/J_0(k_{in}R) & V_0 < 0 \\ k_{in}RI_1(k_{in}R)/I_0(k_{in}R) & V_0 > 0 \end{array} \tag{2.60}$$

As a result, the scattering length is:

$$a(V_0, R) = \{ \begin{array}{ll} Re^{-J_0(k_{in}R)/(k_{in}RJ_1(k_{in}R))} & V_0 < 0 \\ Re^{I_0(k_{in}R)/(k_{in}RI_1(k_{in}R))} & V_0 > 0 \end{array} \tag{2.61}$$

As we take the limit $V_0 \to \infty$, the scattering length goes to R, $a \to R$. This is the hard disk limit. Again, if we take $V_0 \to -\infty$, the scattering length becomes R again.

Although we have established a definition for the scattering length a, we have yet express the cross section in terms of it.

As $k \to 0$,

$$\frac{u'(r)}{u(r)} = -\frac{1}{r}(\frac{1}{2} + \frac{1}{\ln(a/r)}) \tag{2.62}$$

Outside the range of the potential $r > R$,

$$u(r) = \sqrt{r}A_0(r) = e^{i\delta_0}\cos(kr - \frac{\pi}{4} - \delta_0) \tag{2.63}$$

Therefore,

$$\frac{u'(r)}{u(r)} = -k\cot(kr - \frac{\pi}{4} - \delta_0) \tag{2.64}$$

Consequently,

$$kr\cot(kr - \frac{\pi}{4} - \delta_0) = (\frac{1}{2} + \frac{1}{\ln(a/r)}) \tag{2.65}$$

Or, using equation (2.46),

$$\tan\delta_l = \frac{J_l'(kR) - cJ_l(kR)}{Y_l'(kR) - cY_l(kR)} \tag{2.66}$$

, where $c = \beta/kR$. Let $z = kR$. Then, as $z \to 0$,

$$\begin{aligned} \cot\delta_0 &= \frac{-\frac{2}{\pi z}\ln z + \frac{2\beta}{\pi z}\ln z}{\frac{z}{2} + \frac{\beta}{z}} \quad (2.67) \\ &= \frac{2}{\pi}(-\frac{1}{\beta} + \ln z) \quad (2.68) \end{aligned}$$

And using equation (2.57), $1/\beta = \ln(a/R)$. Thus,

$$\cot\delta_0 = \frac{2}{\pi}\ln(kR)(1 - \ln(a/R)) \tag{2.69}$$

As a result, the scattering cross section still tends to infinity as $1/k$ because $\sqrt{k} \to 0$ much faster then $1/\text{ln}k$ as $k \to 0$.

"Resonance" Scattering

In addition to the plain well/barrier potential that we have looked at, we might like to study a variation of that potential:

$$V(r) = \{ \begin{array}{ll} 0 & r > R_2 \\ V_2(> E) & R_1 < r < R_2 \\ V_1(< 0) & r < R_1 \end{array} \tag{2.70}$$

This potential is interesting because at low energy E, there will be resonance scattering if the energy matches that of a "bound state" inside $r < R_1$. Like equation (2.34), we can write the wavefunction in terms of the radial wavefunction $A_l(r)$ for $r > R_2$:

$$\psi(\vec{r}) = \sum_{l=-\infty}^{\infty} (\frac{e^{2i\delta_l}}{2} H_l^{(1)}(kr) + \frac{1}{2} H_l^{(2)}(kr)) e^{il\phi} e^{il\pi/2} \equiv \sum_{l=-\infty}^{\infty} A_l(r) e^{il\phi} e^{il\pi/2} \tag{2.71}$$

At low energy, only the s-wave component needs to be considered. At $r = R_2$, the logarithmic derivative for $l = 0$ is:

$$\beta_0|R_2 = kR_2 \frac{-J_1(kR_2)\cos\delta_0 + Y_1(kR_2)\sin\delta_0}{J_0(kR_2)\cos\delta_0 - Y_0(kR_2)\sin\delta_0} \equiv \frac{1}{\ln(a/R_2)} \tag{2.72}$$

At $r < R_1$, $A_0(r) \propto J_0(k_1 r)$, where $k_1 = \frac{\sqrt{2m(E-V_1)}}{\hbar}$. Therefore, the logarithmic derivative at $r = R_1$ is:

$$\beta_0|R_1 = -\frac{k_1 R_1 J_1(k_1 R_1)}{J_0(k_1 R_1)} \tag{2.73}$$

As $E < V_2$, at $R_1 < r < R_2$, $A_0(r) = c_1 I_0(k_2 r) + c_2 K_0(k_2 r)$, where $k_2 = \frac{\sqrt{2m(V_2-E)}}{\hbar}$. Thus, $A_0'(r) = c_1 I_1(k_2 r) - c_2 K_1(k_2 r)$. The logarithmic derivative is:

$$\beta_0|r = A_0'/A_0 \times r = k_2 r \frac{c_1 I_1(k_2 r) - c_2 K_1(k_2 r)}{c_1 I_0(k_2 r) + c_2 K_0(k_2 r)} \tag{2.74}$$

Since the wavefunction is continous, the logarithmic derivative has to match at the boundaries $r = R_1$ and $r = R_2$ respectively. Matching equation (2.74) and equation (2.73) at $r = R_1$ gives:

$$\frac{c_1}{c_2} = \frac{K_1(k_2 R_1) - \frac{k_1 J_1(k_1 R_1)}{k_2 J_0(k_1 R_1)} K_0(k_2 R_1)}{I_1(k_2 R_1) + \frac{k_1 J_1(k_1 R_1)}{k_2 J_0(k_1 R_1)} I_0(k_2 R_1)} \tag{2.75}$$

Substituting this into equation (2.73) yields the correct logarithmic derivative at $r = R_2$:

$$\beta_0|R_2 = k_2 R_2 \frac{c_1/c_2 I_1(k_2 R_2) - K_1(k_2 R_2)}{c_1/c_2 I_0(k_2 R_2) + K_0(k_2 R_2)} \tag{2.76}$$

Matching this with the wavefunction outside the potential at $r = R_2$, we have:

$$\tan\delta_0 = \frac{J_1(kR_2) + \beta_0|R_2/(kR_2) J_0(kR_2)}{Y_1(kR_2) + \beta_0|R_2/(kR_2) Y_0(kR_2)} \tag{2.77}$$

Resonance scattering will occur when the energy matches that of a bound state within $r < R_1$. This occurs when $\delta_0 = \pi/2$.

Thus far, we have presented a review of 2D scattering theory. To model for the STM and billiard experiments, we need to move one step further and use multiple scattering theory, which will be our next topic, to account for the multiple bounces off the scatterers.

2.3 Multiple Scattering Theory

Waves scatterer off barriers. There are situations where the barriers are well-separated from each other that wave propagates freely before encountering another barrier. In these cases, multiple scattering theory applies. In particular, we are interested in s-wave point scatterers. Despite its mathematical simplicity, s-wave point scatterers provide good models for many physical system where the wavelength is much larger the scattering length. For instance, the Fe adatoms on Cu(111) surface can be modeled by 2D electron wave scattering off s-wave scatterers.

Multiple scattering by an array of scatterers accounts for scattering to infinite orders. In other words, it includes all number of bounces on each scatterer. Real scatterer has a physical dimension, and wave can scatter within. There is trouble if we keep track of the "order" in terms of the strength of the potential V because the propagator to within the scatterer itself has a very large magnitude. Fadeev equation uses the "renormalized" strength, and includes all orders of bounces within one single scatterer without leaving in the "bare" scattering T-matrix. And we keep track of the order in terms of the T-matrix instead.

To jump from a real scatterer to a point scatterer in 2D seems trivial, but is in fact philosophically painful. As we know, a delta function in 2D has no scattering cross section (or length) at all. The mathematical "point" scatterer that we are going to use in our theory preserves the scattering length of the physical scatterer it wants to model. But the potential is localized to one single point. To use this approximation, as we will see, it is much better to work with T-matrix than with V. And the "bare" T-matrix is defined to be the ratio of the outgoing flux to the incoming flux.

From Schrödinger equation,

$$\psi = \psi^0 + \mathcal{G}^0 V \psi = \psi^0 + \mathcal{G}^0 T \psi^0 \tag{2.78}$$

$$\mathcal{G} = \mathcal{G}^0 + \mathcal{G}^0 V G = \mathcal{G}^0 + \mathcal{G}^0 T \mathcal{G}^0 \tag{2.79}$$

$$T = V + V \mathcal{G}^0 T \tag{2.80}$$

$$T = (I - V\mathcal{G}^0)^{-1} V \tag{2.81}$$

Since V is localized,

$$V(\vec{r}) = \sum_i V_i \delta(\vec{r} - \vec{r_i}) \tag{2.82}$$

Therefore, expanding equation (2.81) (including infinite orders of scattering),

$$\begin{aligned} \langle \vec{r} | T | \vec{r'} \rangle &= V_i \delta(\vec{r} - \vec{r_i}) \delta(\vec{r'} - \vec{r_i}) + V_i \delta(\vec{r} - \vec{r_i}) \mathcal{G}^0_{ij} V_j + \cdots & (2.83) \\ &\equiv \mathcal{T}_{ij} \delta(\vec{r} - \vec{r_i}) \delta(\vec{r} - \vec{r_j}) & (2.84) \end{aligned}$$

The first term of equation (2.83) corresponds to one bounce on the i^{th} scatterer, and the second term corresponds to a bounce on the i^{th} scatterer and then a bounce on the j^{th}, and so on. Using equation (2.84), the second term of equation (2.80) becomes:

$$\langle \vec{r} | V \mathcal{G}^0 T | \vec{r'} \rangle = V_i \delta(\vec{r} - \vec{r_i}) \mathcal{G}^0_{ik} \mathcal{T}_{kj} \delta(\vec{r'} - \vec{r_j}) \tag{2.85}$$

And equation (2.80) per se becomes:

$$\mathcal{T}_{ij}\delta(\vec{r}-\vec{r_i})\delta(\vec{r'}-\vec{r_j}) = V_i\delta(\vec{r}-\vec{r_i})\delta(\vec{r'}-\vec{r_i}) + V_i\mathcal{G}^0_{ik}\mathcal{T}_{kj}\delta(\vec{r}-\vec{r_i})\delta(\vec{r'}-\vec{r_j}) \tag{2.86}$$

Removing the delta functions yields:

$$\begin{aligned}
\mathcal{T}_{ij} &= V_i\delta_{ij} + V_i\mathcal{G}^0_{ik}\mathcal{T}_{kj} && (2.87)\\
&= V_i\delta_{ij} + \sum_{k\neq i} V_i\mathcal{G}^0_{ik}\mathcal{T}_{kj} + V_i\mathcal{G}^0_{ii}\mathcal{T}_{ij} && (2.88)
\end{aligned}$$

$$\mathcal{T}_{ij} = (1 - V_i\mathcal{G}^0_{ii})^{-1}V_i\delta_{ij} + (1 - V_i\mathcal{G}^0_{ii})^{-1}V_i\sum_{k\neq i}\mathcal{G}^0_{ik}\mathcal{T}_{kj} \tag{2.89}$$

Let $t_i = (1 - V_i\mathcal{G}^0_{ii})^{-1}V_i$. Thus far, the "bounces" that we refer to can be within the scatterer itself. But as soon as you look at the quantity t_i, one smells trouble because if we have a point scatterer, $\mathcal{G}_{ii}$ simply blows up logarithmically. To avoid dealing with this "non-physical" singularity, we try to work with t_i instead of V_i. This t_i is usually called the "bare" scattering T-matrix ("bare" in the sense that we ignore scattering with other scatterers). And it is the ratio of the outgoing flux to the incoming flux (preserving the properties of the "real" scatterer). Then equation (2.89) can be rewritten as:

$$\begin{aligned}
\mathcal{T}_{ij} &= t_i\delta_{ij} + t_i\sum_{k\neq i}\mathcal{G}^0_{ik}\mathcal{T}_{kj} && (2.90)\\
&= t_i\delta_{ij} + t_i(1-\delta_{ki})\mathcal{G}^0_{ik}\mathcal{T}_{kj} && (2.91)
\end{aligned}$$

Let $A_{ij} = t_i\mathcal{G}^0_{ij}(1-\delta_{ij})$. Once again, we see that A_{ij} has zero diagonal elements. This is because the t_i has already included infinite order of bounces within the scatterer. By rewriting things in terms of A, we have:

$$\mathcal{T} = \mathbf{Diag(t)} + \mathbf{A}\mathcal{T} \tag{2.92}$$

This implies:

$$\mathcal{T} = (\mathbf{I} - \mathbf{A})^{-\mathbf{1}}\mathbf{Diag(t)} \equiv \mathbf{B} \tag{2.93}$$

Therefore, in the position representation,

$$\psi(\vec{r}) = \psi^0(\vec{r}) + \sum_{ij} \mathcal{G}^0(\vec{r}, \vec{r_i}) B_{ij} \psi^0(\vec{r_j}) \tag{2.94}$$

$$\mathcal{G}(\vec{r}, \vec{r'}) = \mathcal{G}^0(\vec{r}, \vec{r'}) + \sum_{ij} \mathcal{G}^0(\vec{r}, \vec{r_i}) B_{ij} \mathcal{G}^0(\vec{r_j}, \vec{r'}) \tag{2.95}$$

These two equations provide a convenient way to treat a multiple scattering problem. The seemingly complicated problem with N scatterers scattering to infinite orders can now be reduced to a matrix inversion and two matrix multiplications, which can be done very easily with computers.

2.4 Boundary Wall Method

There are so many different methods solving the Helmholz equation in 2D with an arbitrary boundary condition. However, methods such as the boundary integral method are difficult to handle numerically and fail to work in many cases. In particular, the problem that we are interested in is the case with:

$$(\nabla^2 + k^2)\psi(\vec{r}) = 0 \tag{2.96}$$

, and $\psi(\vec{r_s}) = 0$ where $\vec{r_s}$ is on the wall. Instead of dealing with normal derivatives and stuff like that, the boundary wall method[luz97] puts an infinitely tall delta function wall on the boundary:

$$V(\vec{r'}) = \int ds \lambda(s) \delta(\vec{r'} - \vec{r_s}) \tag{2.97}$$

, where $\lambda(s) \to \infty$, $\vec{r_s}$ is on the wall. As we have learned in Quantum Mechanics, an infinitely tall delta function wall is impenetrable. Therefore, this potential $V(\vec{r'})$ satisfies our boundary condition.

We know that

$$\psi(\vec{r}) = \psi^0(\vec{r}) + \int d\vec{r'} \mathcal{G}^0(\vec{r}, \vec{r'}) V(\vec{r'}) \psi(\vec{r'}) \tag{2.98}$$

By substituting equation (2.97) into equation (2.98), we obtain:

$$\psi(\vec{r}) = \psi^0(\vec{r}) + \int ds' \lambda(s') \mathcal{G}^0(\vec{r}, \vec{r_{s'}}) \psi(\vec{r_{s'}}) \tag{2.99}$$

Define $\psi(s) = \psi(\vec{r_s})$, and $\mathcal{G}^0(s,s') = \mathcal{G}^0(\vec{r_s}, \vec{r_{s'}})$. By solving $\psi(s)$, $\psi(\vec{r})$ is known every where else. Evaluating ψ on the the wall, equation (2.99) becomes:

$$\psi(s) = \psi^0(s) + \int ds' \lambda(s') \mathcal{G}^0(s,s') \psi(s') \tag{2.100}$$

However, if we look at the second term of equation (2.100) closely, one finds that $\mathcal{G}^0(s,s')$ is singular when $s = s'$. But this singularity is by no means intractable because it is only logarithmic. If we integrate over s, this singularity can be smoothed out.

So far, we have been dealing with an integral equation. To deal with equation (2.100) numerically, we have to discretize this problem. In other words, we can divide the wall into N equal portion of arc length $\Delta s \equiv \text{Totalarclength}/N$. The segments are centered at $s = s_i$, $i = 1, \cdots, N$. Define $\mathcal{G}^0_{ij} = \int_{s=s_i-\Delta s/2}^{s=s_i-\Delta s/2} ds \mathcal{G}^0(s, s_j)/\Delta s$. Then the discretized version of equation (2.100) is:

$$\psi(s_i) = \psi^0(s_i) + \sum_{ij} \Delta s \lambda(s_j) \mathcal{G}^0_{ij} \psi(s_j) \tag{2.101}$$

Define $\psi_i = \psi(s_i)$, $\lambda_i = \lambda(s_i)$, and $\mathcal{G}^0_{ij} = \mathcal{G}^0(s_i, s_j)$. We have:

$$\psi_i = \psi^0_i + \sum_{ij} \Delta s \lambda_j \mathcal{G}^0_{ij} \psi_j \tag{2.102}$$

This is just a linear equation that we can invert. Define $\lambda_i = \lambda_0 f_i$ (let $\lambda_0 \to \infty$), and $M_{ij} = f_i \mathcal{G}^0_{ij} \Delta s$. Rewriting equation (2.102) in the new notations, and rearranging the terms yields:

$$(\mathbf{I} - \lambda_0 \mathbf{M})\psi = \psi^{\mathbf{0}} \tag{2.103}$$

This implies:

$$\psi = (\mathbf{I} - \lambda_0 \mathbf{M})^{-1} \psi^{\mathbf{0}} \tag{2.104}$$

Plugging this back into equation (2.99) gives:

$$\psi(\vec{r}) = \psi^0(\vec{r}) + \sum_{jk} \mathcal{G}^0(\vec{r}, \vec{r_j}) \Delta s \lambda_j (I - \lambda_0 M)^{-1}_{jk} \psi^0_k \tag{2.105}$$

Since an impenetrable wall requires an infinitely tall delta function, we should let λ_0 goes to infinity. As $\lambda_0 \to \infty$,

$$\mathbf{Diag}(\lambda)(\mathbf{I} - \boldsymbol{\lambda_0}\mathbf{M})^{\mathbf{-1}} \to -\mathbf{Diag}(\mathbf{f})\mathbf{M}^{\mathbf{-1}} \tag{2.106}$$

Let $\mathbf{B} = -\mathbf{Diag}(\mathbf{f})\mathbf{M}^{-1}$. Then

$$\psi(\vec{r}) = \psi^0(\vec{r}) + \sum_{jk} \mathcal{G}^0(\vec{r}, \vec{r_j}) \Delta s B_{jk} \psi^0_k \tag{2.107}$$

$$\mathcal{G}(\vec{r}, \vec{r'}) = \mathcal{G}^0(\vec{r}, \vec{r'}) + \sum_{jk} \mathcal{G}^0(\vec{r}, \vec{r_j}) \Delta s B_{jk} \mathcal{G}^0(\vec{r_j}, \vec{r'}) \tag{2.108}$$

Using this boundary wall method, the mathematical hard wall problem is too reduced to a matrix inversion and two matrix multiplications, just like the multiple scattering theory for localized scatterers. As you can see, the equations,(2.95) and (2.108), for the multiple scattering theory and the boundary wall method are strikingly similar. One can combine these two methods to model for systems with both point scatterers and mathematical hard walls.

Chapter 3

Theories of STM experiment

3.1 Theory of STM with One and Many Tips

The STM experiment has probed the local density of states of electrons on surfaces. Naturally, one would want to know of the transport properties of the surface by building a two tip STM experiment. The two tip STM experiment has so far been the holy grail of experimentalists. The transport properties contain information of the off-diagonal elements of the energy Green's function $\mathcal{G}(\vec{r}, \vec{r'}, \epsilon)$. However we should clarify what STM experiment yields the transport property. For example, in a two tip experiment must the electron amplitude in tip 1 be coherent with that in tip 2? What about electrons going directly into/coming directly from bulk states from each tip?

Although the STM can operate in the differential conductance mode as well as the constant current topograph mode, we are going to look at only the differential conductance mode in my paper. The one tip theory of STM in its original atom-by-atom context was given by Tersoff and Hamann[ter84]. Their calculation has related the differential conductance $\frac{dI}{dV}$ to the local density of states of electron at the tip position and therefore the diagonal Green's function $\mathcal{G}(\vec{r}, \vec{r}, \epsilon)$. We would like to generalize this to an N coherent tip experiment. Then we would like to take a look at another variety of a two tip experiment where one tip is the source and the other is the sink.

Striking as it might seem, after all these hard work of searching for appropriate multiple-tip experiments, I will show you that we don't even need to do the those experiments to find out the transport property. The results of getting the total Green's function from the local density of states will be presented in section 6.2 of chapter 6.

3.1.1 N Coherent Tips

In order to bring the off diagonal elements of the Green's function into the picture, we start with a generalization of Tersoff and Hamann's formalism[ter84] to an N-tip experiment, where the tips, which are wired in parallel, are located at positions $\vec{r_i}$ for $i = 1, \cdots, N$. The total tunneling current from the tips to the surface is given to the first order in Bardeen's formalism[bar62] by

$$I = \frac{2\pi}{\hbar} \sum_{\mu\nu} |M_{\mu\nu}|^2 f(E_\mu)[1 - f(E_\nu)]\delta(E_\mu + eV - E_\nu) \tag{3.1}$$

where $f(E)$ is the Fermi function, V is the applied voltage, $M_{\mu\nu}$ is the tunneling matrix between $|\mu\rangle$ on the tip and $|\nu\rangle$ on the surface, at very low temperature such that $kT \ll eV$. E_μ and E_ν are the energy of the state s $|\mu\rangle$ and $|\nu\rangle$ respectively. The expression for the tunneling matrix $M_{\mu\nu}$ is given by:

$$M_{\mu\nu} = \frac{\hbar^2}{2m} \int d\vec{S} \cdot (\psi_\mu^* \bigtriangledown \psi_\nu - \psi_\nu \bigtriangledown \psi_\mu^*) \tag{3.2}$$

where the integral is taken over any surface that lies entirely within in the vacuum space between the tip and the copper surface. We can see that the integrand is just the current operator. Using the same trick as [ter84], we will expand the surface wave function in the following form:

$$\psi_\nu = \Omega_s^{-1/2} \sum_{\vec{G}} a_{\vec{G}} \exp[(\kappa^2 + |\vec{\kappa_G}|^2)^{1/2} z] \exp[i\vec{\kappa_G} \cdot \vec{x}] \tag{3.3}$$

where Ω_s is the sample volume, $\kappa = \hbar^{-1}(2m\phi)^{1/2}$ is the work function for the copper surface, $\vec{\kappa_G} = \vec{k_\parallel} + \vec{G}$, $\vec{k_\parallel}$ is the surface Bloch wave vector of the state, and $\vec{G}$ is the surface reciprocal lattice vector. This general expression of ψ_ν works for states in a region with a negligible potential. For the tip states $|\mu_i\rangle$ for $i = 1, \cdots, N$, we consider them to have the asymptotic spherical form:

$$\psi_{\mu_i} = \Omega_t^{-1/2} c_t \kappa R e^{\kappa R} \frac{e^{-\kappa|\vec{r}-\vec{r_i}|}}{\kappa|\vec{r}-\vec{r_i}|} \tag{3.4}$$

where R is the radius of curvature of the tip about center $\vec{r_i}$, Ω_t is the volume of the tip. For simplicity sake, all tips have the same radius of curvature, but the formalism can be trivially generalized to tips with different sizes. Furthermore, let us consider the case where all tips are held at a distance d from the surface, which can also be easily generalized to tips at different height.

So far, all of the equations comes from the one tip formalism. To generalize, we assume that we work in a regime that neighboring tips are far enough apart such that $\kappa|\vec{r_i} - \vec{r_j}| \gg 1$. Therefore, we can ignore direct tunneling between the two tips through vacuum. In other words, all the interference between the current in different tips is due to surface wave propagation from one tip to another. That is,

$$\langle \mu_i | \mu_j \rangle = \delta_{ij} \tag{3.5}$$

A single electron state $|\mu\rangle$ has a probability of coming off different tip at a certain phase (due to scattering in the leads):

$$|\mu\rangle = \sum_{j=1}^{N} c_j e^{i\phi} |\mu_j\rangle \tag{3.6}$$

where $\sum_i |c_i|^2 = 1, c_i \in \mathbf{R}, c_i \geq 0, \ \phi_i \in [0, 2\pi)$.

To evaluate $M_{\mu_n u}$, as in [ter84], we use the fact that

$$(\kappa\vec{r})^{-1} e^{-\kappa\vec{r}} = \int d^2q \, b(\vec{q}) e^{-(\kappa^2+q^2)^{-1/2}|z|} e^{i\vec{q}\cdot\vec{x}} \tag{3.7}$$

$$b(\vec{q}) = (2\pi)^{-1}\kappa^{-2}(1 + q^2/\kappa^2)^{-1/2} \tag{3.8}$$

Combining equations (3.2),(3.3)(3.4),(3.6),(3.7), $M_{\mu\nu}$ is easily computed:

$$M_{\mu\nu} = \frac{\hbar^2}{2m} 4\pi\kappa^{-1}\Omega_t^{-1/2}\kappa R e^{\kappa R} \sum_{j=1}^{N} c_j e^{-i\phi_j} \psi_\nu(\vec{r_j}) \tag{3.9}$$

Therefore, the tunneling current is given by

$$I \propto \sum_{\mu\nu} f(E_\mu)[1 - f(E_\nu)]\delta(E_\mu + eV - E_\nu)[\sum_{j=1}^{N} c_j e^{-i\phi_j} \psi_\nu(\vec{r_j}) \sum_{l=1}^{N} c_l e^{i\phi_l} \psi_\nu(\vec{r_l})] \tag{3.10}$$

Consequently,

$$\frac{dI}{dV} \propto \sum_\nu [\sum_{j=1}^{N} c_j e^{-i\phi_j} \psi_\nu(\vec{r_j}) \sum_{l=1}^{N} c_l e^{i\phi_l} \psi_\nu^*(\vec{r_l}) \, \delta(E_F + eV - E_\nu)] \tag{3.11}$$

We use the fact that

$$\sum_\nu \langle\vec{r_l}|\nu\rangle\langle\nu|\vec{r_m}\rangle\delta(E_\nu - \epsilon) \tag{3.12}$$

$$= \quad \tfrac{1}{2\pi\hbar}\mathbf{Re}[i\mathcal{G}(\vec{r_l}, \vec{r_m}, \epsilon)] \tag{3.13}$$

Then the dI/dV can be expressed in terms of the Green's function. For a single tip, the differential cross section is:

$$\frac{dI}{dV} \propto Re[c_1^2 i\mathcal{G}(\vec{r_1}, \vec{r_1}, \epsilon)] \tag{3.14}$$

And for the two tips experiment, the differential cross section is:

$$\frac{dI}{dV} \propto Re[c_1^2 i\mathcal{G}(\vec{r_1}, \vec{r_1}, \epsilon)+c_2^2 i\mathcal{G}(\vec{r_2}, \vec{r_2}, \epsilon)+c_1c_2e^{i(\phi_1-\phi_2)}i\mathcal{G}(\vec{r_2}, \vec{r_1}, \epsilon)+c_1c_2e^{i(\phi_2-\phi_1)}i\mathcal{G}(\vec{r_1}, \vec{r_2}, \epsilon)] \tag{3.15}$$

And the current through tip #1 is:

$$\frac{dI_1}{dV} \propto Re[ic_1^2\mathcal{G}(\vec{r_1}, \vec{r_1}, \epsilon) + c_1c_2e^{i(\phi_1-\phi_2)}i\mathcal{G}(\vec{r_2}, \vec{r_1}, \epsilon)] \tag{3.16}$$

For the case of two coherent identical tips with a relative phase of zero,

$$\frac{dI_1}{dV} \propto Re[i\mathcal{G}(\vec{r_1}, \vec{r_1}, \epsilon) + i\mathcal{G}(\vec{r_2}, \vec{r_1}, \epsilon)] \tag{3.17}$$

If the two tips are incoherent, averaging over the phase, only the contribution from the diagonal elements remains:

$$\frac{dI_1}{dV} \propto Re[i\mathcal{G}(\vec{r_1}, \vec{r_1}, \epsilon)] \tag{3.18}$$

As a result, the single tip STM experiment yields a differential cross section proportional to the imaginary part of the diagonal Green's Function whereas the coherent two tip yields the imaginary part of the sum of the diagonal and the off-diagonal elements. However, the coherent two-tip might be extremely difficult to emulate because it is impossible to make two identical tips. Therefore, we might need to search for another two-tip experiment.

3.1.2 Niu's Two Tip Experiment

In addition to the 2 coherent tip experiment mentioned above, there exist another flavor of two tip experiment, suggested by [niu95]. In this thought experiment, the tips are biased at different voltage. One acts as a source and the other as a sink, with the surface being the media. The setup is schemematically shown on figure 3.1.

The Hamiltonian corresponding to this system is:

$$H = H_1 + H_2 + H_{surface} + M \tag{3.19}$$

where M is the tunneling amplitude from the tip to surface and from surface to tip, H_1,H_2,$H_{surface}$ are the Hamiltonians for the tips and the surface respectively.

Consider the transition from $|\mu_1\rangle$ to $|\mu_2\rangle$. We know $\langle\mu_2|M|\mu_1\rangle = 0$. Let us consider the second order in M.

Using formalism of Raman scattering, we found that rate of going from $|\mu_1\rangle$ to $\langle\mu_2|$ is:

$$\begin{aligned} w_{|\mu_1\rangle\to|\mu_2\rangle} &= \frac{2\pi}{\hbar}\delta(E_{\mu_1} + eV_1 + eV_2 - E_{\mu_2})|\sum_\nu \frac{C_1C_2\langle\vec{r_2}|\nu\rangle\langle\nu|\vec{r_1}\rangle}{E_{\mu_1} + eV_1 - E_\nu + i\hbar\eta}|^2 && (3.20) \\ &= \frac{2\pi}{\hbar}\delta(E_{\mu_1} + eV_1 + eV_2 - E_{\mu_2})|C_1C_2G(\vec{r_1}, \vec{r_2}, E_{\mu_1})|^2 && (3.21) \end{aligned}$$

We know that $\langle\nu|M|\mu_i\rangle = C_i\psi_\nu(r_i)$.

Such transitions contribute to current from 1 → 2:

$$I_{1\to 2} = \frac{2\pi e}{\hbar}\sum_{\mu_1\mu_2}[f(E_{\mu_1})-f(E_{\mu_2})]\delta(E_{\mu_1}+eV_1+eV_2-E_{\mu_2})|C_1C_2G(\vec{r_1},\vec{r_2},E_{\mu_1})|^2 \quad (3.22)$$

Likewise, for transition from $|\mu_1\rangle$ to $|\nu\rangle$ (single tip) , rate is:

$$\begin{aligned} w_{|\mu_1\rangle\to|\nu\rangle} &= \frac{2\pi}{\hbar}\delta(E_{\mu_1}+eV_1-E_\nu)|C_1\psi_\nu(\vec{r_1})|^2 && (3.23)\\ &= \frac{2\pi}{\hbar}\delta(E_{\mu_1}+eV_1-E_\nu)|C_1|^2\frac{1}{\pi}\mathrm{Re}[iG(\vec{r_1},\vec{r_1},E_{\mu_1}+eV_1)] && (3.24)\end{aligned}$$

And these contribute to current between tip 1 and the surface:

$$I_{1\to S} = \frac{2\pi e}{\hbar}\sum_{\mu_1\nu}[f(E_{\mu_1})-f(E_\nu)]\delta(E_{\mu_1}+eV_1-E_\nu)|C_1|^2\frac{1}{\pi}\mathrm{Re}[iG(\vec{r_1},\vec{r_1},E_{\mu_1}+eV_1)] \quad (3.25)$$

Total current between tip 1 and the surface is:

$$I_1 = I_{1\to 2} + I_{1\to S} \quad (3.26)$$

$$\frac{dI_1}{dV_1} = \frac{2\pi e^2}{\hbar}[A_1\frac{1}{\pi}\mathrm{Re}[iG(\vec{r_1},\vec{r_1},E_F+eV_1)] + A_1A_2|G(\vec{r_1},\vec{r_2},E_F+eV_1)|^2] \quad (3.27)$$

where $A_i \equiv C_i^2 g_{\mathrm{tip}}$, g_{tip} = density of states of the tip, $E_1 = E_F + eV_1$, $E_2 = E_F - eV_2$.

Likewise, the transconductance is:

$$\frac{dI_1}{dV_2} = \frac{2\pi e^2}{\hbar}A_1A_2|G(\vec{r_1},\vec{r_2},E_F-eV_2)|^2 \quad (3.28)$$

The transconductance is proportional to the square of the magnitude of the off-diagonal Green's function.

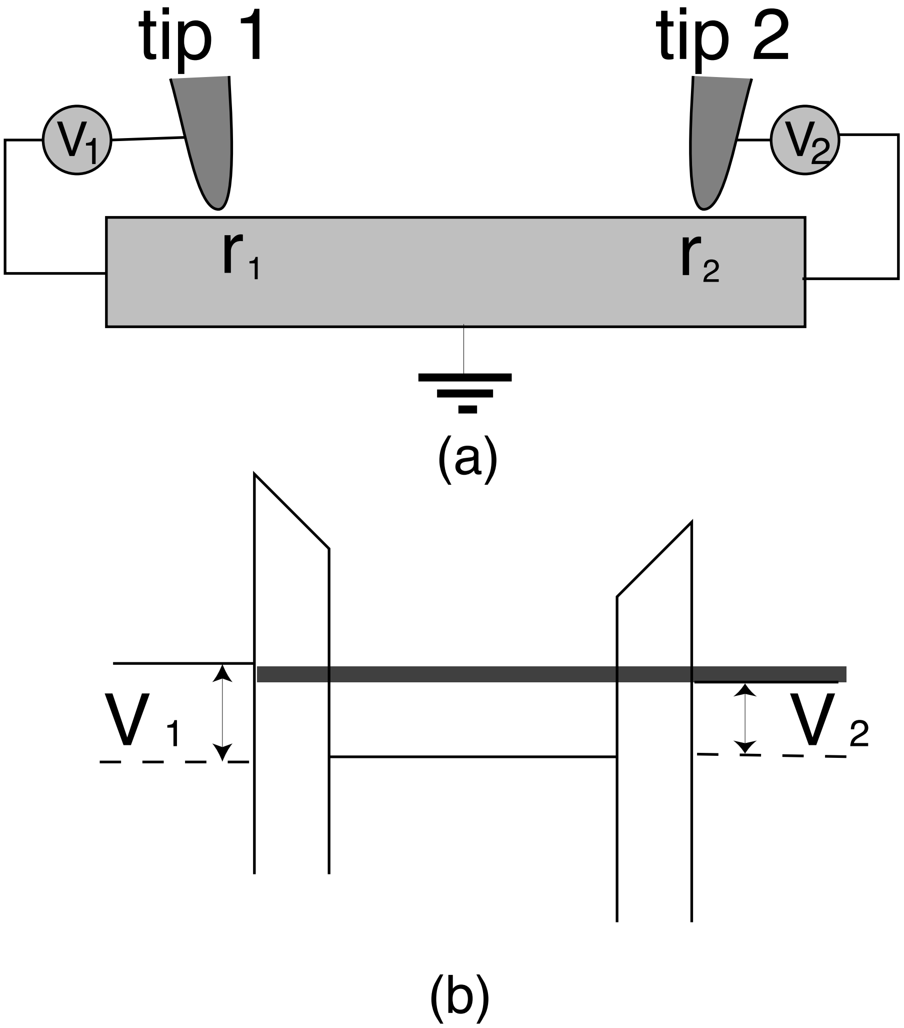

Figure 3.1: (a) The two-tip experiment suggested by Niu et. al. is schematically shown. The two tips are biased at V_1 and V_2 respectively while the surface is grounded. I_1 and I_2 are the current from the tip to the sample respectively. (b) The cotunneling process from tip one to sample and then to tip two is shown, which contributes to the transconductance component in I_2.

Chapter 4

Models and Results for the One-Tip STM Experiment

4.1 Introduction

Quantum Corral experiment by Crommie et al [cro93Na] has been a quest to search for quantum chaos. With Fe adatoms on the surface on Cu(111), where there is a nearly free 2D electron gas, standing wave patterns have been observed for closed fences. Even for the stadium-shaped corral, no chaotic looking wavefunction is observed. Theory by Heller et al [hel94] has explained the low Q of the enclosure has limited the tracing of the trajectory of an electron to only 2-3 bounces, which is inadequate to observe any chaotic behavior. The theory has provided good agreement with the data. Although the fit is phenomenal with the parametrized theory, there are still some places where the fit is noticeably less than perfect. In particular, by using an exact parabolic dispersion relation, the fit for the dI/dV curve above the Fermi energy is shifted quite a bit. Moreover, the width of the peaks in the dI/dV curve has not been explained by any physical means. In this chapter, some fine tunings will be made to the one tip STM model suggested by [hel94]. That would yield a better fit to the dI/dV curve. Further, an acoustic argument will be used to predict the width of the peaks.

4.2 Review of Quantum Corral Experiment

The Quantum Corral experiment[cro93Na] was an STM experiment performed on Cu(111) surface with Fe adatoms located at positions of their wish. Photoelectron Spectroscopy[kev83] has observed surface states on (111) fcc noble metals. Such surface state electrons form a nearly free electron gas, providing a good 2D system to study. The Fermi energy is around 0.45eV above the bottom of the band. If the dispersion curve is fitted with a parabola, it would correspond to an effective mass of $m^* = .38 m_e$.

The corral experiment built closed fence with Fe adatoms. Circles, double circles as well as stadiums have been built in the hope to look for quantum chaos. Yet only standing wave patterns has been observed, even for the chaotic stadium shape.

4.3 Multiple Scattering Formalism

The quantity measured in the STM experiments we consider here[cro93Na, has93, cro93Sc, avo90] is dI/dV, the change of current I with voltage V. A small change in voltage induces current in (or removes current from) a narrow range of energies in the surface state conduction bands, and thus the local density of states (LDOS) at a fixed energy gives the dominant contribution to the experimentally measured dI/dV [ter84].

The LDOS at $\vec{r}$ is related to the Green's function as the following:

$$\mathcal{L}(\vec{r}, \epsilon) \propto \mathrm{Re}[i\mathcal{G}(\vec{r}, \vec{r}, \epsilon)] \tag{4.1}$$

where $\mathcal{L}$ = LDOS, $\epsilon = E_F + eV - E_0, V$ =bias voltage, $\mathcal{G}(\vec{r}, \vec{r}, \epsilon)$ is the full Green's function with the defects present, and E_0 is the bottom of the band. Let $A_{lm} = t_l i \mathcal{G}^0(\vec{r}_l, \vec{r}_m, \epsilon) \times (1 - \delta_{lm})$, $a_l(\vec{r}) = t_l i \mathcal{G}^0(\vec{r}_l, \vec{r}, \epsilon)$, and) will be an integral equation if the scatterers are not point-like.)

Defining $T_{ij} = t_i \delta_{ij}$, we may write the full scattering T-matrix for the system as $\mathbf{B} = [\mathbf{1} - \mathbf{A}]^{-\mathbf{1}}\mathbf{T}$. Consequently,

$$\begin{aligned} \mathcal{L} &\propto 1 + Re[\mathbf{a_T}[\mathbf{1} - \mathbf{A}]^{-\mathbf{1}}\mathbf{a}] \qquad (4.2) \\ &= 1 + Re[\mathbf{a_T} \mathbf{B} \mathbf{a_T}], \qquad (4.3) \end{aligned}$$

Using scattering theory in 2D, we can write the single scattering T-matrix in terms of the phase shift:

$$\frac{-it_l}{4} = \frac{\alpha_l e^{i\delta_l} - 1}{2} \qquad (4.4)$$

Assume $\epsilon = \hbar^2 k^2 / 2m^*$ is the right dispersion relation, where $m^* = 0.38 m_e$. For the Fe adatoms, $\alpha_l = 0$, which is the maximum attenuation, has yield a very good fit. This would correspond to an absorption of 50%, a transmission of 25%, and a reflection of 25% for a wall with Fe adatoms $9.6\mathring{A}$ apart at Fermi energy. The less than perfect wall built by the Fe adatoms can only keep the electron inside for 2-3 bounces. Therefore there is no way to study the long term evolution of the trajectory, which is essential for chaos. The results for the dI/dV curve of the 60 atoms on a circle are shown on figure 4.1. As I have mentioned, the peak above the Fermi energy is shifted quite a bit from the experimental observation.

4.4 Modified Dispersion Relation

In the calculation by Heller et al[hel94], the dispersion relation has been assumed to be parabolic. However, both band structure theory[euc] and the experiment[cro] have shown anharmonicity in the dispersion curve. Therefore, a modified dispersion relation with a built-in anharmonicity should be used instead of the parabolic one. We know that $E_F = \hbar^2 k^2/2m^* = .45(k/k_F)^2$. We can introduce anharmonicity by putting in a quartic term:

$$\epsilon = \hbar^2 k^2/2m_b + \epsilon_4 (k/k_F)^4 \tag{4.5}$$

where m_b is the effective mass at the bottom of the band, $\epsilon_4 = .45eV - E_F * m^*/m_b$. This ensures that the curve passes through the Fermi energy E_F at the correct wavevector k_F. By fitting with the dI/dV curve, I have found that an effective mass of $m_b = .352m_e$ at the bottom of the band yields a good fit. The results for the 60 Atoms circle are shown on figures 4.2 and 4.3. The fit of the peaks are improved significantly over figure 4.1.

4.5 Acoustics of the Corrals

So far, we have not yet addressed the issue regarding the width of the peaks in the dI/dV curve. The width extracted from the experimental and numerical results are used to infer the lifetime of the electrons in the enclosure. In this section, we are going to use a well known formula in acoustics to calculate the corresponding reverberation time of the circle corral. From that, we can use Heisenberg uncertainty principle to predict the width of the curve.

To find out about the Q of the corral, it is similar to ask the question of the reverberation time of a chamber. So the question is: after a pistol is fired, when does the sound stop? As pointed out by Mortessagne in his thesis [mor], Sabine [sab] had answer this question early this century. With the help of his stop watch and his ears, Sabine found that no audible sound of a pistol shot could be heard after about the same time at all location of the chamber. Further, by using organ pipes, he noticed that the reverberation increased by the same absolute amount when increasing from one pipe to two pipes and from two pipes to four pipes. This implies an exponential decay law of energy:

$$\frac{-dW}{W} = \frac{dt}{\tau} \tag{4.6}$$

$$W = W_0 e^{-t/\tau} \tag{4.7}$$

Furthermore, he assumed that the energy propagates isotropically, and energy is uniformly distributed in the room. In addition, he also hypothesized that energy absorption is continuous. Assuming that every wall has an absorption coefficient of α, the decaying time in 2D is:

$$\tau = \frac{< l >}{c\alpha} \tag{4.8}$$

where $< l >$ is the mean free path length and, c is the speed of the wave in the medium. However, this is not quite correct since the absorption does not happen continuously. As found by Eyring [eyr], it happens at each bounce. At each discrete bounce, the energy is multiplied by a factor of $1 - \alpha$[nor]. The average number of bounces in time t is $n = ct/ < l >$. Therefore,

$$W(t) = W_0(1-\alpha)^{ct/<l>} = W_0 e^{c\ln(1-\alpha)t/<l>} \tag{4.9}$$

In other words,

$$\tau = - < l > /c\ln(1-\alpha) \tag{4.10}$$

Now we need to calculate the mean free path length $< l >$ in 2D. The formula [cla, czu] is:

$$< l >= \frac{\pi A}{P} \tag{4.11}$$

where A is the area and P is the perimeter. For a circle,

$$< l >= \pi R/2 \tag{4.12}$$

At $\epsilon = E_F$, the speed is $c = \hbar k_F/m_e$. Moreover, for the Fe atom wall, we know that $\alpha = 75\%$. By substituting all these numbers into the expression for τ and using the Heisenberg uncertainty principle, the width is

$$\Delta E = \hbar/\tau = 0.03eV \tag{4.13}$$

This agrees very well with the width in the figures.

4.6 Conclusion

By introducing the anharmonicity in the dispersion relation, the shift in the location of the peaks in the dI/dV curve above Fermi energy is fixed. Moreover, by using an acoustic argument, the peak width of the peaks in the dI/dV curve is predicted.

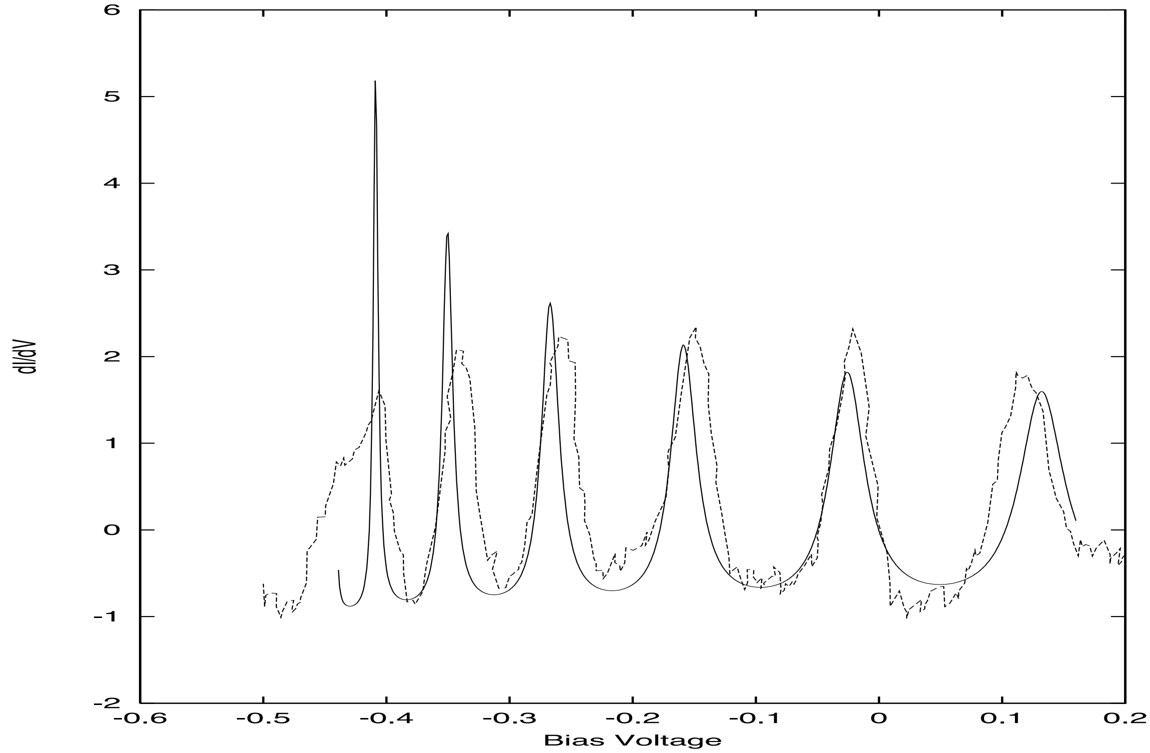

Figure 4.1: The results by Heller et al of dI/dV vs V for the 60 atoms on a circle with radius of $88.67\mathring{A}$ is shown, compared with the experimental value.

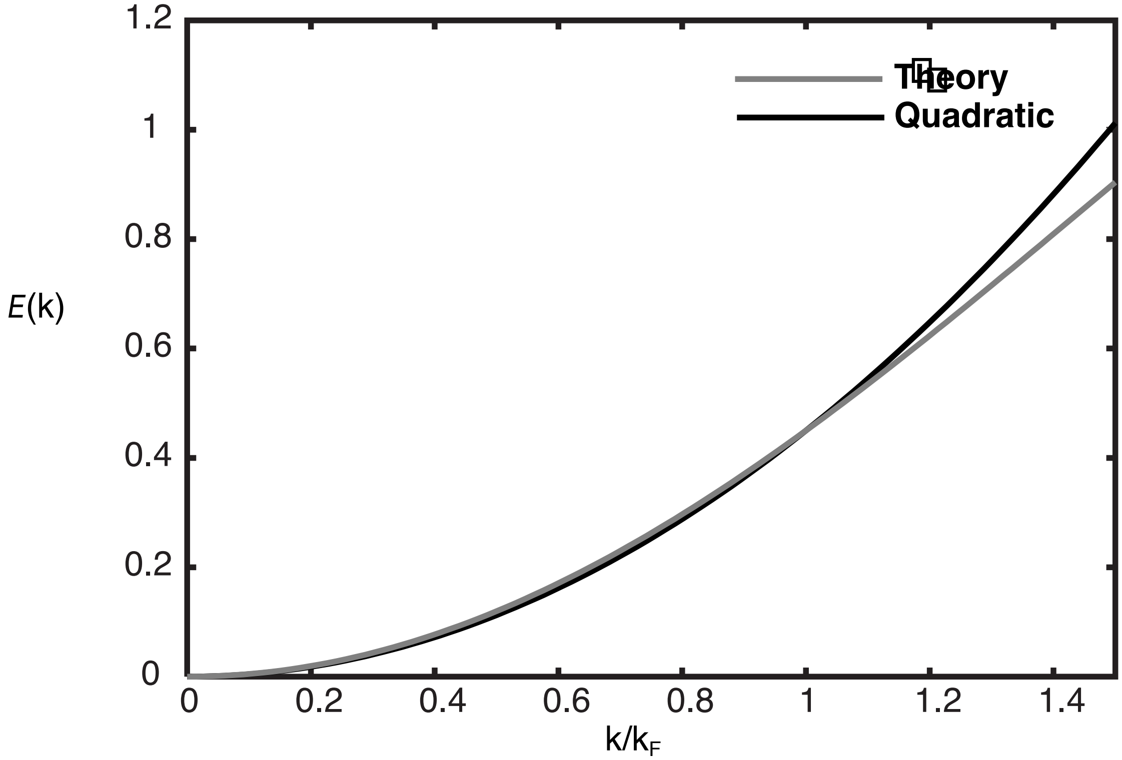

Figure 4.2: Shown is the dispersion relation with a quartic anharmonicity built in. The effective mass at the bottom of the band is $m_b = 0.352 m_e$. The quadratic dispersion relation is plotted as a comparison.

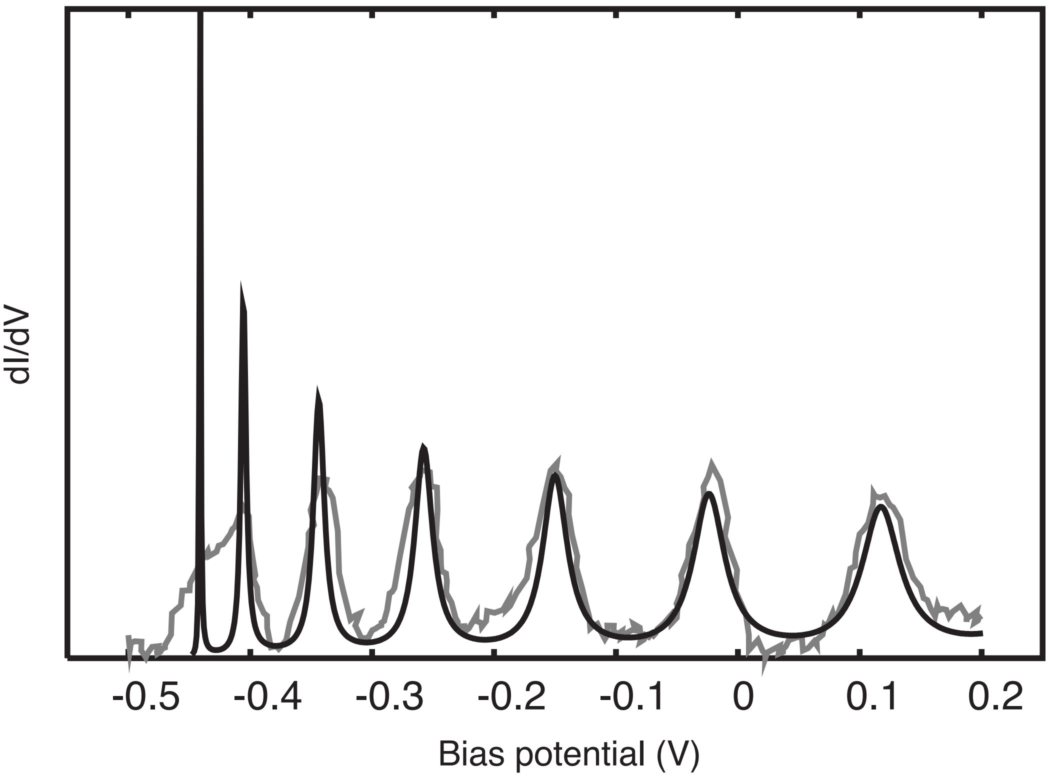

Figure 4.3: The dI/dV vs V is plotted with the modified dispersion relation with a $m_b = 0.352m_e$. The location of the peaks agree with the experimental curve.

Chapter 5

Theory of STM Surface State Electron Scattering off a Step Edge

Abstract

We develop a theory for the scattering of surface electron off a step edge on (111) surface of fcc noble metals. By using multiple scattering theory, the scattering off a step edge can be characterized by a phase shift. This phase shift cannot be determined completely with the STM image near a step edge (by itself). However, by putting several Fe adatoms (with known phase shift) near the step edge, we can extract the information of the step edges phase shift. We suggest this as an experiment to study the scattering properties of the step edge.

5.1 Introduction

The Scanning Tunneling Microscope has probed surface structure essentially atom by atom, imaging the local density of electron states. Experiments[cro93Na, has93, cro93Sc, avo90] have observed standing wave patterns due to scattering off adatoms, defects and step edges on the (111) surface of fcc noble metals, where the surface state electrons form a nearly free two dimensional (2-D) electron gas. In particular, the experiments have imaged the local density of electron states near a step edge. Multiple scattering theory has been used to explain the "Quantum Corrals"(enclosed fence built with adatoms) and the more general scattering off adatoms (s-wave scatterers), which can be an open structure. Although many theories [hel94, chan97] have been proposed for the scattering off s-wave scatterers, little has been done to study the scattering property of a step edge, which by itself gives a "Friedel-like" oscillation in the STM images.

Using the standard STM theory [ter84], the surface local density of states (LDOS) at fixed energy is the dominant contribution to the derivative of the tunneling current I with tip voltage V, dI/dV. Coherent propagation of electron amplitude from tip to the defects, from these to other defects, and back to tip shows that the STM signal is essentially, at each position of the tip, the diagonal element (at that position) of the full energy quantum Green's function for surface state propagation. Therefore, we can use this technique to build a model for scattering off a step edge.

In the most simplified case, electron wave bounces specularly off a step edge and picks up a phase shift (which is generally imaginary due to the coupling to the bulk states). Like the single Fe adatom case[hel94], any information about the attenuation is buried by the geometric factor of the STM tip. For the case with the Fe adatom, the information fo the phase shift can be uncovered by studying the scattering off a number of the Fe adatoms. And the phase shift for the Fe adatom on Cu(111) is known. Using the same trick, the Fe adatom (with its known phase shift) can be used as a "gauge" to find the phase shift of a step edge by imaging the surface with Fe adatoms near the step edge.

5.2 Multiple Scattering Formalism

The quantity measured in the STM experiments we consider here[cro93Na, has93, cro93Sc, avo90] is dI/dV, the change of current I with voltage V. A small change in voltage induces current in (or removes current from) a narrow range of energies in the surface state conduction bands, and thus the local density of states (LDOS) at a fixed energy gives the dominant contribution to the experimentally measured dI/dV [ter84].

The LDOS at $\vec{r}$ is related to the Green's function as the following:

$$\mathcal{L}(\vec{r}, \epsilon) \propto \mathrm{Re}[i\mathcal{G}(\vec{r}, \vec{r}, \epsilon)] \tag{5.1}$$

where $\mathcal{L} = \mathrm{LDOS}$, $\epsilon = E_F + eV - E_0, V =$bias voltage, $\mathcal{G}(\vec{r}, \vec{r}, \epsilon)$ is the full Green's function with the defects present, and E_0 is the bottom of the band. Let $A_{lm} = t_l i\mathcal{G}^0(\vec{r}_l, \vec{r}_m, \epsilon) \times (1 - \delta_{lm})$, $a_l(\vec{r}) = t_l i\mathcal{G}^0(\vec{r}_l, \vec{r}, \epsilon)$, and $a_{T_l}(\vec{r}) = i\mathcal{G}^0(\vec{r}, \vec{r}_l, \epsilon)$. $\mathcal{G}^0$ is the free Green's function, and t_l is scattering T-matrix of the lth scatterer. In 2D, $\mathcal{G}^0(\vec{r}, \vec{r'}, \epsilon) = \frac{-i}{4} H_0^{(1)}(k|\vec{r} - \vec{r'}|)$. The free space Green's function is applicable because there is a nearly free 2D electron gas on the (111) surface of fcc noble metals. Coherent propagation of electron amplitude from the tip to adatoms (defects) and then back to the tip is described by $\mathbf{a} \cdot \mathbf{a_T}$. The amplitude back to the tip after $n+1$ bounces on the adatoms (defects) is $\mathbf{a_T A^n a}$. Therefore, the diagonal element of the full quantum

Green's function, which corresponds to the total amplitude, is:

$$i\mathcal{G} = i\mathcal{G}^0(\vec{r},\vec{r},\epsilon) + \sum_{n=0}^{\infty} \mathbf{a_T}(\vec{r})\mathbf{A^n a}(\vec{r}) \tag{5.2}$$

$$= i\mathcal{G}^0(\vec{r},\vec{r},\epsilon) + \mathbf{a_T}(\vec{r})[\mathbf{1}-\mathbf{A}]^{-1}\mathbf{a}(\vec{r}) \tag{5.3}$$

(Note that equation (5.2) will be an integral equation if the scatterers are not point-like.) Defining $T_{ij} = t_i\delta_{ij}$, we may write the full scattering T-matrix for the system as $\mathbf{B} = [\mathbf{1}-\mathbf{A}]^{-\mathbf{1}}\mathbf{T}$. Consequently,

$$\mathcal{L} \propto 1 + Re[\mathbf{a_T}[\mathbf{1}-\mathbf{A}]^{-\mathbf{1}}\mathbf{a}] \tag{5.4}$$

$$= 1 + Re[\mathbf{a_T B a_T}], \tag{5.5}$$

Using scattering theory in 2D, we can write the single scattering T-matrix in terms of the phase shift:

$$\frac{-it_l}{4} = \frac{\alpha_l e^{i\delta_l} - 1}{2} \tag{5.6}$$

5.3 Scattering off a Step Edge

As we are working in the low energy regime, the wavelength of the electron is much longer than the scale of irregularities of the step edge. Thus the edge can be considered as "smooth" and "straight". Wave bounces specularly off a smooth plane. Moreover, whenever the wave hits the edge, it picks up a phase shift. For simplicity, choose the edge to be at $x = 0$. Let the real part of the phase shift and attenuation by the edge be δ_s and α_s respectively. And the T-matrix for the step edge is $\frac{-it_s}{4} \equiv \beta_s e^{i\gamma_s} = \frac{\alpha_s e^{i\delta_s}-1}{2}$. Then the LDOS near the step edge is:

$$\mathcal{L} \propto 1 + Re[H_0^{(1)}(2kr)\frac{\alpha_s + c_2 e^{i\delta_s} - 1}{2}] \tag{5.7}$$

$$\rightarrow \quad 1 + \beta_s \cos(2kr - \pi/4 + \gamma_s)\sqrt{\frac{1}{\pi kr}} + c_2, \tag{5.8}$$

where c_2 is the current tunneling to the bulk.

Since this is only a proportionality, not an equality, the information about β_s cannot be extracted. Further, the exact location of the step is quite very well-defined compared to the wavelength. Subsequently, γ_s can be determined by locating the trough and the crest of the signal. However, the information about the attenuation is buried by the geometric factor. Therefore, we cannot find δ_s and α_s from the STM image near the step edge alone.

5.4 Scattering off A Step Edge and An Array of Fe Adatoms on Cu(111)

The "Quantum Corral" experiments are done with Fe adatoms on Cu(111). With the multiple adatoms on the surface, the STM image corresponds to the maximum attenuation $\alpha = 0$[hel94]. Therefore, the real part of the phase shift δ is irrelevant. Define $\beta e^{i\gamma} = \frac{\alpha e^{i\delta} - 1}{2}$. And $\beta e^{i\gamma} = .5e^{i\pi}$. In order to gauge β_s, consider a setup with Fe adatoms by the step edge. Information about β_s can be recovered because the amplitude bouncing between defects is affected by the attenuation. The total amplitude reaching the tip consists of two main components. First, like the case without the adatoms, there is the amplitude from the tip bouncing on the edge normally and back to the tip (figure 5.1 (a)). Second, there are amplitudes going from the tip to the ith scatterer, bouncing off any possible path, finally to the jth and back to the tip. Again, since we assume specular reflection, the wave can bounce on the wall before getting to the adatom, and can bounce on the wall before getting back to the tip. The four possible cases are shown on figure 5.1 (b) - (e). Likewise, the amplitudes going from one scatterer to the other can involve bouncing on the wall. By ray-tracing the amplitudes, we can conclude that putting an array of N Fe adatoms by the step edge is equivalent to the problem with N Fe adatoms and N "image" adatoms with phase shift of $\beta\beta_s e^{i(\gamma+\gamma_s)}$ where the "mirror" is along the step edge. This is schematically shown on figure 5.2. Then we can apply multiple scattering theory to this problem. The LDOS will be given by:

$$\mathcal{L} \propto 1 + Re[H_0^{(1)}(2kr)\beta_s e^{i\gamma_s}] + Re[\mathbf{a_T}[\mathbf{1} - \mathbf{A}]^{\mathbf{-1}}\mathbf{a}] \tag{5.9}$$

We can then vary α_s and δ_s, and therefore β_s and γ_s, to fit the experimental data. In particular, the T-matrix will be different for different step edges. Further, "stepping-up" and "stepping-down" the edge have phase shift and attenuation. "Stepping-up" has a strong coupling to the bulk. Consequently, it has a very low α_s.

5.5 Discussion of Numerical Results

As mentioned previously, the information about the attenuation and the phase shift by the step edge can be extracted by putting Fe adatoms near the edge. And this is because multiple scattering is sensitive to the attenuation as well as the phase shift of the defects. But how "sensitive" is it? Intuitively, the more adatoms there are, the more sensitive the LDOS rasterscan is to the attenuation and the phase shift. Numerically, we find that it is difficult to distinguish the patterns with few Fe adatoms for various step edge phase shifts and attenuations. The LDOS with 2 Fe adatoms near the edge is shown on figure 5.3 with a phase shift of $\delta_s = 0$ and an attenuation of $\alpha_s = 0.4$ for the step edge. The two adatoms are located symmetrically about $y = 0$, two wavelengths away from the edge and two wavelengths apart. However, the pattern with just two scatterers is extremely insensitive to variation of the phase shift. We found that the pattern with phase shift of $\delta_s = .05\pi$ appears no different from figure 5.3. Therefore, we need to put more Fe adatoms on the surface to see significant difference between the patterns. In particular, we looked at the pattern with 24 Fe atoms evenly spaced along a semi-circle with a radius of four times the wavelength and centered at twice the wavelength away from the edge. This setup is reasonable because the "Quantum Corral" experiment done on Cu(111) surface states has a wavelength of $40\mathring{A}$ and the spacing between the adatoms is around $9.6\mathring{A}$. The patterns for various phase shifts and attenuations are shown on figure 5.4. Distinctive features can be recognized from the patterns up to an error of ± 0.1 for attenuation α_s and $\pm 0.05\pi$ (around 10 degrees) for phase shift δ_s.

5.6 Conclusion

In conclusion, putting Fe adatoms, whose phase shift is well-known, next to the step edge on Cu(111) enables us to extract the information on the phase shift of the step edge. STM experiment with this setup would be a possible tool to investigate the scattering property of the surface.

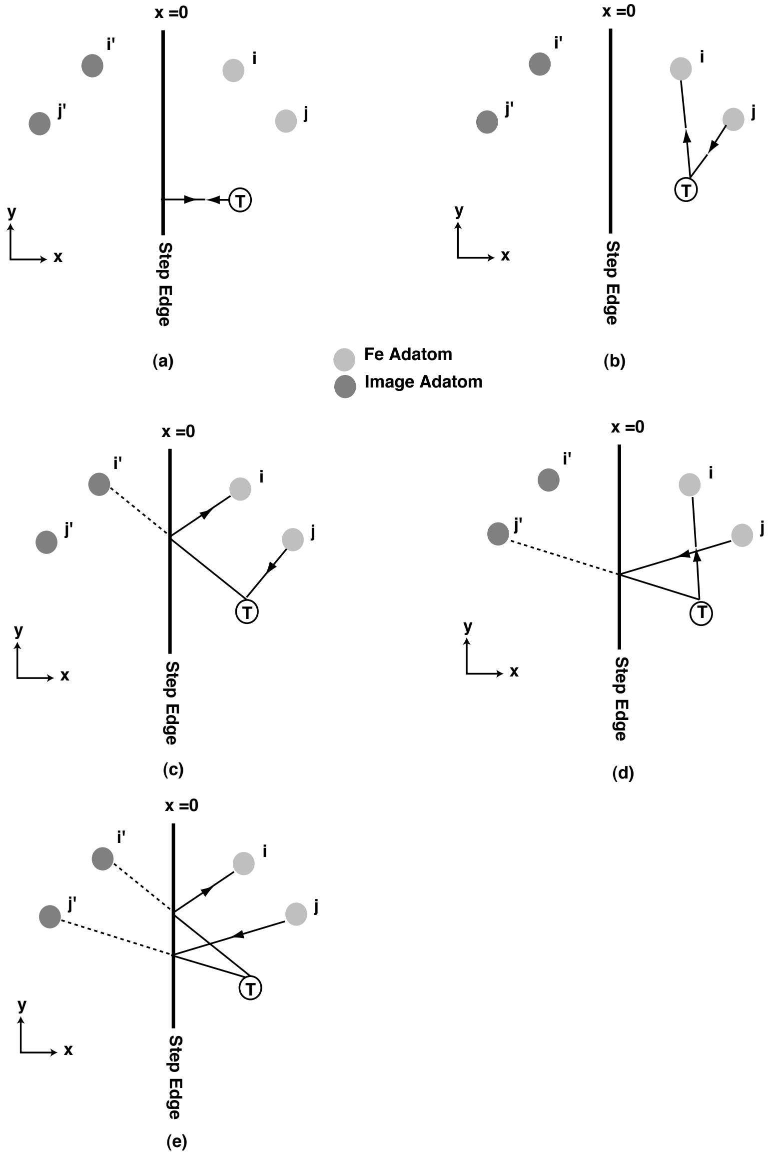

Figure 5.1: Shown are the components of the total amplitude. (a) This component goes from the tip and reflects normally off the edge back to the tip. (b) This amplitude goes from the tip to the ith scatterer and bounces off all possible paths and finally to the jth scatterer and then back to the tip. (c) Same as (b), except that the wave bounces off the edge before hitting the ith scatterer for the first time. This is equivalent to hitting the image scatterer, $i'th$. (d) Same as (b), except that the wave bounces off the edge before finally getting back to the tip from the jth scatterer. This is equivalent to the amplitude coming from the image scatterer, $j'th$. (e) The amplitude bounces off the edge before hitting the ith scatterer for the first time, and after coming off the jth scatterer for the final time. Again, this is equivalent to scattering from the image scatterers i' and j'.

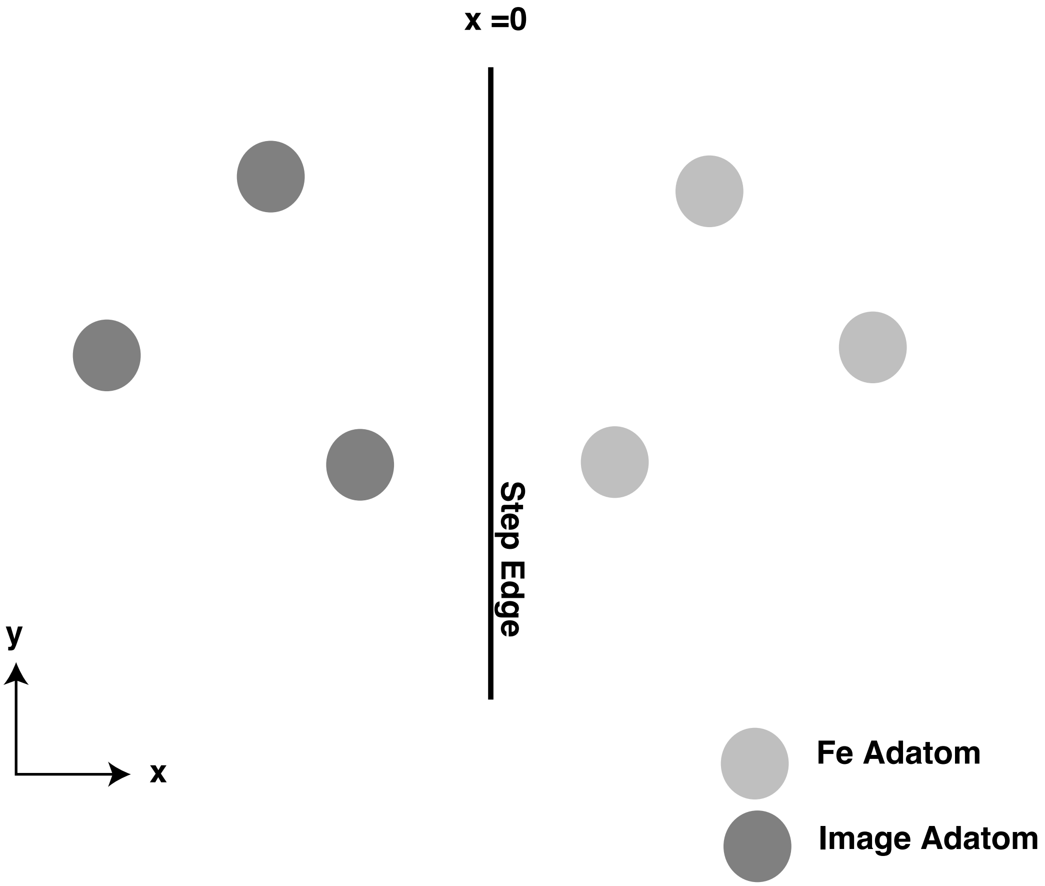

Figure 5.2: The scattering off N adatoms with T-matrix of $\beta e^{i\gamma}$ near a step edge can be reduced to the scattering problem with N adatoms and N image adatoms with a T-matrix of $\beta\beta_s e^{i(\gamma+\gamma_s)}$.

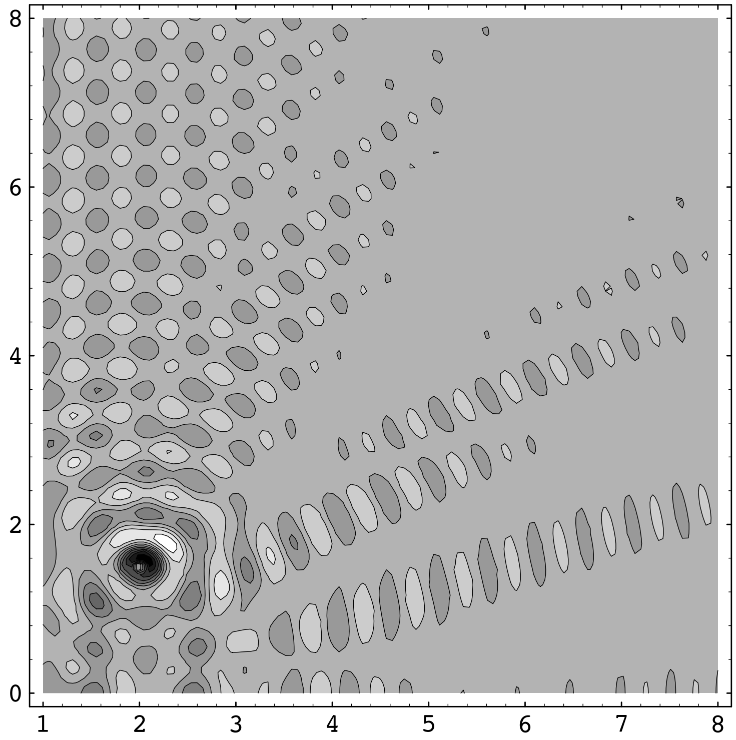

Figure 5.3: Contour plot of LDOS for 2 Fe adatoms, at (2,2) and (2,-2), near the step edge (at $x = 0$) is shown. The edge has a phase shift of $\delta_s = 0$ and an attenuation of $\alpha_s = .4$. This pattern is insensitive to the variation of real part of the phase shift. (The scale is measured in terms of the wavelength.)

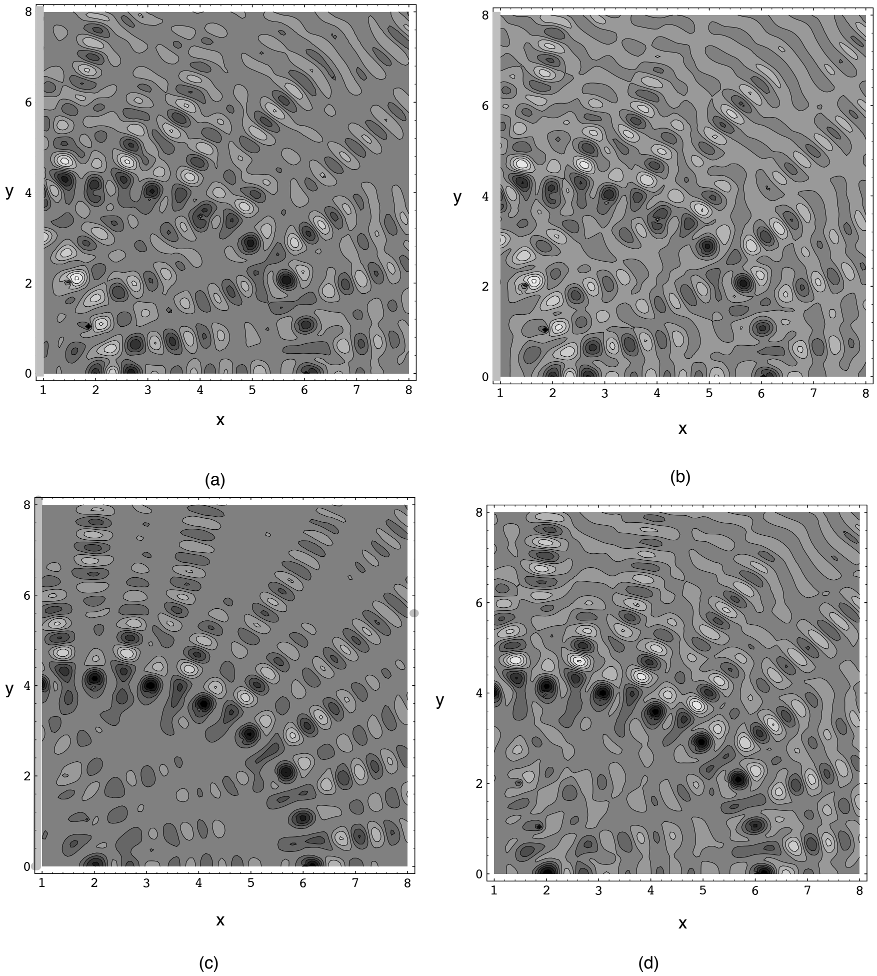

(a)

(b)

(c)

(d)

Figure 5.4: Contour plot of LDOS for 24 Fe adatoms, located uniformly on a semicircle of radius 4 wavelengths and centered at (2,0) near the step edge (at $x = 0$), is shown. (The scale is measured in terms of the wavelength.) The plots corresponds to the following attenuation and phase shift for the edge: (a) $\alpha_s = .4$, $\delta_s = \pi$, (b)$\alpha_s = .4$, $\delta_s = .95\pi$, (c) $\alpha_s = .4$, $\delta_s = 0$, $\alpha_s = .4$, $\delta_s = \pi/4$. By inspection, there are distinctive features for each of the plot.

Chapter 6

Two-Tip Results From One-Tip Data and its Variations

6.1 Introduction

In this chapter, the results of getting the transport properties from the local density of state will be presented[chan97]. From the local density of states at various positions, the total scattering T-matrix as well as the full Green's function can be determined.

Another interesting question raised in this context is the relation between the Green's functions of similar but not identical configurations of localized scatterers with only one angular momentum channel. We show that the Green's function of a configuration with one scatterer missing can be related to that of the original configuration through a very simple expression. The Green's function of a configuration with a added scatterer of known properties can be related to that of the original as well.

6.2 STM Surface State Electron Scattering:Two-Tip Results from One-Tip Data

Abstract

The STM experiments have opened up a new class of scattering inversion problems, where the scatterers are fixed and the boundary condition corresponds to a movable point source. Using a least square method, we can obtain the scattering T-matrix for an assembly of atoms (s-wave point scatterers) on a surface; and thus the off-diagonal elements of the Green's function just from the knowledge of the one-tip data. Therefore, transport property measurements such as that suggested by Niu et al., which are needed when other kind of defects are present, can be predicted solely from the one-tip data.

6.2.1 Introduction

The one-tip scanning tunneling microscope (STM) has permitted study of surface electron structure in great detail, by imaging the local density of electron states. Recent experiments[cro93Na, has93, cro93Sc, avo90] have observed standing wave patterns due to scattering off adatoms, defects and step edges on the (111) surface of fcc noble metals, where the surface state electrons form a nearly free two dimensional (2-D) electron gas. Initially, the particle in a box theory has been used to explain the pattern in the hand made "quantum corrals" (area enclosed by adatom fence). It was later shown that s-wave multiple scattering theory with complex phase shifts can accurately account for the interference patterns[hel94] of both the corrals and open systems.

After knowing the local properties of the surface, it is natural to study the transport properties, which requires the knowledge of the off-diagonal elements of the Green's function. This points to a two-tip STM experiment such as the one suggested by Niu et al. [niu95]. Their motivation was founded in the intuitively reasonable idea that a two tip experiment would contain much more information than the one tip data. However, the two-tip STM is extremely difficult to achieve technically.

Surprisingly, for surfaces with adatoms and point defects, the off-diagonal Green's function can actually be obtained from the single tip STM data at various points on the surface by using a least square inversion procedure. Adatoms and point defects can reasonably be modeled as point s-wave scatterers. (Step edges and other defects still remain unexplored both experimentally and theoretically and we do not know presently whether these can be included in the inversion procedure.) Although inverse scattering has been an old and often difficult problem, the s-wave multiple scattering problem turns out to be very tractable. Contrary to the assumption of Niu et al.[niu95], the two tip measurement need not contain more information than the one tip data, in the sense that two tip transport properties can be predicted by the one-tip STM data.

6.2.2 Review of the Multiple Scattering Theory

The quantity measured in the STM experiments we consider here[cro93Na, has93, cro93Sc, avo90] is dI/dV, the change of current I with voltage V. A small change in voltage induces current in (or removes current from) a narrow range of energies in the surface state conduction bands, and thus the local density of states (LDOS) at a fixed energy gives the dominant contribution to the experimentally measured dI/dV [ter84].

The LDOS at $\vec{r}$ is related to the Green's function as the following:

$$\mathcal{L}(\vec{r}, \epsilon) \propto \mathrm{Re}[i\mathcal{G}(\vec{r}, \vec{r}, \epsilon)] \tag{6.1}$$

where $\mathcal{L} =$ LDOS, $\epsilon = E_F + eV - E_0, V =$bias voltage, $\mathcal{G}(\vec{r}, \vec{r}, \epsilon)$ is the full Green's function with the defects present, and E_0 is the bottom of the band. Let $A_{ij} = t_i i\mathcal{G}^0(\vec{r}_i, \vec{r}_j, \epsilon) \times (1 - \delta_{ij})$, $a_i(\vec{r}) = t_i i\mathcal{G}^0(\vec{r}_i, \vec{r}, \epsilon)$, and $a_{T_i}(\vec{r}) = i\mathcal{G}^0(\vec{r}, \vec{r}_i, \epsilon)$. $\mathcal{G}^0$ is the free Green's function, and t_i is scattering T-matrix of the ith scatterer. Coherent propagation of electron amplitude from the tip to adatoms (defects) and then back to the tip is described by $\mathbf{a} \cdot \mathbf{a_T}$. The amplitude back to the tip after $n + 1$ bounces on the adatoms (defects) is $\mathbf{a_T A^n a}$. Therefore, the diagonal element of the full quantum Green's function, which corresponds to the total amplitude, is:

$$\begin{aligned} i\mathcal{G} &= i\mathcal{G}^0(\vec{r}, \vec{r}, \epsilon) + \sum_{n=0}^{\infty} \mathbf{a_T}(\vec{r}) \mathbf{A^n} \mathbf{a}(\vec{r}) & (6.2) \\ &= i\mathcal{G}^0(\vec{r}, \vec{r}, \epsilon) + \mathbf{a_T}(\vec{r}) [\mathbf{1} - \mathbf{A}]^{-1} \mathbf{a}(\vec{r}) & (6.3) \end{aligned}$$

(Note that equation (6.2) will be an integral equation if the scatterers are not point-like.) Defining $T_{ij} = t_i \delta_{ij}$, we may write the full scattering T-matrix for the system as $B = [1 - A]^{-1}T$. Consequently,

$$\begin{aligned} \mathcal{L} &\propto 1 + Re[\mathbf{a_T}[\mathbf{1} - \mathbf{A}]^{\mathbf{-1}}\mathbf{a}] \quad (6.4) \\ &= 1 + Re[\mathbf{a_T}\mathbf{B}\mathbf{a_T}], \quad (6.5) \end{aligned}$$

The crucial point is that if we know $\mathbf{B}$, we know the whole *off-diagonal* Green's function as

$$\mathcal{G}(\vec{r'}, \vec{r}, \epsilon) = \mathcal{G}^0(\vec{r'}, \vec{r}, \epsilon) - i\mathbf{a_T}(\vec{r'})\mathbf{B}\mathbf{a}(\vec{r}) \quad (6.6)$$

6.2.3 Two tip results from one tip data

The experiments measure dI/dV at various positions on the surface, which is, as mentioned above, related to the electron LDOS[ter84]. Let L be the number of positions at which the one tip measurements have been taken, and N be the number of scatterers on the surface of Cu(111). We then have L linear equations of the following form:

$$c_1\mathcal{L}(\vec{r_l}, \epsilon) + c_2' \equiv c_1\mathrm{Re}[1 + \mathbf{a_T}(l)\mathbf{B}\mathbf{a_T}(l)] + c_2 = b_l \quad (6.7)$$

where c_1, c_2 are real constants, $c_2 = c_1 + c_2'$ and $l = 1, \cdots, L$; b_l is the experimental data at position $\vec{r_l}$, and $a_T(l) = a_T(\vec{r_l})$. c_1 depends on the size and geometry of the STM tip, and c_2' corresponds to current flowing directly to the bulk states. Since all the scatterers are s-wave, t_i has no directional dependence. Subsequently, B_{ij} will be independent of the tip position. Then equation (6.7) can be rewritten as linear equations in the unknowns, c_1B_{ij} and c_2:

$$c_1(\mathrm{Re}[a_{T_i}(l)a_{T_j}(l)]\mathrm{Re}[B_{ij}] - \mathrm{Im}[a_{T_i}(l)a_{T_j}(l)]\mathrm{Im}[B_{ij}]) + c_2 = b_l \quad (6.8)$$

There are at most $2N^2 + 1$ unknowns, $c_1\mathrm{Re}[B_{ij}]$, $c_1\mathrm{Im}[B_{ij}]$ and c_2 (exactly $2N^2 + 1$ if all c_1B_{ij}, are independent), and L linear equations.

When all of the B_{ij} are independent, we can rewrite equation (6.8) by mapping all the unknowns onto a $2N^2 + 1$ column vector, $\mathbf{x}$, and the coefficients for the L equations onto a $L \times (2N^2 + 1)$ matrix, $\mathbf{\Omega}$, as:

$$\Omega_{ml} x_m = b_l \tag{6.9}$$

Then if $L \geq 2N^2 + 1$ and if the L equations are linearly independent, we may use singular value decomposition to solve for a least square error solution for the real and imaginary parts of all $c_1 B_{ij}$ and c_2.

$$x = (\mathbf{\Omega^T \Omega})^{-1} \mathbf{\Omega}^T b \tag{6.10}$$

This completes the determination of x and thus B_{ij}, from which we get the off diagonal Green's function *via* Eq. 6.6.

Symmetry considerations

In cases where there is a symmetry in the system, some elements of the B_{ij} are related. For instance, for a system with time-reversal symmetry, $B_{ij} = B_{ji}$. Or for a system with geometrical symmetry such as the 60 atoms in a circle, $B_{ij} = B_{\sigma(i)\sigma(j)}$, where σ is an element of the symmetry group. In those cases, the coefficients of equation (6.9) have to be grouped accordingly before applying the singular value decomposition method.

Determination of the phase shift for s-wave scatterers

We now can go beyond the Green's function result and determine the scattering properties of the individual s-wave scatterers present, including the multiplicative constant c_1. By the definition of $\mathbf{B}$, we have:

$$\mathbf{A} = 1 - \mathbf{T}(c_1 \mathbf{B})^{-1} c_1 \tag{6.11}$$

Since $A_{ij} = t_i G_{ij}$, where $G_{ii} = 0$ and $G_{ij} \equiv \mathcal{G}^0(\vec{r}_i, \vec{r}_j, \epsilon)$ is the free Green's function in two dimensions connecting scatterer positions i and j,

$$t_i G_{ij} = \delta_{ij} - t_i (c_1 B)^{-1}_{ij} c_1 \tag{6.12}$$

We can use singular value decomposition [pre92] again for the atoms of the same species S for we have $|S| \times N$ linear equations in t_s in the form of equation (6.12), where $|S|$ is the number of atoms of species S.

We find

$$t_s = \frac{\sum_{i \in S} c_1 (c_1 B_{ii})^{-1}}{\sum_{i \in S} \sum_{j=1}^{N} (G_{ij} + c_1 (c_1 B_{ij})^{-1})^2} \tag{6.13}$$

In fact, the multiplicative factor c_1 can be determined from the fit of the theory to experimental data of the Fe adatom on Cu(111) (quantum corrals) [hel94]. This factor should only depend on the size and geometry of the sample and the tip, i.e. c_1 is independent of the nature of the s-wave scatterers. In other words, the (possibly complex) phase shift of any s-wave scatterer can be determined completely once we have determined the optimal c_1. To find c_1, consider the least square error:

$$\text{Error} = \sum_{all\ \ \vec{r}_i} [c_1 \mathcal{L}_{theory}(\vec{r}_i, \epsilon, \mathbf{T}(c_1)) - c_1 \mathcal{L}_{expt}(\vec{r}_i, \epsilon)]^2 \tag{6.14}$$

After calculating the minimum of Error w.r.t. c_1, we would have the least square fit of t_s, c_1 and also the exact Green's function.

The inversion method can suffer from numerical instability when the matrix Ω is nearly singular, even after all the symmetries have been accounted for. The first line of defense is the placement of the experimental data points, as this can strongly affect numerical stability. Inversion can also be achieved when Ω is nearly singular by minimizing equation (6.14) w.r.t. c_1 as well as the t_s of different species. We have found that this only works well when the number of species of scatterer is less than 10.

We have shown the whole Green's function (up to a multiplicative constant) can be determined solely from its diagonal elements as

$$c_1 \mathcal{G}(\vec{r}, \vec{r'}, E) = c_1 \mathcal{G}^0(\vec{r}, \vec{r'}, E) - i\mathbf{a_T}(\vec{r}) c_1 \mathbf{B} \mathbf{a_T}(\vec{r'}), \tag{6.15}$$

demonstrating the results of the one tip STM experiments can predict the results of the hypothetical two tip or "conductance" experiment. In figure 6.1, the results of the inversion are compared to the exact Green's function. The inversion results with a noisy data of 10% error agrees reasonably well with the exact results. In fact, the inversion with clean data yields agreement within line width.

6.2.4 Two Tip Experiment

There are several "two tip" measurements that one can imagine. For example, one could have a single lead forking into two tips, which might be coherent with one another. Niu et al.[niu95] have made the more natural suggestion of a "two lead" two-tip STM experiment, which measures the transconductance. The current from tip one to the surface I_1 and the current from the surface to tip two I_2 are measured at bias voltage of V_1 and V_2. The one-tip differential conductance is, $i = 1, 2$:

$$\frac{dI_i}{dV_i} = \frac{2\pi e^2}{\hbar} \frac{\Gamma_i}{\pi} Re[\mathcal{G}(\vec{r_i}, \vec{r_i}, \epsilon)] \tag{6.16}$$

where $\frac{2\pi e^2}{\hbar}\frac{\Gamma_i}{\pi} = c_1$ for tip i. The transconductance corresponds to the transition rate from tip 1 to the surface and then to tip 2, and is[niu95]:

$$\sigma_{12} = \frac{\partial I_2}{\partial V_1} = \Gamma_1 \Gamma_2 \frac{2\pi e^2}{\hbar} |\mathcal{G}(\vec{r}_1, \vec{r}_2, \epsilon)|^2 \tag{6.17}$$

where $\epsilon = E_F + eV_1 - E_0$, E_0 is the bottom of the surface band. Since we can find $\Gamma_i \mathcal{G}(\vec{r}_1 \vec{r}_2, \epsilon)$ for each tip from the one-tip data, the *transconductance can also be determined from the one tip data.*

6.2.5 Conclusion of Section

In conclusion, the one-tip STM experiments yield more than just the local properties of the surface. Transport properties including the formidable two-tip experiment, as well as the scattering properties of individual scatterers can be inferred from the STM images. Nevertheless, the two-tip data may still be useful if other than point defects are present.

Acknowledgments

We acknowledge helpful discussions with M. Crommie and D. Eigler. This research was supported by the National Science Foundation under grant number CHE-9014555.

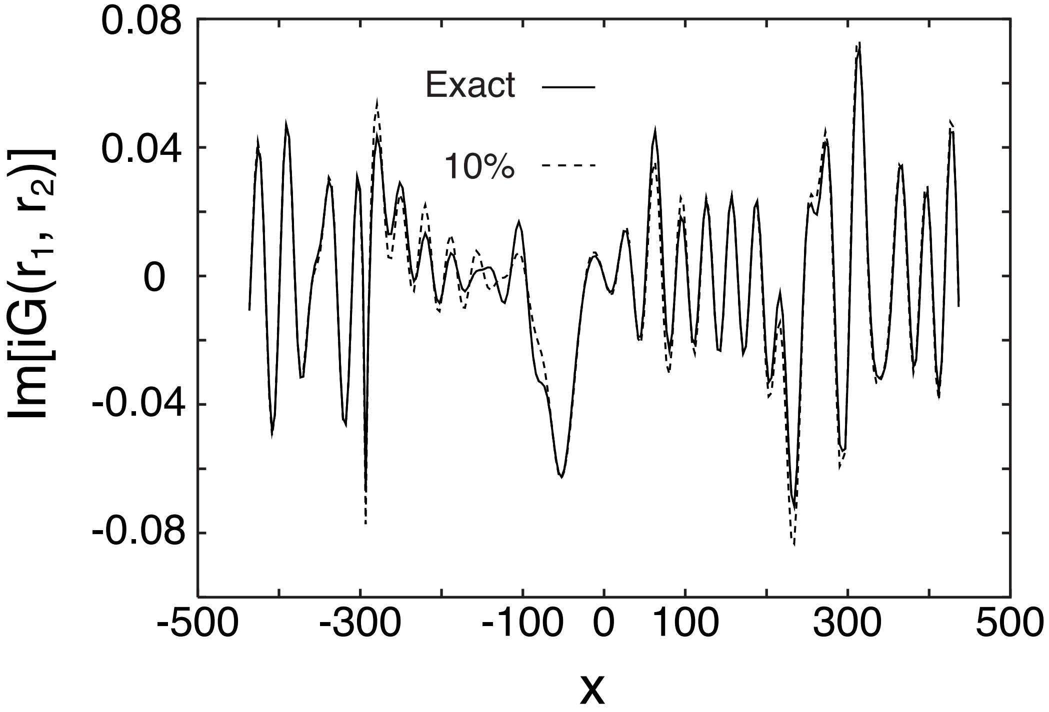

Figure 6.1: $\mathrm{Im}[i\mathcal{G}(\vec{r}_1, \vec{r}_2, \epsilon)]$ is plotted against x, where $\vec{r}_1 = (x, 0)$ and $\vec{r}_2 = (165, 165)$ (in Å). The energy is at $\epsilon = .45eV$. 60 Fe adatoms are located in a circle of radius $292.84\mathring{A}$ centered at $(0., 0.)$. The exact data is compared to the inversion results with noisy data with a Gaussian error of 10%. In fact, the inversion data without noise agrees with the exact one within line width.

6.3 Relating Green's functions of similar configurations of scatterers

Now that we can find the whole Green's function, it would be interesting if we can relate Green's function of a given configuration to a Green's function of a similar configuration in the multiple scattering regime, i.e. amplitudes of all orders are included. The first case to consider will be the relation between the Green's function of a given configuration to that with one scatterer removed.

6.3.1 Missing Scatterer

In the original configuration of scatterers, there are N scatterers on the surface. The one tip experiment then determines the B_{ij} completely, as shown in the previous section. Now we remove the s^{th} scatterer from the configuration, and the new Green's function for the $N-1$ scatterer corresponds to B'_{ij}. In fact, B_{ij} and B'_{ij} can be related through the following simple expression:

$$B'_{ij} = B_{ij} - B_{is}B_{sj}/B_{ss} \tag{6.18}$$

where $i, j = 1, \cdots, N$, and s is the label of the scatterer removed.

This claim can be proved in two different ways. The first one is a straightforward algebraic manipulation from the definition of **A** and **B** and the second one is by a counting argument.

Proof by algebraic manipulation

By the definitions of B_{ij} and B'_{ij}, we have:

$$T(1-A)B = I \qquad\qquad \delta_{ij} = T_i(\vec{r})B_{ij} - T_i(\vec{r})\sum_{\alpha} A_{i\alpha}B_{\alpha j} \tag{6.19}$$

$$T(1-A')B'=I \qquad\qquad \delta_{ij}=T_i(\vec{r})B'_{ij}-T_i(\vec{r})\sum_{\alpha\neq s}A'_{i\alpha}B'_{\alpha j} \tag{6.20}$$

where $A'_{ij}=A_{ij}$ for both $i,j\neq s$,$A'_{ij}=0$ for either $i,j=s$

Then

$$\begin{aligned}
(1-A')B^* &= \sum_{\alpha\neq s}(\delta_{i\alpha}-A'_{i\alpha})(B_{\alpha j}-B_{\alpha s}B_{sj}/B_{ss}) && (6.21)\\
&= \sum_{\alpha\neq s}(\delta_{i\alpha}-A_{i\alpha})B_{\alpha j}-\sum_{\alpha\neq s}(\delta_{i\alpha}-A_{i\alpha})B_{\alpha s}B_{sj}/B_{ss} && (6.22)\\
&= \sum_{\alpha\neq s}(\delta_{i\alpha}-A_{i\alpha})B_{\alpha j}-A_{is}B_{ss}B_{sj}/B_{ss} && (6.23)\\
&= \delta_{ij} && (6.24)
\end{aligned}$$

This proves the claim 6.18.

Proof by counting

Counting is a more intuitive way of verifying the claim, and it will be prove to be useful in section 6.3.2. Define C_{ss} to be the amplitude originating from s^{th} site and arriving back at s^{th} without having visited it in the interim.

$$C_{ss}=\sum_{l\neq s}\sum_{m\neq s}A_{rl}\frac{B'_{lm}}{T_m(\vec{r})}A_{ms} \tag{6.25}$$

Therefore, B_{ss} is just the sum of all amplitudes over all number of stopovers at the s^{th} scatterer:

$$B_{ss}=\frac{1}{1-C_{ss}}T_s(\vec{r}) \tag{6.26}$$

Similarly,

$$\begin{aligned}
B_{is} &= \sum_{l\neq s}\frac{B'_{il}}{T_l(\vec{r})}A_{ls}B_{ss} && (6.27)\\
B_{sj} &= \sum_{m\neq s}\frac{B_{ss}}{T_s(\vec{r})}A_{sm}B'_{mj} && (6.28)
\end{aligned}$$

Hence,

$$\begin{aligned}
B_{ij} &= B'_{ij}+\sum_{lm}\frac{B'_{il}}{T_l(\vec{r})}A_{ls}\frac{B_{ss}}{T_s(\vec{r})}A_{sm}B'_{mj} && (6.29)\\
&= B'_{ij}+\frac{B_{is}B_{sj}}{B_{ss}} && (6.30)
\end{aligned}$$

This again proves the claim (6.18). Unlike the singular decomposition method that only works for the s-wave case, this claim is applicable to localized scatterers with only one angular momentum channel. Moreover, the factorization of amplitudes into parts with the s^{th} scatterer and without is analogous to the Feenberg's perturbation theory for self-avoiding random walk[feen48]. Therefore, equation (6.18) could have been proved with diagrammatic techniques.

6.3.2 Added scatterer

Now that we have a formula linking the Green's function of N scatterers to N-1 scatterers, we can use that formula to go from N to N+1.

Given a configuration, add a scatterer of known **T** matrix to it. **B** is known for the configuration with N scatterers. We would like to find the Green's function $\mathbf{B_{new}}$ for the N+1 scatterers, $s = N + 1$. As in the previous section,

$$A_{new_{ij}} = A_{ij} \tag{6.31}$$

$$A_{new_{is}} = T_i \mathcal{G}^0_{is} \tag{6.32}$$

$$A_{new_{si}} = T_s \mathcal{G}^0_{si} \tag{6.33}$$

Define $C_{ss} = \sum_{i=1}^{N} \sum_{j=1}^{N} A_{new_{si}} \frac{B_{ij}}{T_j(\vec{r})} A_{new_{js}}$ just like section 6.3.1. Then using the previous results in section 6.3.1:

$$B_{new_{ss}} = \frac{1}{1 - C_{ss}} T_s(\vec{r}) \tag{6.34}$$

$$B_{new_{is}} = \sum_{j=1}^{N} \frac{B_{ij}}{T_j(\vec{r})} A_{new_{js}} \frac{1}{1 - C_{ss}} T_s(\vec{r}) \tag{6.35}$$

$$B_{new_{si}} = \sum_{j=1}^{N} B_{ji} A_{new_{sj}} \frac{1}{1 - C_{ss}} \tag{6.36}$$

$$= \frac{T_s}{T_i} B_{new_{is}} \tag{6.37}$$

For $i, j \neq s$, using equation (6.18),

$$B_{new_{ij}} = B_{ij} + \frac{B_{new_{is}} B_{new_{sj}}}{B_{new_{ss}}} \tag{6.38}$$

Combining the knowledge in section 6.3.1 and section 6.3.2, once one knows the Green's function of a given configuration. Then one can predict the Green's function when we add, remove scatterers or even move scatterers around.

6.3.3 Generalization of the Missing Scatterer Formula

In this section, we are going to generalize the missing scatterer formula to removing a group of scatterers at one time. We can start by studying the problem of superimposing two arrays of scatterers, whose Green's functions are known respectively.

Superposition of Two Arrays of Scatterers

Suppose we initially have two isolate arrays of s-wave scatterers with N and M scatterers whose Green's functions correspond to $\mathbf{B^1}$ in the sense of equation (2.93), an $N \times N$ matrix, and $\mathbf{B^2}$, an $M \times M$ matrix, respectively. When we bring them together, the resulting Green's function corresponds to a new $\mathbf{B}$, which depends on $\mathbf{B^1}$,$\mathbf{B^2}$, as well as $\mathbf{G}$, the propagator between the scatterers of the two groups. Define an $(N+M) \times (N+M)$ matrix

$$\tilde{\mathbf{B}} = \begin{pmatrix} \mathbf{B^1} & \mathbf{0} \\ \mathbf{0} & \mathbf{B^2} \end{pmatrix} \tag{6.39}$$

This is the scattering matrix that includes scattering within the respective group only. To cross to another group, we have to consider the "cross-group" propagator:

$$\tilde{\mathbf{G}} = \begin{pmatrix} \mathbf{0} & \mathbf{G^{12}} \\ \mathbf{G^{21}} & \mathbf{0} \end{pmatrix} \tag{6.40}$$

Therefore, $\tilde{\mathbf{G}}_{ij}$ gives the propagator from i to j where i, j belong to different groups. With $\tilde{B}$ and $\tilde{G}$, we can build the total amplitude of scattering. Define

$$\begin{aligned} \tilde{\mathbf{C}} &\equiv \tilde{\mathbf{B}}\tilde{\mathbf{G}}\tilde{\mathbf{B}}\tilde{\mathbf{G}} && (6.41) \\ &= \begin{pmatrix} \mathbf{B^1G^{12}B^2G^{21}} & \mathbf{0} \\ \mathbf{0} & \mathbf{B^2G^{21}B^1G^{12}} \end{pmatrix} && (6.42) \end{aligned}$$

$\tilde{\mathbf{C}}$ is the amplitude of scattering within one group to infinite order, crossing to the second group and scattering around to infinite order , and coming back to the first group. Therefore, the total amplitude that originates from and ends up at same group is:

$$(1 - \tilde{\mathbf{C}})^{-1}\tilde{\mathbf{B}} \tag{6.43}$$

Likewise, the total amplitude that originates from one group and ends up at a different group is:

$$(\mathbf{I} - \tilde{\mathbf{C}})^{-1}\tilde{\mathbf{B}}\tilde{\mathbf{G}}\tilde{\mathbf{B}} \tag{6.44}$$

In other words, the total Green's function corresponds to:

$$\begin{aligned} \mathbf{B} &= (\mathbf{I} - \tilde{\mathbf{C}})^{-1}(\tilde{\mathbf{B}}\tilde{\mathbf{G}} + \mathbf{I})\tilde{\mathbf{B}} && (6.45) \\ &= \begin{pmatrix} (\mathbf{I} - \mathbf{B^1G^{12}B^2G^{21}})^{-1} & \mathbf{0} \\ \mathbf{0} & (\mathbf{I} - \mathbf{B^2G^{21}B^1G^{12}})^{-1} \end{pmatrix} \times \\ &\quad \begin{pmatrix} \mathbf{B^1} & \mathbf{B^1G^{12}B^2} \\ \mathbf{B^2G^{21}B^1} & \mathbf{B^2} \end{pmatrix} && (6.46) \\ &= \begin{pmatrix} (\mathbf{I} - \mathbf{B^1G^{12}B^2G^{21}})^{-1}\mathbf{B^1} & (\mathbf{I} - \mathbf{B^1G^{12}B^2G^{21}})^{-1}\mathbf{B^1G^{12}B^2} \\ (\mathbf{I} - \mathbf{B^2G^{21}B^1G^{12}})^{-1}\mathbf{B^2G^{21}B^1} & (\mathbf{I} - \mathbf{B^2G^{21}B^1G^{12}})^{-1}\mathbf{B^2} \end{pmatrix} && (6.47) \end{aligned}$$

This completes the formula for superimposing two arrays of s-wave scatterers.

Formula for Removing a group of s-wave Scatterers

Let us look at the situation when we have $N+M$ scatterers initially. And I would like to remove M s-wave scatterers at the same time. Rearrange the $\mathbf{B}$ such that those scatterers correspond to $i = N+1, \cdots, N+M$. Consider $\mathbf{B}$ as four submatrices:

$$\mathbf{B} = \begin{pmatrix} \mathbf{B^{11}} & \mathbf{B^{12}} \\ \mathbf{B^{21}} & \mathbf{B^{22}} \end{pmatrix} \tag{6.48}$$

where $\mathbf{B^{11}}$ is an $N \times N$ matrix, $\mathbf{B^{22}}$ is an $M \times M$ matrix, $\mathbf{B^{12}}$ is an $N \times M$ matrix, and $\mathbf{B^{21}}$ is an $M \times N$ matrix. Using equation (6.47), for $i, j = 1, \cdots, N$,

$$B_{ij} = B^{11}_{ij} = [(I - B^1 G^{12} B^2 G^{21})^{-1} B^1]_{ij} \tag{6.49}$$

Therefore,

$$B^1_{ij} = B_{ij} - [(I - B^1 G^{12} B^2 G^{21})^{-1} B^1 G^{12} B^2 G^{21} B^1]_{ij} \tag{6.50}$$

The second term of equation (6.50) is:

$$[(I - B^1 G^{12} B^2 G^{21})^{-1} B^1 G^{12} B^2 G^{21} B^1]_{ij} = \sum_{s=N+1}^{N+M} B_{is} [G^{21} B^1]_{sj} \tag{6.51}$$

In fact,

$$\mathbf{G^{21} B^1} = \mathbf{B^{22}}^{-1} \mathbf{B^{21}} \tag{6.52}$$

Therefore equation (6.50) becomes:

$$B^1_{ij} = B_{ij} - \sum_{s=N+1}^{N+M} \sum_{t=N+1}^{N+M} B_{is} {B^{22}}^{-1}_{st} B_{tj} \tag{6.53}$$

This gives a generalized form of equation (6.18).

6.4 Conclusion

We are able to predict the results of multi-tip STM experiments from the results of one-tip experiments. The one-tip experiment measures the local density of states, which can be expressed in terms of the diagonal of the energy Green's function. One might have thought that it is impossible to extract any transport properties of the surface solely from the diagonal information. However, the singular value decomposition method shows that for systems where multiple scattering works, it is possible to determine the scattering T-matrix of the scatterers, and therefore the off-diagonal Green's function, once enough data points have been taken.

We have related STM topographs with similar configurations of scatterers. Green's functions of similar configurations of scatterers are related through relatively simple expressions. In particular, the Green's function of a configuration of N localized scatterers completely determine the Green's functions of the configuration with scatterers removed from the original configuration.

Chapter 7

Proximity Scattering, Wall Scattering, and more

7.1 Introduction

As mentioned in previous chapters, the “Quantum Corral” experiments have Fe adatoms wall that is very “leaky”. A natural question to ask will be: How can we build a better wall? Because of the simplicity of the multiple scattering theory, we can build small as well as large structures with s-wave scatterers very easily. In this chapter, we are dedicated to study atomic walls built with s-wave scatterers. Once again, we will limit ourselves to the 2D systems. First, we need to specify the properties of s-wave scatterers as we don’t want any pillow-like scatterers. Second, we shall begin our study with the “two-atom wall”. This will lead us to the subject of proximity resonance. Third, we will give in to the temptation to learn about the scattering properties of certain small structures of s-wave scatterers. Lastly, we can finally look at scattering off a wall of atoms, both infinite and finite.

7.2 Picking the Right Atom

How should we model for the physical scatterers? In the "Quantum Corral" experiments, the walls are built with Fe adatoms on Cu(111). Their walls are very leaky not because of the gap between neighbouring adatoms, but because of the attenuation by the Fe adatom per se. The Fe adatom can couple the surface state electron to the bulk state, causing loss of coherence. Moreover, because of the magnetic nature of Fe atoms, there will be some loss of coherence due to spin-flip by the Fe adatoms when the electron bounces on the Fe adatoms. Therefore, an Fe adatom acts more like a "pillow" than a "brick". And one can never build a strong wall with loads of pillows.

Therefore we shall only consider unitary S-matrix, S_0 in our problem. In other words, we will have a real phase shift δ_0. Hence, the t-matrix is given by equation (2.37):

$$-\frac{i}{4}t = \frac{e^{2i\delta_0} - 1}{2} \tag{7.1}$$

Although the phrase shift δ_0 is independent of the wavevector k in the "Quantum Corral" model, it generally does. (In the "Quantum Corral" experiment, the Fe adatoms are black dots that absorb everything at all the energy concerned in the experiment. Thus, it always corresponds to the case with $\frac{-it}{4} = \frac{-1}{2}$.) And how? The dependence is determined by the nature of the potential. The natural thing to try will be the well/barrier potential as well as its variations. This is a reasonable model because the Sridhar group at Northeastern University can build disc like potentials with dielectric material in microwave cavity. However, this kind of potential does not give sharp peak in the single scatterer cross section, even with the "barrier/well combo" to force a resonance. This type of mathematical potentials are unlike real atoms, which have internal structures and do have sharp resonance peaks. Therefore, I have to find something else!

Using the criteria in section 7.7 of Sakurai[sak], S_0 needs to satisfy the following:

1. Pole at $k = k_0 + ik_{im}$
2. $|S_0| = 1$ for $k > 0$ (unitarity)
3. $S_0 = 1$ at $k = 0$ (threshold behavior)

The S-matrix can be of the following form:

$$S_0 = \frac{1 + ikR(k)}{1 - ikR(k)} \tag{7.2}$$

,where $R(k)$ is a real function of k. Such function will satisfy all of the above three criteria.

In particular, if we pick the function $R(k)$ to be:

$$R(k) = R_0 + \frac{2\gamma^2}{k_0^2 - k^2} \tag{7.3}$$

, where R_0,γ, and k_0 are all real. This $R(k)$ will have a background part R_0 and yield a resonance at k_0 and a width of $2k\gamma^2$ (in energy). This will yield a sharp peak in the single atom cross section, as shown in fig 7.1 with no background and in fig 7.2 with $R_0 = 1$.

Using this definition of $R(k)$, the S-matrix is therefore given by:

$$S_0 = \frac{(k_0^2 - k^2)(1 + ikR_0) + 2ik\gamma^2}{(k_0^2 - k^2)(1 - ikR_0) - 2ik\gamma^2} \tag{7.4}$$

And the t-matrix is:

$$\tau \equiv \frac{-it}{4} = \frac{2ik\gamma^2 + ikR_0(k_0^2 - k^2)}{(k_0^2 - k^2 - 2ik\gamma^2) - ikR_0(k_0^2 - k^2)} \tag{7.5}$$

In particular, I am interested in the case with no background scattering R_0. Having decided on the scattering properties of the "atom", I can start studying about the proximity resonance of two atoms.

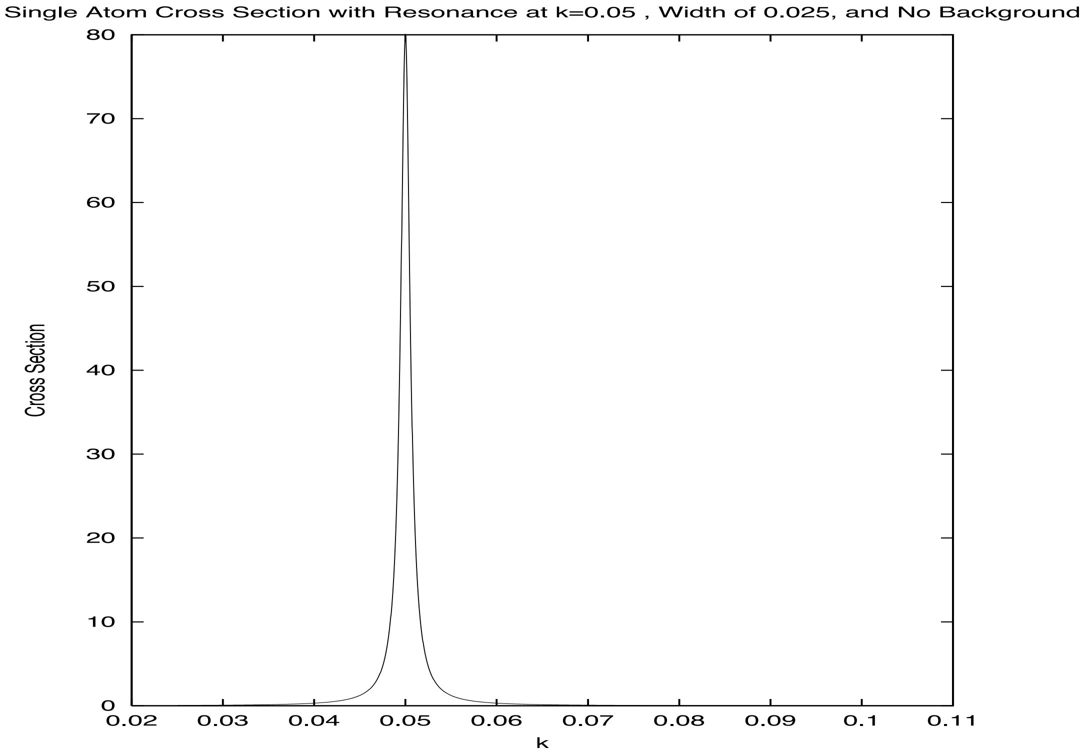

Figure 7.1: This is the single atom scattering cross section with a resonance at $k = .05$, a width of .000625, and no background ($R_0 = 0$).

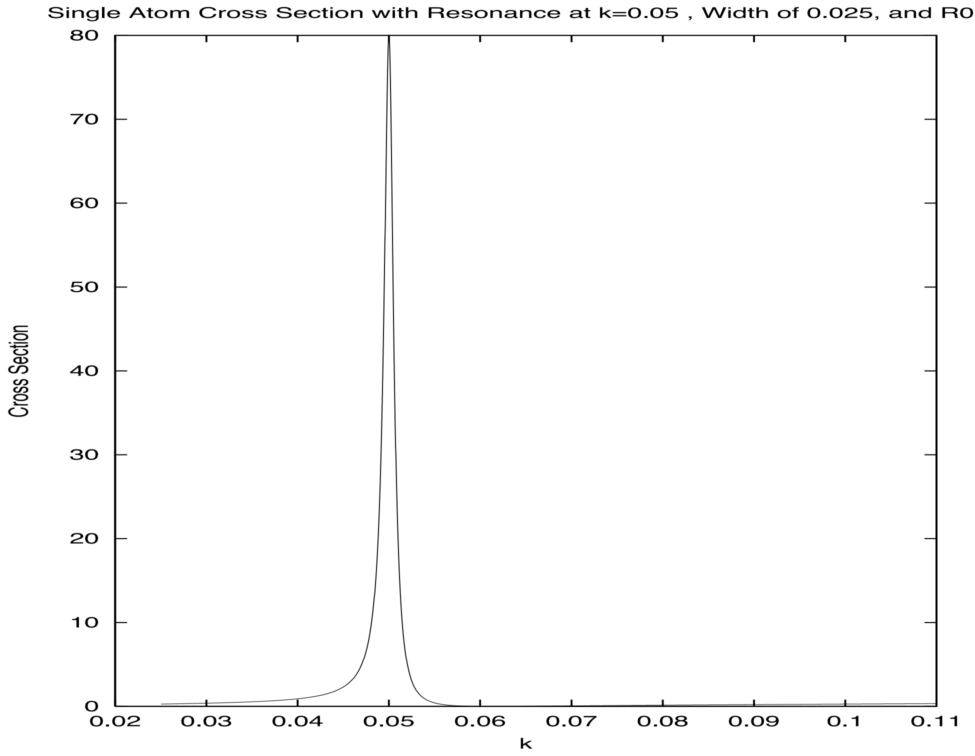

Figure 7.2: This is the single atom scattering cross section with a resonance at $k = .05$, a width of .000625, and $R_0 = 1$.

7.3 Proximity Resonance in 2D

In quantum scattering theory, each object has two characteristic cross sections. (In 2D, the cross section should be called the "cross length".) One is obviously the physical range of the potential. The other is the scattering cross section. In 2D, from chapter 2, we know that the cross section $\sigma \propto \frac{4}{k}$. At low energy, if we have an s-wave resonance, the cross section then goes like λ, which can be quite large and in some cases thousands of times larger than the physical range of the potential.

If two identical scatterers are more than their physical size apart, we can apply multiple scattering theory. However, as mentioned above, these scatterers can still be within the single scatterer cross section of each other. When this happens, it is no surprise to see something out of the ordinary. This is because when the wave scatters off one scatterer, it simply can't "miss" the other. At the correct k and separation d, the wave can bounce coherently back and forth between the scatterers for a long long time, causing a sharp resonance. Such resonance can be observed if I place two Fe adadtoms on Cu(111) too close together. This is called proximity resonance because the effect dies out as the separation increases.

Proximity resonance in 3D has been studied by Heller[hel96]. The observed examples include sound wave on air bubbles in water and light on molecular dipoles. In this section, I am going to present the 2D proximity resonance. Further, the effect of the asymmetric scatterers will be noted.

Using multple scattering theory, the wavefunction can be written as:

$$\psi(\vec{r}) \;=\; \psi^0(\vec{r}) + \psi^{scat}(\vec{r}) \tag{7.6}$$

$$= \quad e^{i\vec{k}\cdot\vec{r}} + \sum_{lm} e^{i\vec{k}\cdot\vec{r_l}} B_{lm} H_0^{(1)}(k|\vec{r} - \vec{r_m}|) \tag{7.7}$$

For the two scatterers at a separation of d and T-matrix τ_0, pick their locations to be at $\pm\frac{\vec{d}}{2}$. Let $h = H_0^{(1)}(kd)$. The total scattering T-matrix is:

$$\mathbf{B} = \frac{\tau_0}{1 - \tau_0^2 h^2} \begin{pmatrix} 1 & \tau_0 h \\ \tau_0 h & 1 \end{pmatrix} \tag{7.8}$$

Moreover, the Hankel functions can be rewritten in terms of Hankel functions centered at the origin:

$$H_0^{(1)}(k|\vec{r} - \vec{d}/2|) = \sum_{\nu=-\infty}^{\infty} H_\nu^{(1)}(kr) J_\nu(kd/2) e^{i\nu\phi} \tag{7.9}$$

$$H_0^{(1)}(k|\vec{r} + \vec{d}/2|) = \sum_{\nu=-\infty}^{\infty} H_\nu^{(1)}(kr) J_\nu(kd/2) e^{i\nu\phi}(-1)^\nu \tag{7.10}$$

Using equations (7.8),(7.9),(7.10), the scattered wave can be written as:

$$\begin{aligned} \psi^{scat}(\vec{r}) \quad = \quad & 2\tau_0(\frac{1}{1 - \tau_0 h}) \cos\frac{k_y d}{2} \sum_{\nu even} H_\nu^{(1)}(kr) J_\nu(kd/2) e^{i\nu\phi} \\ & -i(\frac{1}{1 + \tau_0 h}) \sin\frac{k_y d}{2} \sum_{\nu odd} H_\nu^{(1)}(kr) J_\nu(kd/2) e^{i\nu\phi} \end{aligned} \tag{7.11}$$

Taking the large distance limit, the scattered wave is of the following form:

$$\psi^{scat}(\vec{r}) = \sum_\nu f_\nu \frac{e^{ikr}}{\sqrt{r}} e^{i\nu\phi} \tag{7.12}$$

Therefore, for even ν,

$$f_\nu = \sqrt{\frac{2}{\pi k}} e^{i(-\pi/2-\nu\pi/2)} \cos\frac{k_y d}{2} J_\nu(kd/2) \frac{2\tau_0}{1-\tau_0 h} \tag{7.13}$$

For odd ν,

$$f_\nu = \sqrt{\frac{2}{\pi k}} e^{i(-\pi/2-\nu\pi/2)} \sin\frac{k_y d}{2} J_\nu(kd/2) \frac{-2i\tau_0}{1-\tau_0 h} \tag{7.14}$$

Thus, the partial wave cross section can be written as:

$$\sigma_\nu = 2\pi |f_\nu|^2 = \frac{16}{k} |\frac{\tau_0}{1-\tau_0 h}|^2 \cos^2\frac{k_y d}{2} J_\nu^2(\frac{kd}{2}) \tag{7.15}$$

for even ν.

And

$$\sigma_\nu = 2\pi |f_\nu|^2 = \frac{16}{k} |\frac{\tau_0}{1+\tau_0 h}|^2 \sin^2\frac{k_y d}{2} J_\nu^2(\frac{kd}{2}) \tag{7.16}$$

for odd ν.

Resonance happens when $1 \pm \tau_0 h = 0$. (The plus corresponds to odd ν whereas the minus corresponds to even ν.) Unlike the 3D case, in 2D, we cannot approximate $h = H_0^{(1)}(kd)$ by any polynomial in kd at low energy. This is because the Hankel function becomes logarithmic at low k, which cannot be written as a power series. Further, the p-wave resonance doesn't exist if the incident wave is normal to the line of scatterer because that mode doesn't get excited.

Figure 7.3 shows the results of a typical proximity resonance in 2D. The cross section of the single scatterer peaks at $k = 0.05$ and has a width of $\gamma^2 = 0.000625$. We have assumed that the incident wave is at one radian to the normal of the line of the two scatterers. Like the 3D case, the maximum of the S-wave cross section is shifted to a lower energy. Again, the width is about twice as broad. The p-wave resonance is shifted to higher energy, by about the same amount. The width for the p-wave resonance is much narrower, around 300 times narrower, than the S-wave.

When there is a background phase shift, $R_0 \neq 0$, the resonances can look similar or very different depending on the magnitude and slope of the background phase shift. The p-wave resonace can be broader, narrower than the background free case. And it can even be absent. The energy shifts can be reversed. In figures 7.4 and 7.5, the results with $R_0 = 1$ and $R_0 = 10$ are shown. We can see that the differences are quite significant.

Further, we shall check that such resonances are indeed proximity resonances. In other words, the effect goes away as the separation d tends to infinity. As I have mentioned, the poles of the denominators in the cross sections cannot be solved algebraically by Taylor expansion. Instead, we have to solve the following numerically:

$$1 \pm \tau_0 h = 0 \tag{7.17}$$

In figures 7.6, the locations of the S-wave and P-wave resonances are shown. As the separation d goes to infinity, the location of the peaks oscillates around the single atom value, i.e. $k = 0.05$. Similarly, as shown in figure 7.7, the width of and s-wave and p-wave resonance both oscillates the single scatterer value 0.000625. This means that the narrow proximity resonance peak goes away (by becoming as broad as the single atom case) as the two scatterers move away from each other. Another interesting point is that the S-wave and P-wave cross section oscillates at around π out of phase from one another. The s-wave resonance k_{res} peaks at around separation with $k_0 d = (2n+1)\pi$ whereas p-wave peaks at $k_0 d = 2n\pi$. The location of peaks for the width are at the same location for for s-wave and p-wave. A peak of s-wave corresponds to a trough of p-wave. This is like the case with two air bubbles in jello. The radius of the air bubble oscillates. If the two bubbles are in phase, then there is a s-wave resonance (i.e.s-wave resonance width small). If they are exactly out of phase by π, then there is a p-wave resonance (p-wave resonance width small). (When the separation is small, energy is trapped for a long while between the two bubbles because one radiates as the other absorbs, causing proxmity resonance.)

7.3.1 Asymmetric scatterers

Thus far, only the case with two identical scatterers has been considered. What happens if we put two scatterers of different species close together? Intuitively. the proximity resonance should go away as the two scatterers become different enough from one other. By restricting ourselves to backgroundless scattering, we can vary the width of the resonance of one of the scatterers. In figure 7.8 and 7.9, the cross sections of the scatterers with resonance at $k = 0.05$ and widths of γ^2, where $\gamma = 0.025, 0.022$ respectively, are shown. Agreeing with our intuition, the proximity resonance width becomes larger due to the asymmetry.

7.4 Scattering by Small Structures

In the previous section, we have studied the case of proximity resonance in 2D. Now, instead of using the two scatterers, we are going to build small structures with the scatterers. In particular, we are going to build tiny circles with more of the s-wave scatterers evenly spaced along them. Therefore, $\vec{r_m} = R\cos(\frac{2m\pi}{N})\hat{x} + R\sin(\frac{2m\pi}{N})\hat{y}$ The scattered wavefunction is:

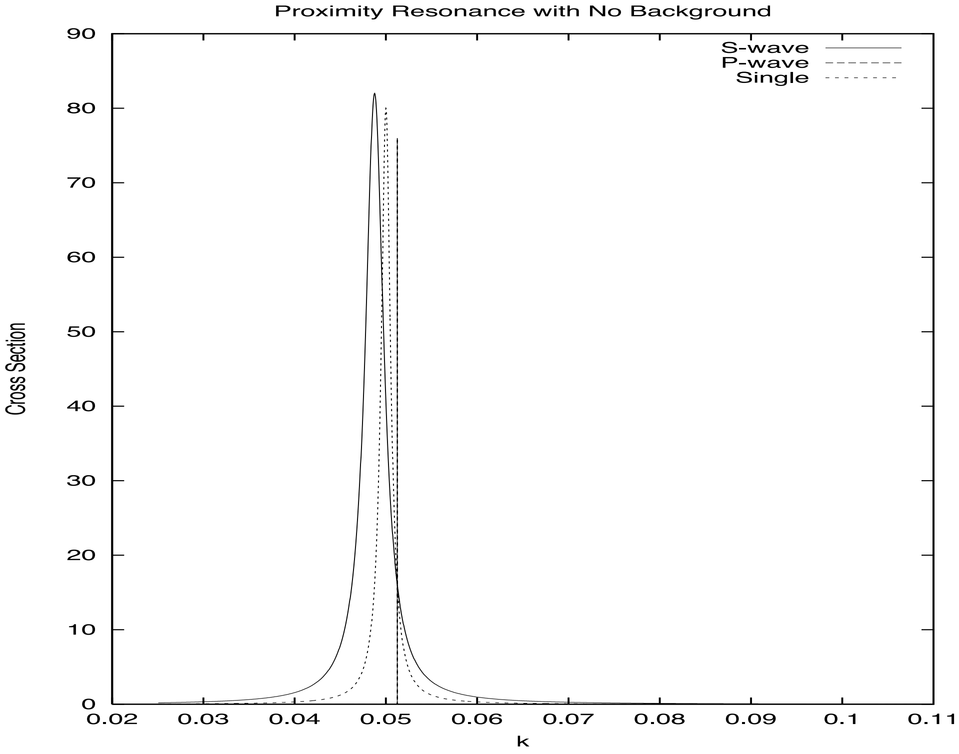

Figure 7.3: This is the cross section for quantum proximity resonance with no background. The single atom scattering cross section has a resonance at $k = .05$, a width of .000625, and $R_0 = 0$.

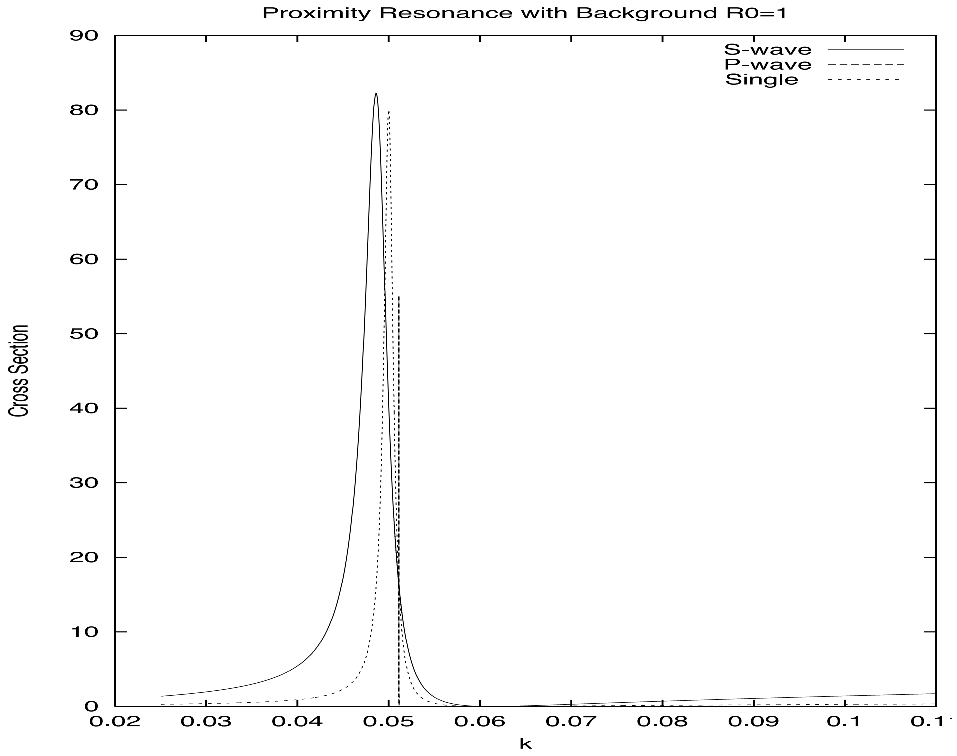

Figure 7.4: This is the cross section for quantum proximity resonance with background. The single atom scattering cross section has a resonance at $k = .05$, a width of .000625, and $R_0 = 1$.

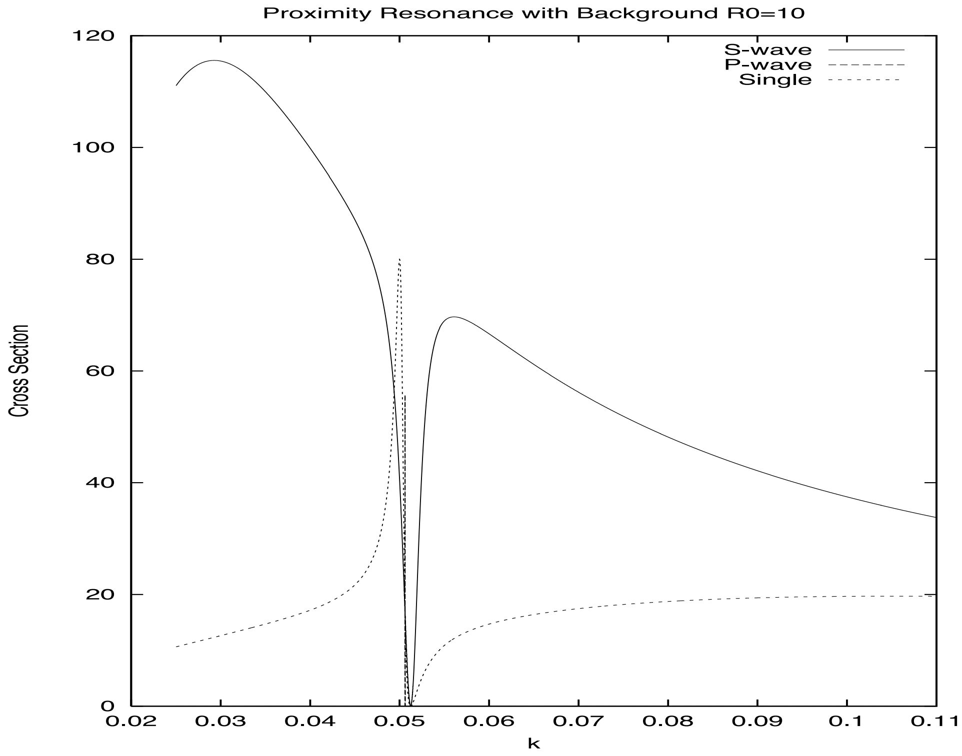

Figure 7.5: This is the cross section for quantum proximity resonance with background. The single atom scattering cross section has a resonance at $k = .05$, a width of .000625, and $R_0 = 10$.

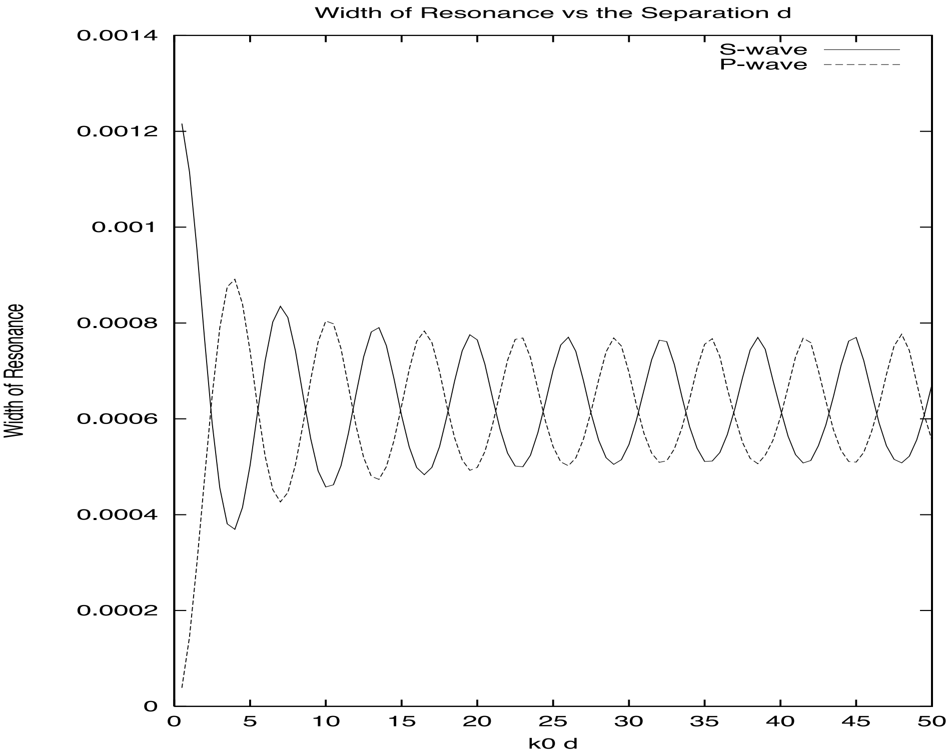

Figure 7.6: The resonance energy for the S-wave and P-wave cross section is plotted against the separation $k_0 d$.

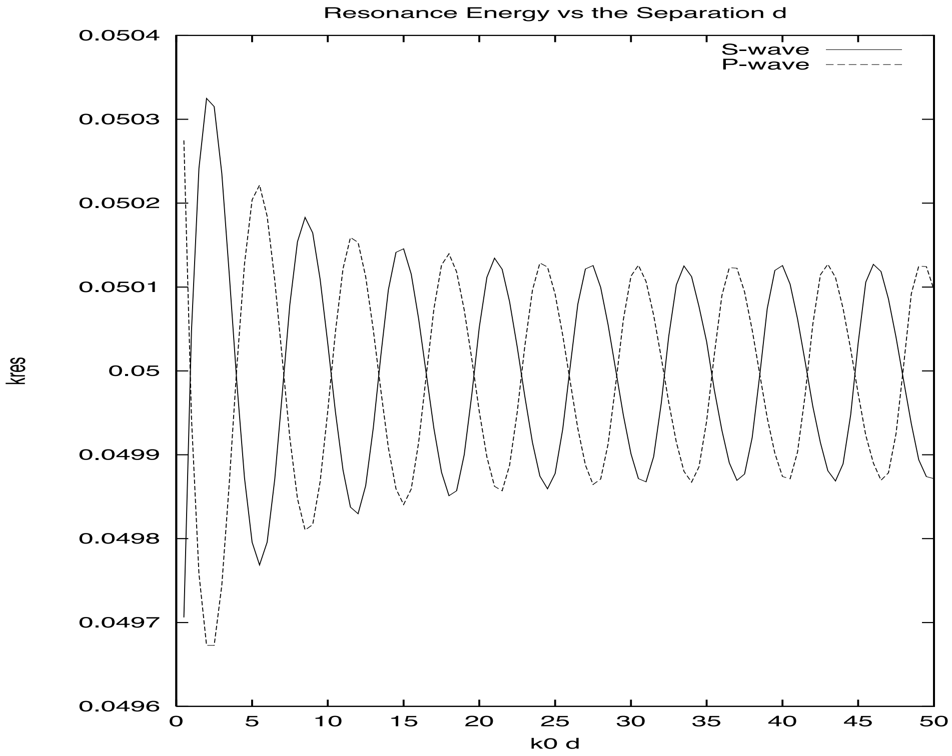

Figure 7.7: The resonance width for the S-wave and P-wave cross section is plotted against the separation $k_0 d$.

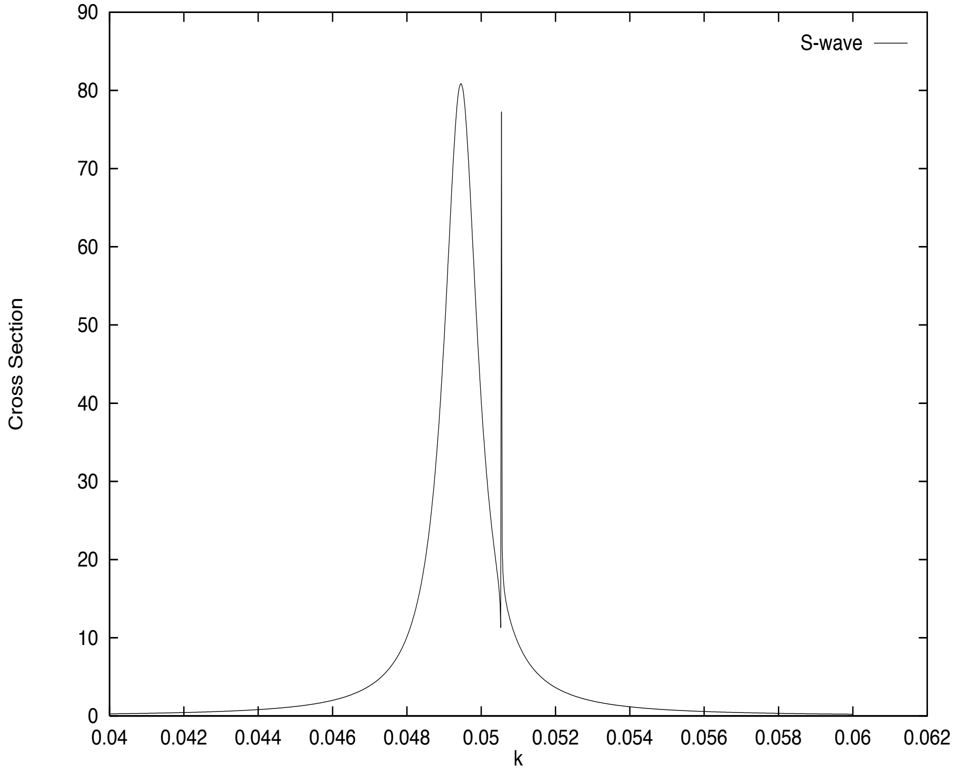

Figure 7.8: This is the S-wave cross section for quantum proximity resonance with no background for 2 asymmetric scatterers. The single atom scattering cross section has a resonance at $k = .05$, a width of .000625 and 0.000484, and $R_0 = 0$.

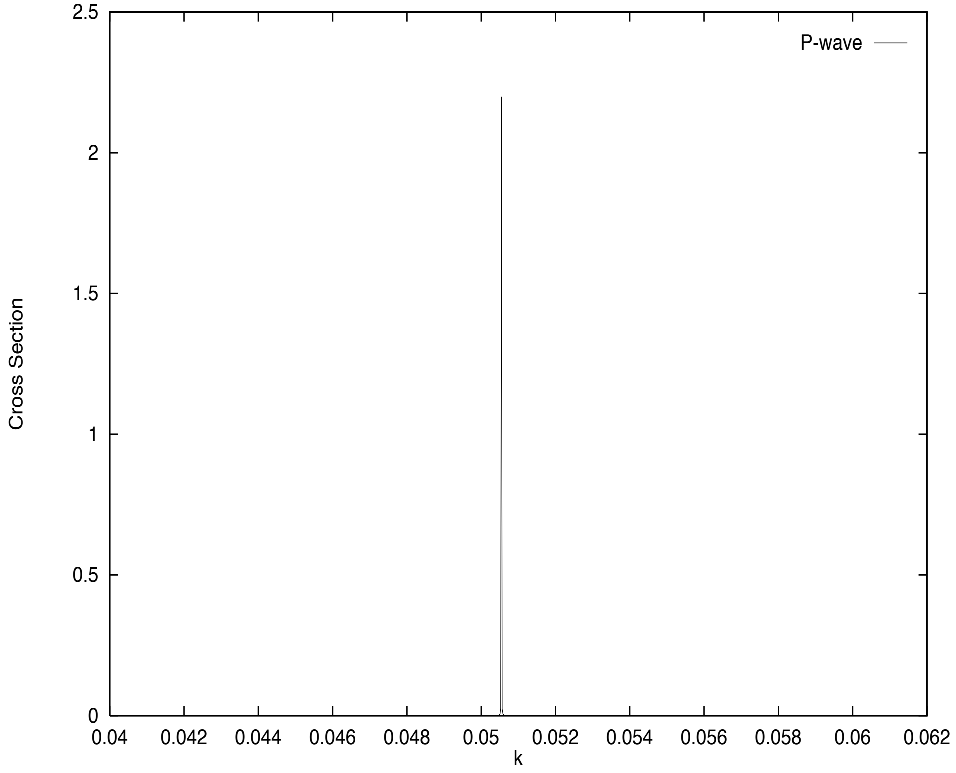

Figure 7.9: This is the P-wave cross section for quantum proximity resonance with no background for 2 asymmetric scatterers. The single atom scattering cross section has a resonance at $k = .05$, a width of .000625 and 0.000484, and $R_0 = 0$.

$$\psi^{scat}(\vec{r}) = \sum_{lm} e^{ikRcos(\phi_k - \phi_l)} B_{lm} H_0^1(k|\vec{r} - \vec{r_m}) \tag{7.18}$$

Using the fact that,

$$H_0^1(k|\vec{r} - \vec{r_m}|) = \sum_{\nu=-\infty}^{\infty} H_\nu^{(1)}(kr) J_\nu(kR) e^{i\nu(\phi - \phi_m)} \tag{7.19}$$

As a results, the scattering amplitude is:

$$f_\nu = \sqrt{\frac{2}{\pi k}} J_\nu(kR) \sum_{lm} e^{ikRcos(\phi_k - \phi_l)} B_{lm} e^{i\nu(\phi - \phi_m)} \tag{7.20}$$

The cross section is:

$$\sigma_\nu = \frac{4}{k} |J_\nu(kR) \sum_{lm} e^{ikRcos(\phi_k - \phi_l)} B_{lm} e^{i\nu(\phi - \phi_m)}|^2 \tag{7.21}$$

Shown in figures 7.10 and 7.11 are the cross sections of circles built with 2 to 8 scatterers. Because of the C_N symmetry of the geometry, there can only be one s-wave peak, one p-wave peak, and higher partial wave peaks with much smaller amplitudes. As the number of scatterers increases the s-wave resonance becomes broader and shifted more down from the single scatterer value. The p-wave resonance becomes narrower and is shifted up more.

For more than 2 scatterers, the p-wave resonance always exists regardless of the angle of the incident wave. This is obvious because the wave cannot be normal to all of the lines joining any two scatterers across the diameter.

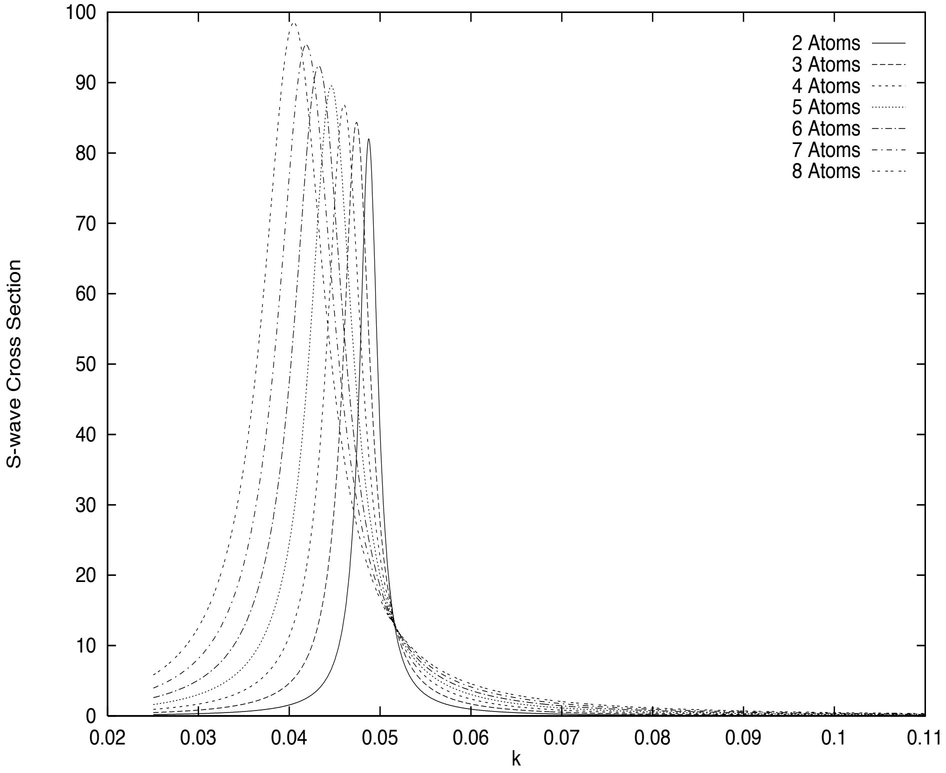

Figure 7.10: This is the S-wave cross section for 2-8 atoms on a circle with radius 1, with no background scattering. The single atom scattering cross section has a resonance at $k = .05$, a width of .000625, and $R_0 = 0$.

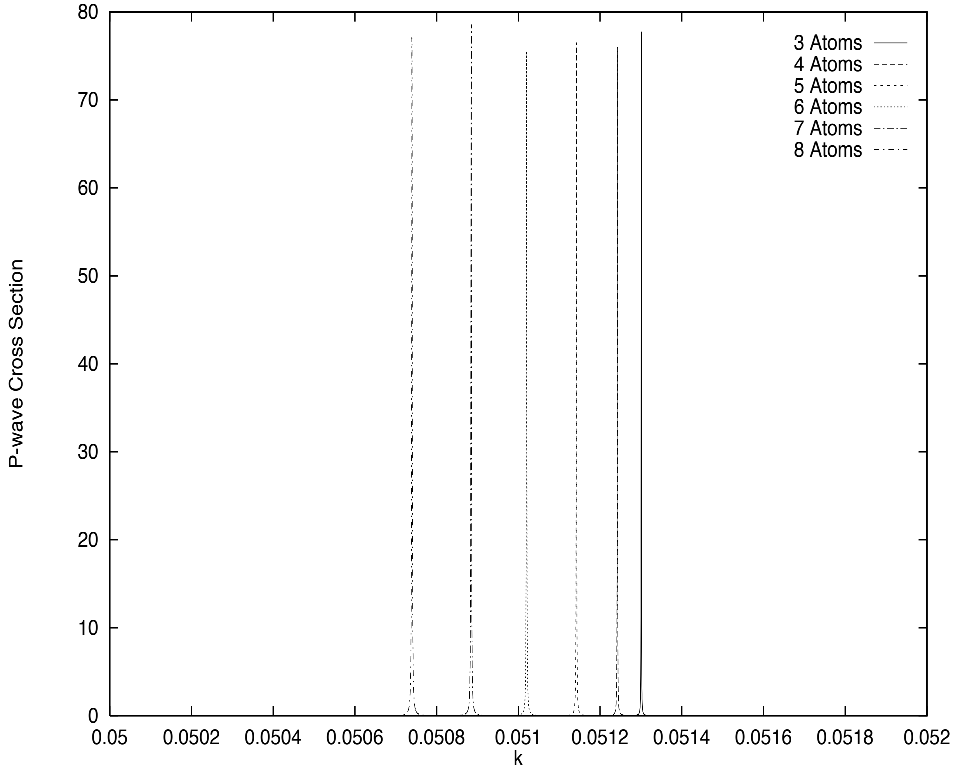

Figure 7.11: This is the P-wave cross section for 3-8 atoms on a circle with radius 1, with no background scattering. The single atom scattering cross section has a resonance at $k = .05$, a width of .000625, and $R_0 = 0$.

7.5 Scattering by Wall of Scatterers

Lastly, we are moving to the case where the results will be to the interest of many people. That is the scattering off a line of atoms. Scattering off a wall has been studied in many context. In particular, the problem with a hard mathematical boundary has been pursued by many, including the boundary wall approach[luz97]. However, in the real world, walls are made with real atoms instead of being a "dead" wall. Therefore, it would be interesting to see the scattering properties off a line of atoms.

7.5.1 Infinite Wall of Atoms

Like many physical problems, it is usually easier to study the infinite problem. Let us consider the scattering off an infinite wall of evenly spaced atoms and extract the transmittivity and reflectivity of the wall. Once again, I would like to restrict myself to the 2D problem. The spacing between neighbouring atoms is d. And we assume that the atoms lie on the y-axis($x = 0$) at $y = nd$, with n being an integer. Using multiple scattering theory, the total wave function with an incident plane wave is:

$$\psi(\vec{r}) = e^{i\vec{k}\cdot\vec{r}} + \sum_{lm} e^{i\vec{k}\cdot\vec{r_l}} B_{lm} H_0^{(1)}(k|\vec{r} - \vec{r_m}|) \tag{7.22}$$

In particular,

$$B_{lm} = \tau_m(\delta_{lm} + A_{lm} + A_{lm}^2 + \cdots) \tag{7.23}$$

, where $A_{lm} = \tau_l H_0^{(1)}(k|\vec{r_l} - \vec{r_m}|)$.

To solve the problem, consider the following sum:

$$
\begin{aligned}
S &= \sum_{l} e^{i\vec{k}\cdot(\vec{r_l}-\vec{r_m})}\tau_l H_0^{(1)}(k|\vec{r_l}-\vec{r_m}|) && (7.24)\\
&= \sum_{n} e^{ik_y nd}\tau_0 H_0^{(1)}(k|nd|) && (7.25)
\end{aligned}
$$

as $\tau_l = \tau_0$ for all l (identical scatterers). It is impossible to sum this up in closed form. Therefore, we have to take the low energy limit. When $kd << 1$, $k_y d << 1$. Define $\delta t = k_y d$. The sum can be rewritten as:

$$
\begin{aligned}
S &= \frac{1}{\delta t}\sum_{n} e^{in\delta t}\tau_0 H_0^{(1)}(\frac{k}{k_y}n\delta t)\delta t && (7.26)\\
&\approx \frac{1}{k_y d}\int_{\infty}^{\infty} dte^{it} H_0^{(1)}(\frac{k}{k_y}t) && (7.27)\\
&= \frac{2\tau_0}{k_x d} && (7.28)\\
&\equiv S' && (7.29)
\end{aligned}
$$

by approximating the sum by an integral and using the following identity:

$$
\int_{\infty}^{\infty} dye^{ik_y y} H_0^{(1)}(k\sqrt{x^2+y^2}) = \frac{2e^{ik_x|x|}}{k_x} \qquad (7.30)
$$

In fact,

$$
\sum_{l} e^{i\vec{k}\cdot(\vec{r_l}-\vec{r_m})}B_{lm} = \sum_{n} S^n\tau_0 = \frac{\tau_0}{1-S} \qquad (7.31)
$$

Thus,

$$
\psi(\vec{r}) = e^{i\vec{k}\cdot\vec{r}} + \sum_{lm}\frac{\tau_0}{1-S}e^{i\vec{k}\cdot\vec{r_m}}H_0^{(1)}(k|\vec{r}-\vec{r_m}|) \qquad (7.32)
$$

$$\approx \quad e^{i\vec{k}\cdot\vec{r}} + \sum_{lm} \frac{\tau_0}{1-S'} e^{i\vec{k}\cdot\vec{r_m}} H_0^{(1)}(k|\vec{r}-\vec{r_m}|) \tag{7.33}$$

Approximating the sum by an integral again,

$$\sum_m e^{i\vec{k}\cdot\vec{r_m}} \tau_0 H_0^{(1)}(k|\vec{r}-\vec{r_m}|) = \frac{2\tau_0 e^{i(k_x|x|+k_y y)}}{k_x d} \tag{7.34}$$

As a result,

$$\psi(\vec{r}) \approx e^{i\vec{k}\cdot\vec{r}} + \frac{2\tau_0/k_x d}{1-2\tau_0/k_x d} e^{i(k_x|x|+k_y y)} \tag{7.35}$$

So the transmission coefficient is:

$$tc = 1 + \frac{2\tau_0/k_x d}{1-2\tau_0/k_x d} \tag{7.36}$$

And the reflection coefficient is:

$$rc = \frac{2\tau_0/k_x d}{1-2\tau_0/k_x d} \tag{7.37}$$

The transmittiviy $\mathcal{T} = |tc|^2$ and reflectivity $\mathcal{R} = |rc|^2$ of a wall using the scatterers in the previous section as function of energy are plotted in figures 7.12 respectively. The transmittivity is low when the single scattering cross section is high. This is reasonable since the atom wall becomes more efficient when the atoms are "turned on."

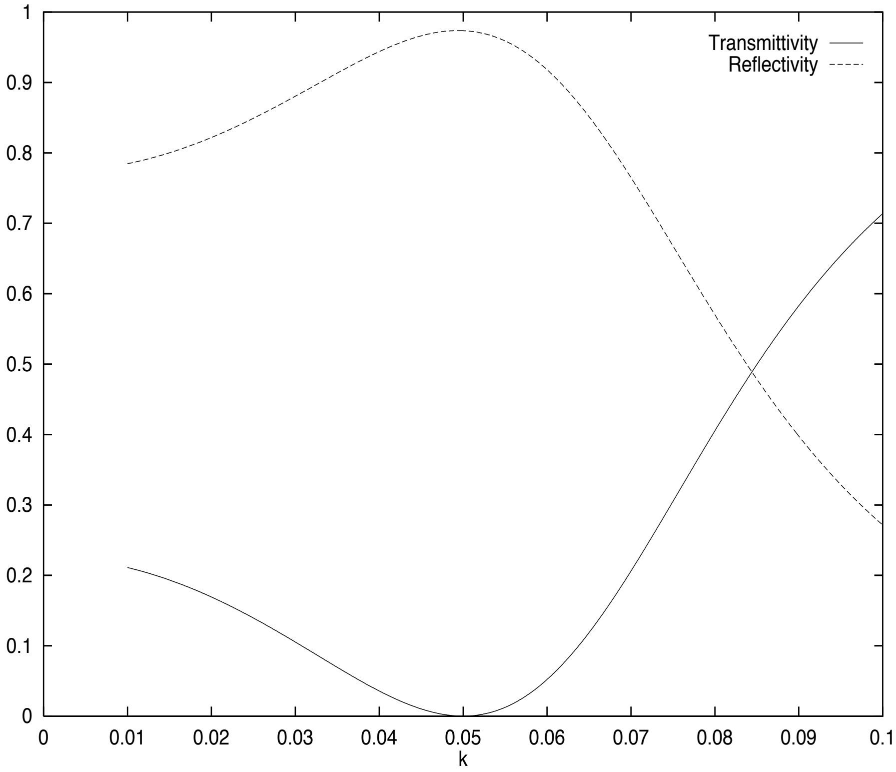

Figure 7.12: The transmittivity and reflectivity of an infinite wall of scatterers are plotted against k. The scatterers are spaced at d away from one another. The single scatterer cross section has a peak at $k_0 = 0.05$ and a width of 0.000625. Again, the incident plane wave is 1 radian to the normal of the wall.

7.5.2 Scattering off Finite Walls

In reality, an infinite wall hardly ever exists. Therefore we need to study the properties of finite walls as well. Once again, we are building the walls with the same scatterers that we have used in the previous sections. That is the one with a resonance at $k = 0.05$, width of $\gamma^2 = 0.000625$, and no background scattering $R_0 = 0$. The incident plane wave is 1 radian to the normal of the wall, which will excite the p-wave mode.

7.5.3 8 Atoms Wall

Let us start our adventure with 8 atoms lying on a line, at $d = 1$ apart. We would like to find the transmittivity as well as the reflectivity of the wall. But before we could do anything about it, we would have to straigthen out some definitions first. In the infinite wall case, the transimittivity and reflectivity comes naturally from the transmission and the reflection coefficients. However, in the finite case, we don't have the nice form in the total wavefunction. Therefore, we have to look at the shadow of the wall to define the transmittivity. Given the wall is long enough, we define the transmittivity to be:

$$\mathcal{T} = \frac{\left|\int_{-1/2}^{1/2} dy Im[\psi^* \nabla \psi]\right|}{k \cos \phi} \tag{7.38}$$

where at $x = x_0$ is in the shadow and ϕ is the incident angle of the incident wave to the normal of the wall.

Reflectivity is defined to be:

$$\mathcal{R} = \frac{\left|\int_{-1/2}^{1/2} dy Im[\psi_R^* \nabla \psi_R]\right|}{k \cos \phi} \tag{7.39}$$

where $\psi_R = \psi - \psi^0$ and at $x = -x_0$.

Armed with these definitions, we can calculate the transmittivity as well as the reflectivity of the 8 atoms wall. The transmittivity and the reflectivity are shown on figures 7.13 and 7.14. In addition to studying the transmittivity and reflectivity which calculates the properties in the shadow region, we can look at the S-wave and P-wave cross sections of the wall from far away. The expressions for partial wave scattering amplitudes are:

$$f_\nu = 2\sqrt{\frac{2}{\pi k}} \sum_{m=1}^{N/2} J_\nu(kr_m) \sum_{l=1}^{N/2} (B_{lm} + B_{l+N/2m}) \cos k_y r_l \tag{7.40}$$

for even ν, and

$$f_\nu = 2i\sqrt{\frac{2}{\pi k}} \sum_{m=1}^{N/2} J_\nu(kr_m) \sum_{l=1}^{N/2} (B_{lm} - B_{l+N/2m}) \sin k_y r_l \tag{7.41}$$

for odd ν.

The partial wave cross sections are therefore:

$$\sigma_\nu = \frac{16}{k} | \sum_{m=1}^{N/2} J_\nu(kr_m) \sum_{l=1}^{N/2} (B_{lm} + B_{l+N/2m}) \cos k_y r_l |^2 \tag{7.42}$$

for even ν, and

$$\sigma_\nu = \frac{16}{k} | \sum_{m=1}^{N/2} J_\nu(kr_m) \sum_{l=1}^{N/2} (B_{lm} - B_{l+N/2m}) \sin k_y r_l |^2 \tag{7.43}$$

for odd ν.

And the results for the S-wave and P-wave are shown on figures 7.15 and 7.16 respectively. Comparing these with the transmittivity plot, one can see that low transmittivity corresponds to high cross sections.

Further, the peaks we observe in the cross sections correspond to resonance states along the wall. At resonance energies, the wavefunction is large along the walls. And these are like “conducting” states and conductors are good screens, causing low transmittivity. In particular, the s-wave peaks and p-wave peaks correspond to wavefunctions of the respective characters. Some sample wavefunctions along the wall are shown on figures 7.18 thru 7.20.

7.5.4 Band Structure of the 8 Atom Wall

As we have seen, there are states along the wall at resonance energies. What wavevectors do these energies correspond to along the wall? If we know that, we know the dispersion relation of the 8 atoms wall. As we have the wavefunctions along the wall at these energies, we can fourier transform them. In particular, I have found peaks at particular wavevectors corresponding to each of the wavefunctions. By plotting the energy against these wavevectors, we have the dispersion relations of the wall. The results is shown on figure 7.21 and 7.22. This is an example of the band structure of a finite 1D object embedded in 2D.

7.6 Conclusion

We have proved the existence of 2D proximity resonance by reproducing results similar to the 3D one[hel96]. The scattering off small circles has also been investigated. Lastly, by studying the scattering off a finite wall yields a first band structure calculation of a finite 1D object embedded in 2D.

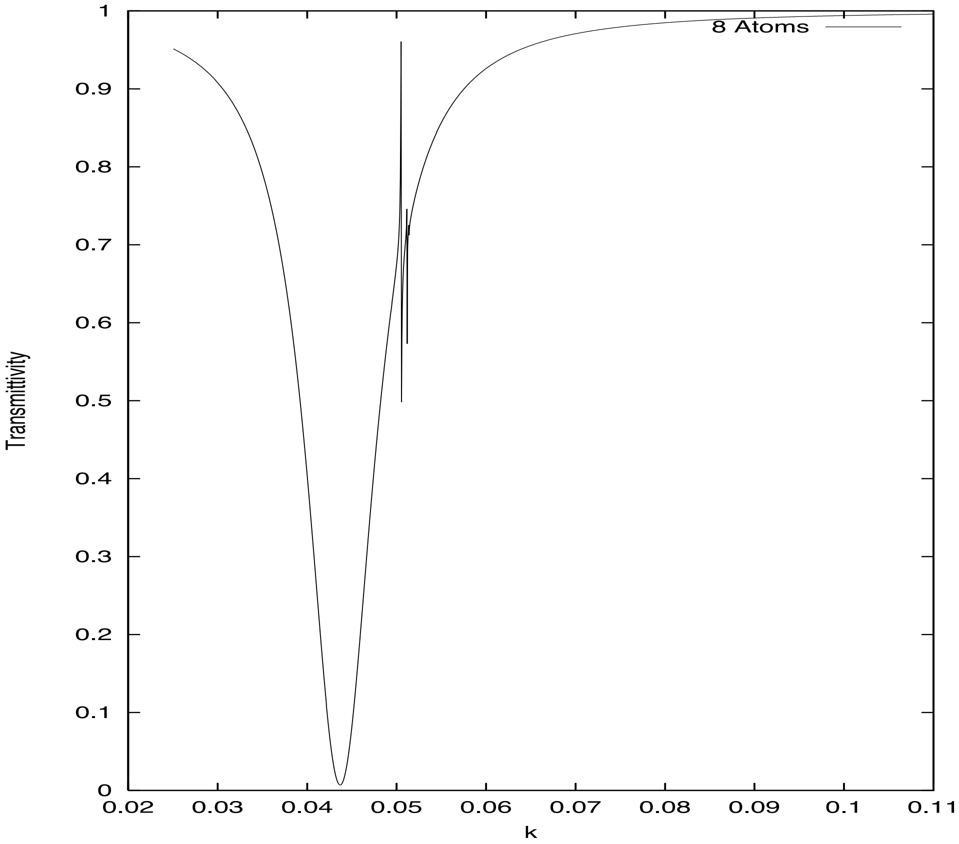

Figure 7.13: Shown is the transmittivity through a wall of 8 atoms.

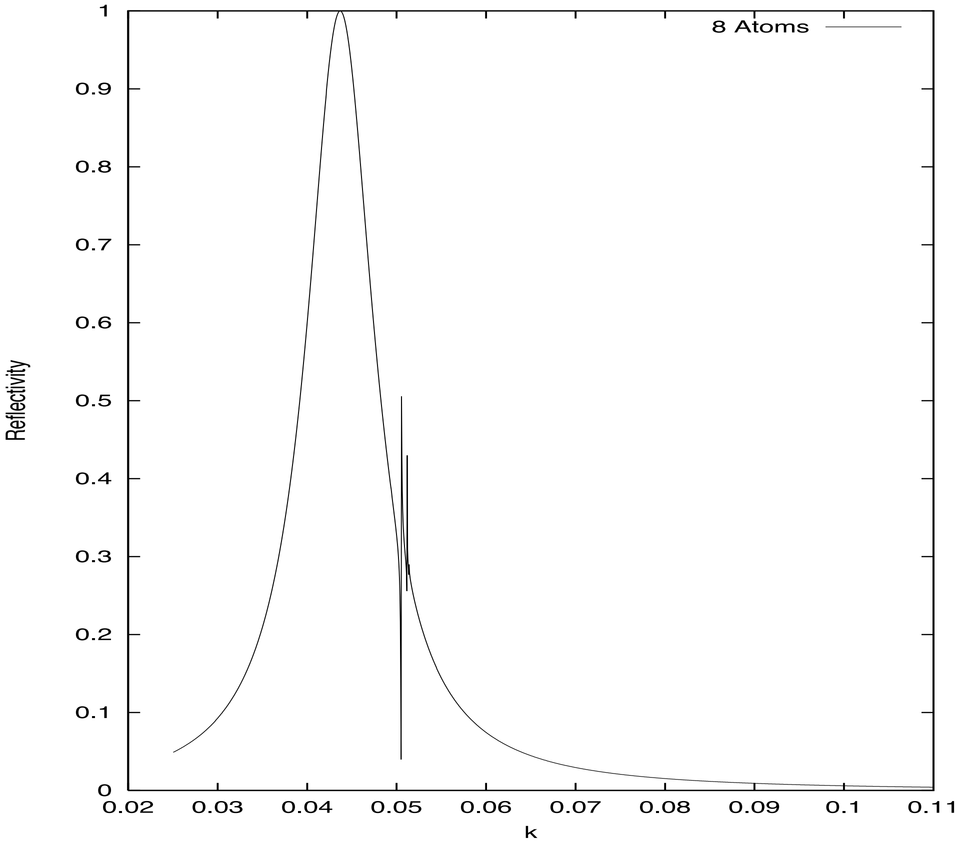

Figure 7.14: Shown is the reflectivity through a wall of 8 atoms.

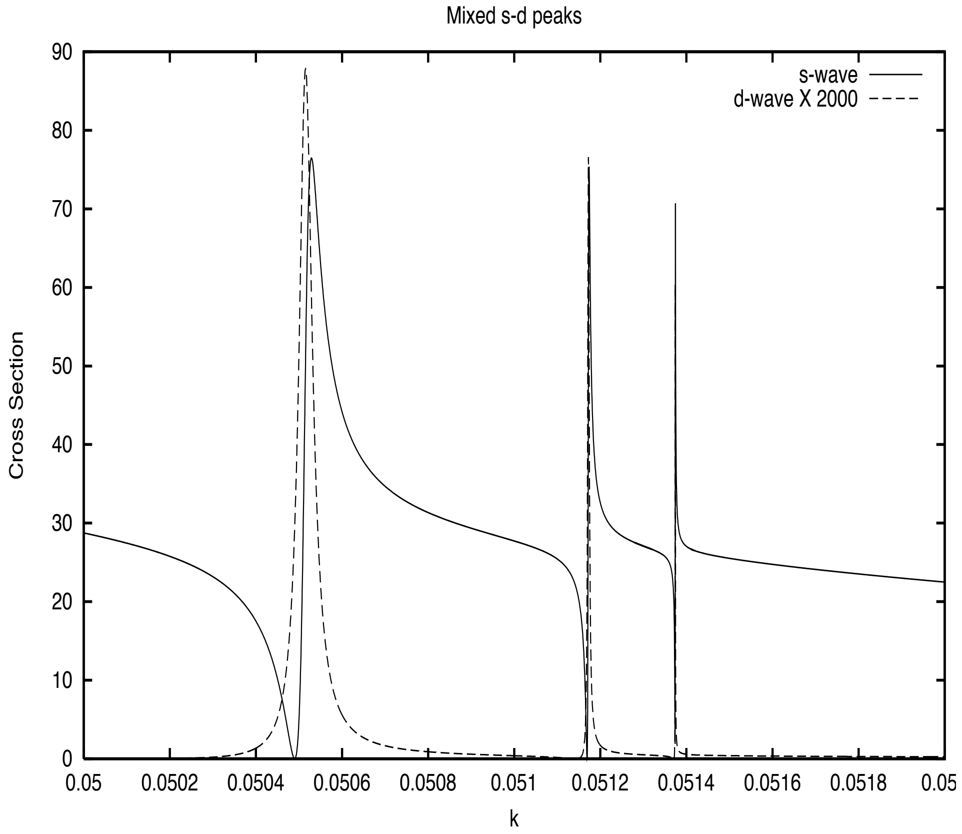

Figure 7.15: The s-wave and d-wave cross sections for a wall of 8 atoms is shown.

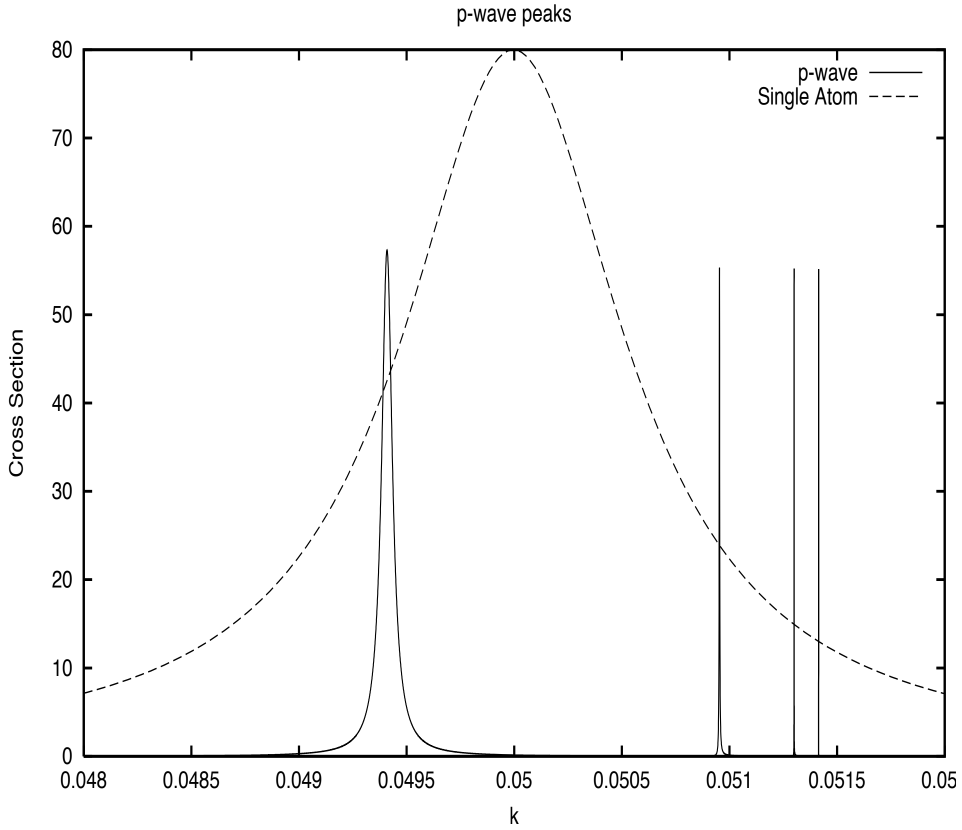

Figure 7.16: The p-wave cross section for a wall of 8 atoms is shown.

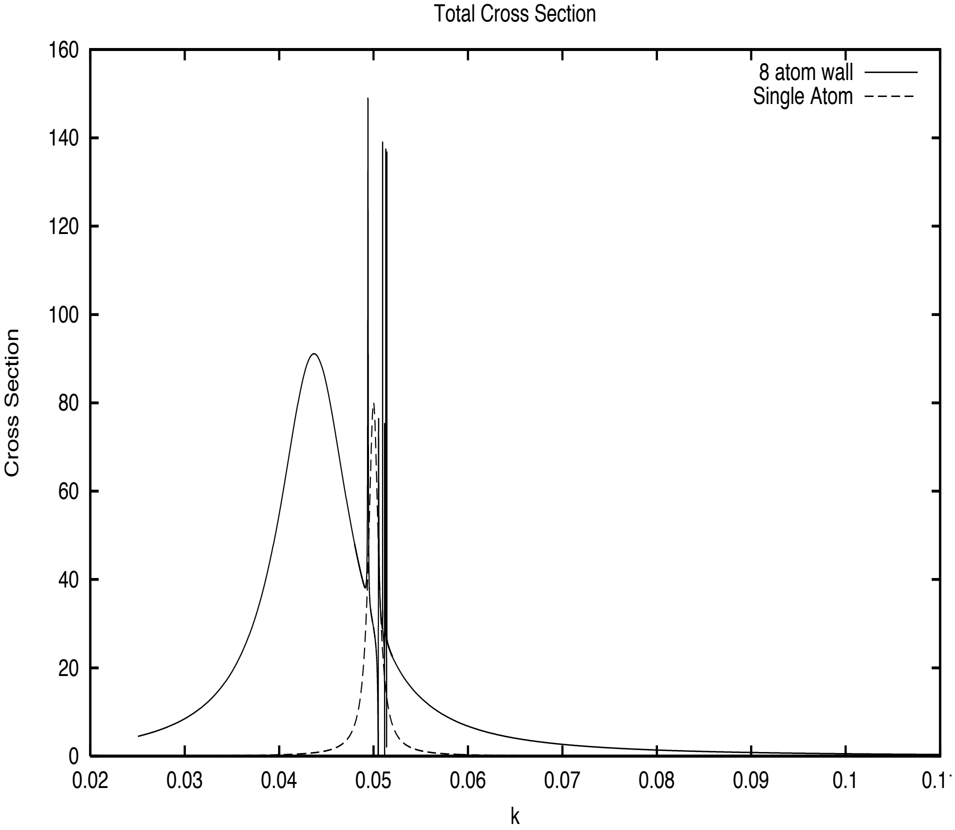

Figure 7.17: The total cross section for a wall of 8 atoms is shown.

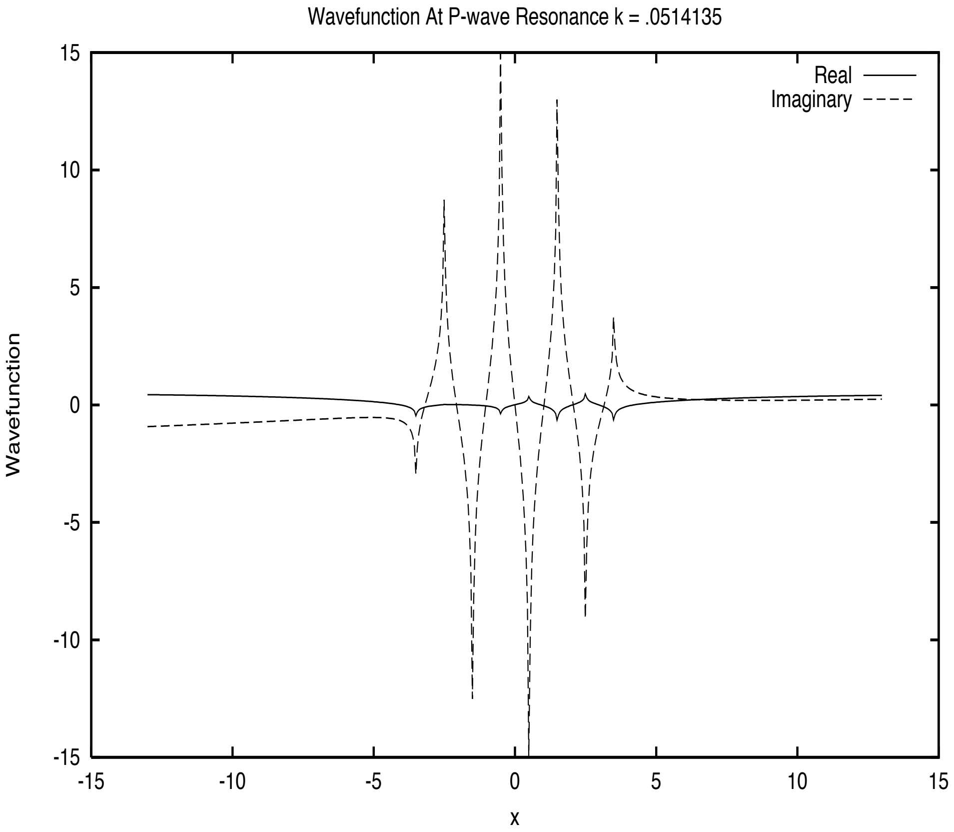

Figure 7.18: The wavefunction at p-wave resonance, $k = 0.0514135$, for a wall of 8 atoms is shown. This shows p-wave characteristics.

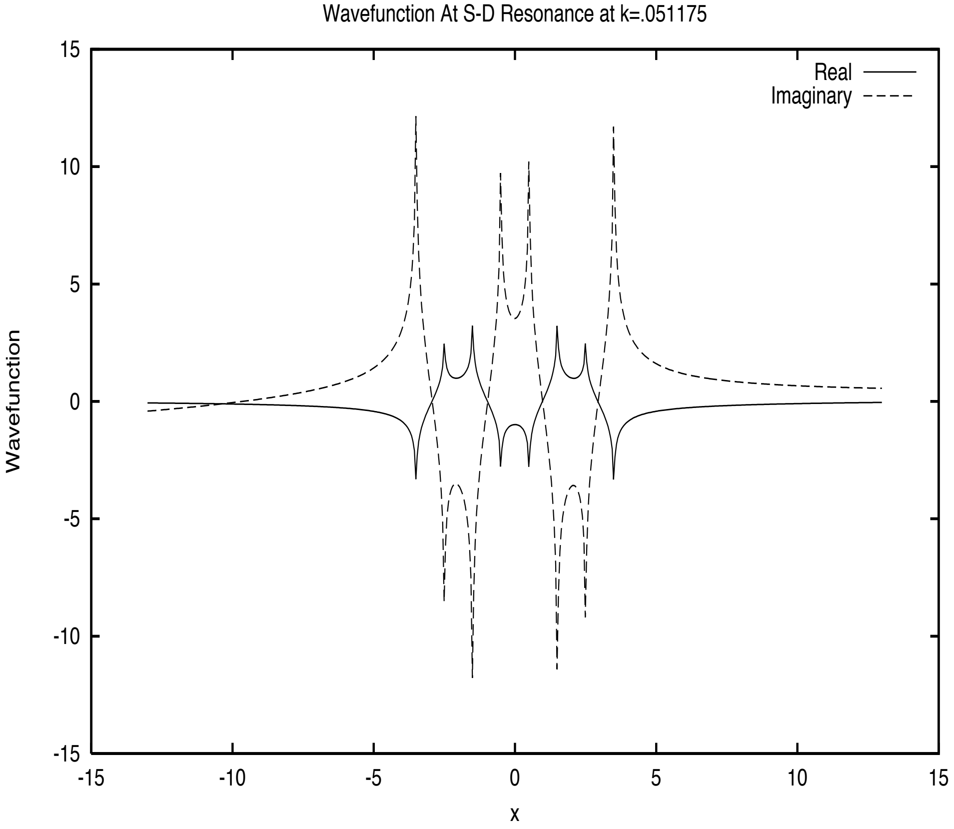

Figure 7.19: The wavefunction at s-wave and d-wave resonance, $k = 0.051175$, for a wall of 8 atoms is shown. This shows s-d mixed characteristics.

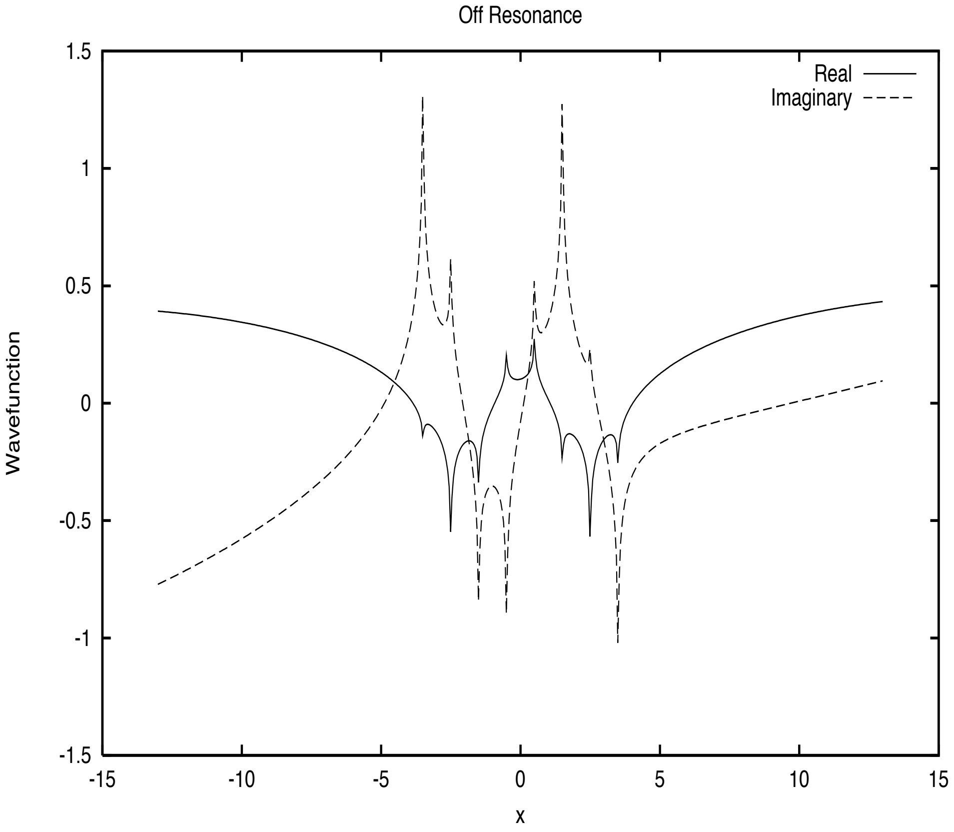

Figure 7.20: The wavefunction at a non-resonance energy for a wall of 8 atoms is shown. The amplitude along the wall is not as big as the ones on resonance.

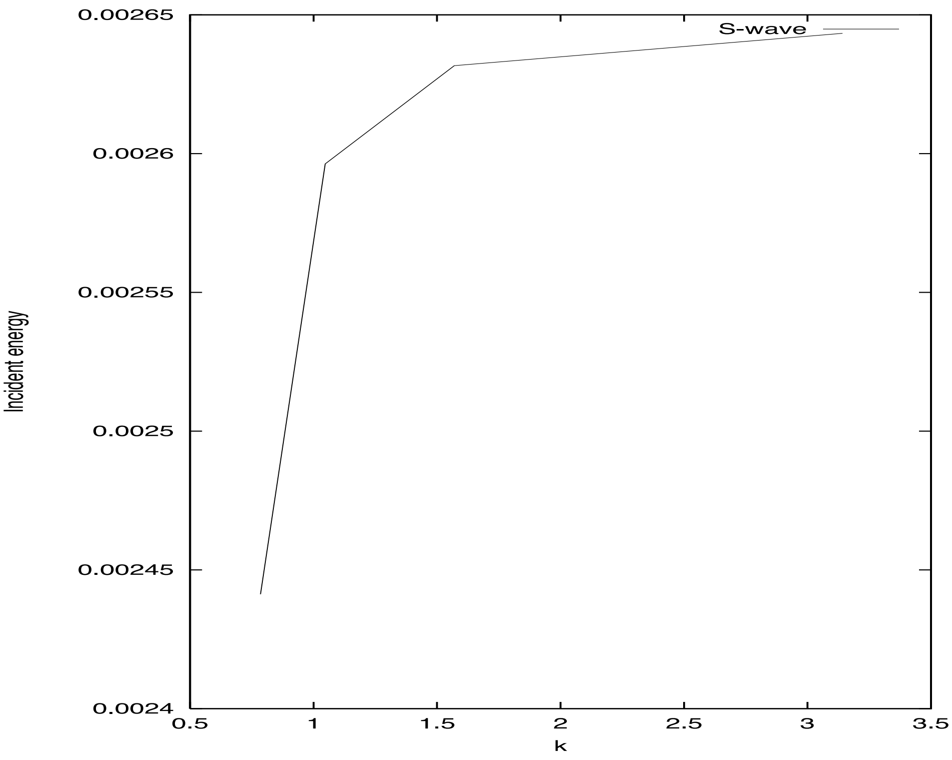

Figure 7.21: The energy vs wavevector of the S-wave resonance states are plotted.

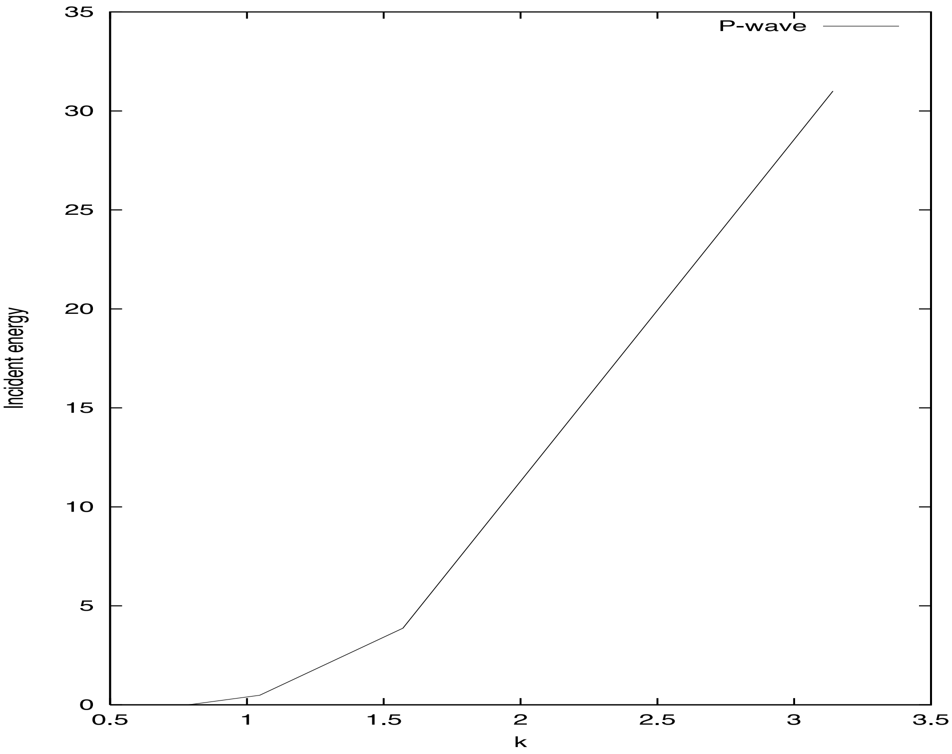

Figure 7.22: The energy vs wavevector of the P-wave resonance states are plotted.

Chapter 8

Theories of Coherent Backscattering

8.1 Introduction

In mesoscopic systems, elastic scattering of electrons by impurities leads to backscattering trajectories. Since these scattering events are coherent and preserve the memory of phase, the backscattered trajectory can interfere with the forward one. As a result, the resistance increases and the effect is known as weak localization. If a perpendicular magnetic field is applied, the Green's function of a closed trajectory picks up an extra phase proportional to the area enclosed and the magnetic field. The increase in the resistance should therefore be suppressed. Experiments have been performed to observe this effect. In particular, the Westervelt group[kat96] has built a nanostructure with a pair of reflectors behind a gate. Such reflectors are shaped and aimed so that the trajectories will be pointed back to the gate and the areas enclosed are about the same. Since the reflectors and the gates are mathematical hard walls, we can use the boundary wall method to model these walls. In the absence of other impurities, such reflectors should cause oscillation in resistance as the magnetic field varies (Aharonov-Bohm effect). However, in real life, impurities are present. Therefore, by combining the boundary wall method with the S-wave multiple scattering theory, we can build a model for the reflectors and gates with lots of impurities.

8.2 Review of the Westervelt Experiment

The experiment is performed on $GaAs/Al_{.3}Ga_{.7}As$ heterostructure at a temperature of $385mK$ inside a superconducting solenoid that produces the perpendicular magnetic field. There is a 2DEG lying $520\mathring{A}$ beneath the surface of the sample. The Fermi wavelength of the electron is $43nm$, and the width of the gate allows 4 modes to propagate through. Current I is passed through the gate and the voltage across the nanostructure is measured. The results are averaged over 25 such devices.

So how are the reflectors shaped? Assuming specular reflection only, the reflectors are designed so that if the wave from the origin hits the first one, it will bounce straight down to the second reflector at the same location, and then back to where it originates. Algebraically, we have:

$$x = f(\theta)\cos\theta \tag{8.1}$$

$$y = \pm f(\theta)\sin\theta \tag{8.2}$$

$$f(\theta) = \frac{2R_0}{1+\sin\theta} \tag{8.3}$$

where $R_0 = 975nm$ and $12^o < \theta < 30^o$. Detailed derivation of the expression is presented in appendix A.

The results of the experiment are plotted on figure 8.1. As you can see, the anticipated Aharonov-Bohm kind of oscillation is absent, possibly due to the impurities on the surface.

8.3 Modeling

In this section, we are going to build the models used for the setup in both the cases with and without impurities. The general philosophy is to apply the boundary wall method to the mathematical hard walls posed by the gates and the reflectors. Point-like S-wave scatterers are used to model for the impurities present. However, the Green's function formula used in previous chapters does not apply any more due to the presence of a perpendicular magnetic field. So what is the correct Green's function to use?

8.3.1 Green's Function in the Presence of a B-field

To handle systems with magnetic field, first we need to define the magnetic length l_m as well as the cyclotron frequency ω.

$$\omega = eB/m_e \tag{8.4}$$

$$l_m = \sqrt{\frac{\hbar}{m_e \omega}} \tag{8.5}$$

According to Ueta[uet], by solving the Schrödinger equation with a perpendicular non-zero magnetic field, the 2D Green's function is found to be:

$$\mathcal{G}(\vec{r}, \vec{r'}, \epsilon, B) = -\frac{1}{4\pi} \frac{\pi}{\cos \pi\epsilon} \frac{1}{\Gamma(\frac{1}{2} - \kappa)} \frac{W_{\kappa,0}(z)}{z^{1/2}} \exp(i(xy' - yx')/2l_m^2) \tag{8.6}$$

where $z = (r - r')^2/2l_m^2$ and $\epsilon = E/\hbar\omega$. By taking the low field limit,

$$G(\vec{r}, \vec{r'}, \epsilon, B) \rightarrow G(\vec{r}, \vec{r'}, \epsilon, 0)\exp(i(xy' - yx')/2l_m^2) \tag{8.7}$$

Equation (8.7) is what we are going to use for our free particle Green's function due to the fact that the experiment is performed at low field and the electron trajectories are not visibly curved.

8.3.2 Resistance

Until now, we have been talking about the resistance and Green's function in separate context. In order to build a model for the experiment, we have to know what the experiment is really measuring. The resistance the experiment measured has two parts, the classical and the quantum parts. The classical part can be accounted for by Drude's Theory and the quantum part is the one we need a model for. As mentioned in previous section, a current of I is passed through the gate and the voltage across the structure is measured. Using a definition similar to equation (7.38), the transmittivity through the gate is:

$$\mathcal{T} = \left| \int_{-w/2}^{w/2} Im[\psi^* \nabla \psi] \right| / k \tag{8.8}$$

where $x = 0$ is along the line of the gate.

Reflectivity is defined to be:

$$\mathcal{R} = \left| \int_{-w/2}^{w/2} Im[\psi_R^* \nabla \psi_R] \right| / k \tag{8.9}$$

where $\psi_R = \psi - \psi^0$ and at $x = 0$. These are both integrated over the opening of the gate. The conductance is[ando]:

$$G = \frac{e^2}{\pi\hbar}\mathcal{T} \tag{8.10}$$

This quantity must then be averaged over all incident angle of the wave.

The resistance is:

$$R = R_{\text{classical}} + 1/G \tag{8.11}$$

8.3.3 Application of the Boundary wall method

We need now to calculate the wavefunction to use our expression for the conductance.

Using the boundary wall method mentioned in chapter 2, the wavefunction can be written as:

$$\psi(\vec{x}) = e^{i\vec{k}\cdot\vec{x}} + \sum_{ij} e^{i\vec{k}\cdot\vec{x_i}} B_{ij}\mathcal{G}^0(\vec{x_j}, \vec{x}, \vec{k}) \tag{8.12}$$

$$\mathcal{G}^0(\vec{x_j}, \vec{x}, \vec{k}) = -\frac{1}{4} i H_0^{(1)}(k|\vec{x_j} - \vec{x}|) e^{i\phi_j(\vec{x})} \tag{8.13}$$

$$\phi_j(\vec{x}) = \phi(\vec{x_j}, \vec{x}) = \frac{B}{2}(-xy_j + x_j y) \tag{8.14}$$

Note that the Boundary Wall Method treats a continuous mathematical wall by discretizing it. The resulting expressions are of the same form as the multiple scattering theory for s-wave scatterers.

To find the current, we have to take the gradient of equation (8.12):

$$\begin{aligned}\nabla\psi(\vec{x}) &= i\vec{k}e^{i\vec{k}\cdot\vec{x}} - \frac{1}{4}i\sum_{ij} e^{i\vec{k}\cdot\vec{x_i}} B_{ij}(H_0^{(1)}(k|\vec{x_j}-\vec{x}|)e^{i\phi_j(\vec{x})}i\frac{B}{2}(-y_j\hat{x}+x_j\hat{y}) \\ &\quad -H_1^{(1)}(k|\vec{x_j}-\vec{x}|)k(\vec{x}-\vec{x_j})/|\vec{x}-\vec{x_j}|e^{i\phi_j(\vec{x})})\end{aligned} \tag{8.15}$$

Therefore,

$$\begin{aligned}\psi^*(\vec{x})\nabla\psi(\vec{x}) &= i\vec{k} - \frac{1}{4}\vec{k}\sum_{ij} e^{i\vec{k}\cdot(\vec{x}-\vec{x_i})} B_{ij}^* H_0^{(2)}(k|\vec{x_j}-\vec{x}|)e^{-i\phi_j(\vec{x})} \\ &\quad +\frac{1}{16}\sum_{ijlm} e^{i\vec{k}\cdot(\vec{x_i}-\vec{x_l})} B_{ij}B_{lm}^* H_0^{(2)}(k|\vec{x_m}-\vec{x}|)e^{-i\phi_m(\vec{x})} \\ &\quad (H_0^{(1)}(k|\vec{x_j}-\vec{x}|)e^{i\phi_j(\vec{x})}i\frac{B}{2}(-y_j\hat{x}+x_j\hat{y}) - \\ &\quad H_1^{(1)}(k|\vec{x_j}-\vec{x}|)k(\vec{x}-\vec{x_j})/|\vec{x}-\vec{x_j}|e^{i\phi_j(\vec{x})}) \\ &\quad -\frac{1}{4}i\sum_{ij} e^{i\vec{k}\cdot(\vec{x_i}-\vec{x})} B_{ij}[H_0^{(1)}(k|\vec{x_j}-\vec{x}|)e^{i\phi_j(\vec{x})}i\frac{B}{2}(-y_j\hat{x}+x_j\hat{y}) \\ &\quad -H_1^{(1)}(k|\vec{x_j}-\vec{x}|)k(\vec{x}-\vec{x_j})/|\vec{x}-\vec{x_j}|e^{i\phi_j(\vec{x})}]\end{aligned} \tag{8.16}$$

Substituting these into equation (8.8) and average over all incident angles, we obtain an answer for the resistance, which is shown on figure 8.2. (In our numerical simulation, 6 scatterers are put on each wall length of one wavelength.) As we can see, there are peaks due to the Aharonov-Bohm effect. But this is not quite close to what the experiment observed. The peaks are too broad and rounded, which could be due to the lack of impurities in the model. Therefore, we need to put in some impurities.

8.3.4 Impurities

In the presence of impurities, the formula we will use to calculate the wavefunction is the same as the one in the previous section, except that we replace the scattering T-matrix by the total of the reflector-gates and the s-wave point scatterers. The impurities are modeled by s-wave point scatterers with a single atom t-matrix of:

$$\frac{-it}{4} = (\alpha e^{i\delta} - 1)/2 \tag{8.17}$$

We pick $\alpha = 1$ and $\delta = 1$ for each of the scatterers so that the cross length of a scatterer is around $6.2nm$. The T-matrices for the impurities and the gates-reflectors can be added by the addition formula, equation (6.47). By realizing over 25 random locations and averaging the results for the transmittivity, our results are shown on figure 8.3, which is quite close to the experimental observed. Shown are the results with an impurity concentration n_s of around 1/4 impurity per square wavelength. The corresponding mean free path is $1/n_s\sigma = 1.5\mu m$.

8.4 Conclusion

The observed results for the conductance fluctuations experiment by the Westervelt group [kat96] have been modeled and explained by using a Boundary Wall Method with impurities.

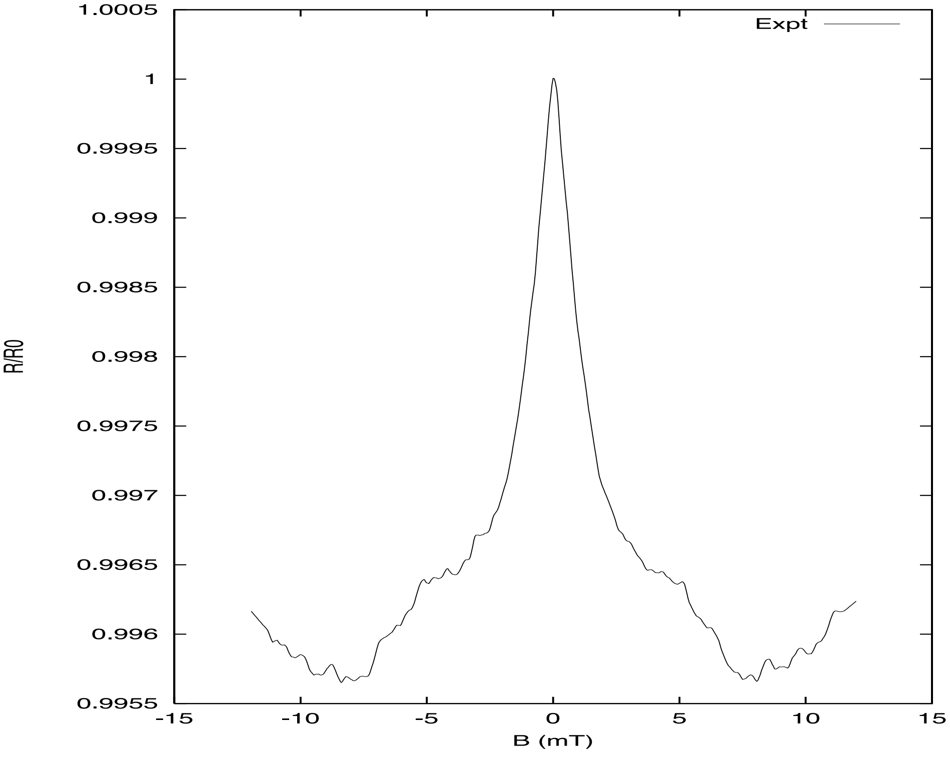

Figure 8.1: The resistance vs magnetic field for the given experimental set up is shown.

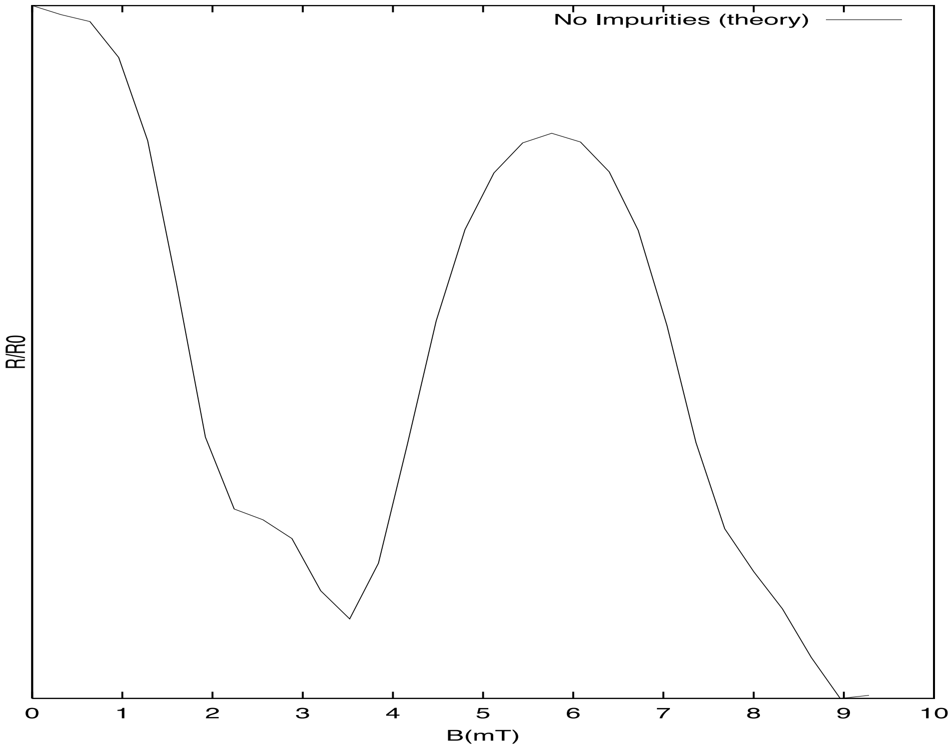

Figure 8.2: Shown is the results of the theory with no impurities.

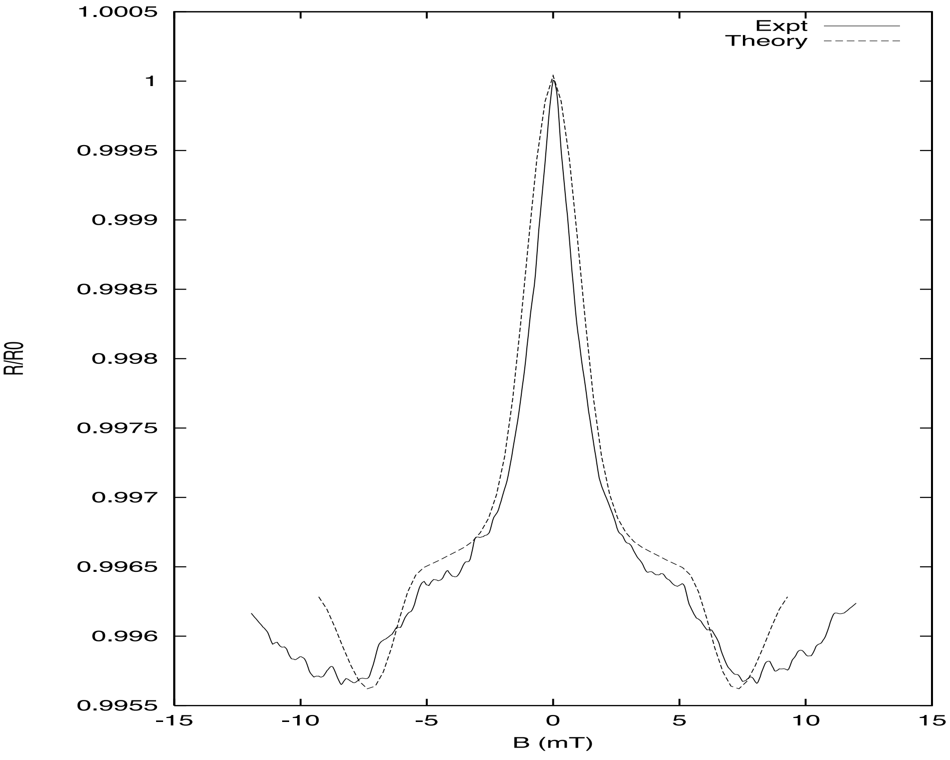

Figure 8.3: Shown is the comparison of theory with the impurities and the experimental results.

Chapter 9

Conclusion

The two-tip STM results have been obtained from the one-tip one, and the scattering properties of the step are studied. Moreover, some tiny problems in the original parametrized multiple scattering model for the “Quantum Corral” have been fixed. Proximity resonance and scattering off atomic walls have been investigated as well. These are the point-like S-wave scattering theory part of my project. Still, one might want to do an inversion theory for other defects and study the scattering properties of them as well. As for the atomic walls, straight walls are the only extended structure being studied. There is always a possiblity of building large structures of other shapes and for example, search for states that live on the perimeter of the structures.

Regarding the mathematical wall part of my project, the hard wall and impurities model accounts for the observations in the coherent backscattering experiment[kat96]. And that has been performed in the regime where 4 modes are allowed in the point contact. Current theories is being done for experiments in the tunneling regime.

Acknowledgement

First, I have to thank my advisor, Professor Heller. Without his help and encouragement, this thesis may never come into existence. Second, I would like to thank to my Committee members, Professor Ehrenreich and Professor Westervelt, for their time, helpfulness, and kindness.

Thanks to Professor Timothy Halpin-Healy for bring me into the field of theoretical physics.

Then I must thank Adam, Lev, Neepa and the rest of group for tolerating my stupid questions and helping through my hardest times. Also, thanks to Chi, Cynthia, Jenny, Karen, Konstantin, and Shilpa for being great friends.

Thanks my family for their support through all these years. Without my parents paying the tuition at Columbia, I wonder where I will be today. Thank you for giving me a chance to see this side of the world.

Lastly, thanks everyone in the Linux development project since you provide the OS on the computer where I write this thesis. And thanks Chi and Konstantin for helping me setting it up correctly.

Appendix A

Coherent Backscattering Experiment

A.1 Determination of the shape of the reflectors

Slope of the normal × slope of the reflector is -1.

$$m_b = \frac{-1}{\frac{dy}{dx}} = \tan\frac{\phi}{2} \tag{A.1}$$

Let $r = f(\phi)$. b Therefore, $x = f(\phi)\cos\phi$,$y = f(\phi)\sin\phi$.

$$\begin{aligned} \frac{dy}{dx} &= \frac{dy}{d\phi}\frac{d\phi}{dx} && \text{(A.2)} \\ &= \frac{\frac{df}{d\phi}\sin\phi + f\cos\phi}{\frac{df}{d\phi}\cos\phi - f\sin\phi} && \text{(A.3)} \\ &= \frac{\frac{df}{d\phi}\tan\phi + f}{\frac{df}{d\phi} - f\tan\phi} && \text{(A.4)} \end{aligned}$$

$$\Rightarrow m_b = \frac{-1}{\frac{dy}{dx}} = \tan\frac{\phi}{2} = \frac{f\tan\phi - \frac{df}{d\phi}}{\frac{df}{d\phi}\tan\phi + f} \tag{A.5}$$

Rearranging this expression, we obtain:

$$\frac{df}{d\phi}\frac{1}{f} = \frac{\tan\phi - \tan\frac{\phi}{2}}{1 + \tan\phi\tan\frac{\phi}{2}} = \tan\frac{\phi}{2} \tag{A.6}$$

$$\Rightarrow \frac{d}{d\phi}\ln f(\phi) = \tan\frac{\phi}{2} \tag{A.7}$$

Integrating this expression, we have:

(Let $u = \phi/2$

$$\begin{aligned} \int d\phi \tan\frac{\phi}{2} &= 2\int du \frac{\sin u}{\cos u} && \text{(A.8)} \\ &= -2\int d(\cos u)\frac{1}{\cos u} && \text{(A.9)} \\ &= -2\ln|\cos u| && \text{(A.10)} \\ &= -\ln\cos^2 u && \text{(A.11)} \end{aligned}$$

)

$$\ln f(\phi) = -\ln\cos^2\frac{\phi}{2} + C \tag{A.12}$$

$$\Rightarrow f(\phi) = R_0 \sec^2\frac{\phi}{2} \tag{A.13}$$

The schematics of the relfector is outlined on figure A.1. Define $\theta = \pi/2 - \phi$. Then,

$$f(\theta) = \frac{2R_0}{1+\sin\theta} \tag{A.14}$$

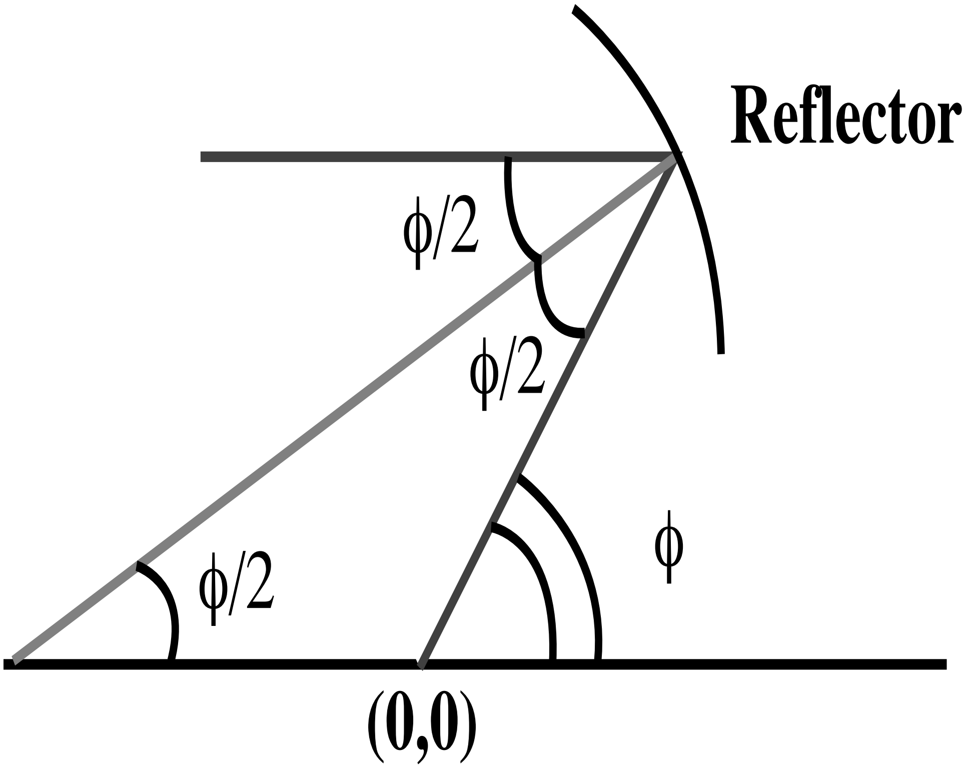

Figure A.1: The schematic of the reflector is shown. The gate is along the y axis.

Bibliography

[ando] Ando, T., Fukuyama, H. *Quantum Transport in Mesoscopic Systems: An Introduction*, Transport Phenomena in Mesoscopic Systems, Fukuyama, H., Ando, T. Ed.,Springer-Verlag (1992).

[avo90] Avouris, P., Lyo, I.-W., Walkup, R. E. and Hasegawa, Y.,*J. Vac. Sci. Technol.* B, 529 (1990).

[bar62] Bardeen, J.,*Phys. Rev. Lett.* **6**, 57(1962)

[chan97] Chan, S., Heller, E.J.,*Phys. Rev. Lett.* **78** 13,2570-2 (1997).

[cla] Clausius, R. *Die Kinetische Theorie der Gase*, Vieweg, Brauchschweig (1889).

[cro93Na] Crommie, M.F., Lutz, C.P., and Eigler, D.M., *Nature* **363**, 524-527 (1993).

[cro93Sc] Crommie, M.F., Lutz, C.P., and Eigler, D.M., *Science* **262**, 218-220 (1993).

[cro] Crommie, M.F., through private communication.

[czu] Czuber, E., *Zur Theory der geometricschen Wahrscheinlichkeiten, Sitzungsber*, Akad. Wiss. Wien. Math. Naturwiss. Kl. 2 **A 90**,719-742 (1884).

[euc] Euceda, A., Bylander, D.M., Kleinman, L., *Phys. Rev* **B 28**, 528 (1983).

[eyr] Eyring, C.F.,*Reverberation in Dead Rooms*,J. Accoust. Soc. Am. **1**,217-249 (1930).

[feen48] E. Feenberg,*Phys. Rev.* **74** 6(1948)

[gas89] Gaspard, P. and Rice, S. A. *J. Chem. Phys.* **90**, 2225-2262 (1989) for a treatment of the “three disk” problem in two dimensions.

[has93] Hasegawa, Y. and Avouris, P., *Phys. Rev. Lett.* **71**, 1071-1074 (1993).

[hel94] Heller, E.J., Crommie, M.F.,Lutz,C.P. and Eigler, D.M.,*Nature* **369** 464 (1994).

[hel96] Heller, E.J., *Phys. Rev. Lett.* **77** 20, 4122-5 (1996).

[kat96] Katine, J.A., Eriksson, M.A. WestErvelt, R.M. Campman, K.L., Gossard, A.C., *Superlattices and Microstructures* **20** 3, 337-41 (1996).

[kev83] Kevan,S.D., *Phys. Rev. Lett.* **50**, 526-529 (1983).

[lan86] Lang, N.D., *Phys. Rev.* **B 34**, 5927-5950(1986).

[luz97] Da Luz,M., Lupu-Sax,A.S., Heller,E.J., *Phys. Rev.* **E 56** 3, 2496-2507 (1997).

[mor] Mortessagne,F. *Dynamique et Interferences Geometriques Dans Les Billiards Chaotiques*, 'Unpublished Doctoral Thesis',L'Universite de Paris 7-Denis Diderot (1994).

[niu95] Q. Niu, M.C. Chang,C.K. Shih, *Phys. Rev.* **B 51**,5502-5505 (1995)

[nor] Norris,R.F.,1st Meeting ASA, New York (May 11, 1929); See V.O. Knusden, *Architectural Accoutics* Appendix II, Wiley, New York (1932).

[pre92] Press,W.H., Teukolsky, S.A. , Vetterling,W.T., and Flannery,B.P., *Numerical Recipes*, Cambridge Univ. Press 1992.

[rod67] Rodberg,L.S., and Thaler,R.M., *Introduction to the Quantum Theory of Scattering* (Academic, New York, 1967)

[sab] Sabine, W.C., *Collected Papers on Accoustics* (Cambridge, Harvard U.P. 1923); reprinted by Dover, New York (1964).

[sak] Sakurai,J.J.m *Modern Quantum Mechanics*(Addison-Wesley 1985)

[ter84] Tersoff,J. and Hamann,D.R., *Phys. Rev.* **B 31**,805-813 (1984).

[uet] Ueta, T., *J. Phys. Soc. Japan* **61** 12, 4314-24 (1992).

B 48, 2851-2854 (1993).